# Laser Desorption Analyses in Trapped Ion Mass Spectrometry Systems

ACADEMISCH PROEFSCHRIFT

ter verkrijging van de graad van doctor aan de Universiteit van Amsterdam
op gezag van de Rector Magnificus prof. dr. J.J.M. Franse,
ten overstaan van een door het college voor promoties ingestelde commissie,
in het openbaar te verdedigen in de Aula der Universiteit
op woensdag 23 juni 1999, te 10:00 uur

door

**Gerardus Jacobus van Rooij**

geboren te Geldrop

**Promotiecommissie**

| | |
|---|---|
| promotor: | prof. dr. J.J. Boon |
| co-promotor: | dr. R.M.A. Heeren |
| overige leden: | prof. dr. I.J. Amster<br>prof. dr. ir. M.J.C. van Gemert<br>prof. dr. A.J.R. Heck<br>prof. dr. F.H. Laukien<br>prof. dr. P.G. Kistemaker<br>prof. dr. J.F. van der Veen |

Faculteit der Wiskunde, Informatica, Natuurkunde en Sterrenkunde

Cover design in co-operation with Iliya Cerjak and Wim Koppers

The work described in this thesis was performed at the FOM-Institute for Atomic and Molecular Physics, Kruislaan 407, 1098 SJ Amsterdam, The Netherlands. It is part of the approved research program on mass spectrometry of macromolecular systems of the *Stichting voor Fundamenteel Onderzoek der Materie* (FOM, Foundation for Fundamental Research on Matter). The research was made possible by financial support from the *Nederlandse Organisatie voor Wetenschappelijk Onderzoek* (NWO, Dutch Organisation for Scientific Research).

*aan mijn ouders*

This thesis is based on the following papers:

Chapter 3:

*High Resolution End Group Determination of Low Molecular Weight Polymers by Matrix Assisted Laser Desorption Ionization on an External Ion Source Fourier Transform Ion Cyclotron Resonance Mass Spectrometer,* G. J. van Rooij, M. C. Duursma, R. M .A. Heeren, J. J. Boon, and C. G. de Koster, J. Am. Soc. Mass Spectrom. **7**, 449 (1996).

*End Group Analysis of Polyethylene Glycol Polymers by Matrix Assisted Laser Desorption/Ionization on an External Ion Source Fourier Transform Ion Cyclotron Resonance Mass Spectrometer,* C. G. de Koster, M.C. Duursma, G. J. van Rooij, R. M. A. Heeren, and J. J. Boon, Rapid Comm. in Mass Spec. **9**, 957 (1995).

*Correction of Time-of-Flight Shifted Polymeric Molecular Weight Distributions in Matrix Assisted Laser Desorption/Ionization Fourier Transform Mass Spectrometry,* P. B. O'Connor, M. C. Duursma, G. J. van Rooij, R. M. A. Heeren, and J. J. Boon, Anal. Chem. **69**, 2751 (1997).

Chapter 4:

*Determination of Block Length Distributions of Poly(oxypropylene) and Poly(oxyethylene) Block Copolymers by MALDI-FTICR Mass Spectrometry,* G. J. van Rooij, M. C. Duursma, C. G. de Koster, R. M. A. Heeren, J. J. Boon, P. J. W. Schuyl, and E. R. E. van der Hage, Anal. Chem. **70**, 843 (1998).

Chapter 5:

*Design and Performance of an Arbitrary Waveform Generator for Ion Excitation in Trapped Ion Mass Spectrometry,* in preparation.

Chapter 6:

*Isotope Beating Effects in the Analysis of Polymer Distributions by Fourier Transform Mass Spectrometry,* M. L. Easterling, I. J. Amster, G. J. van Rooij, and R. M. A. Heeren, submitted to J. Am. Soc. Mass Spectrom.

Chapter 7:

*Probing Mass Discriminations and Mass Shifts in the ITMS Mass Spectra of Externally Generated MALDI Ions with Synthetic Polymers,* G. J. van Rooij, R. M. A. Heeren and J. J. Boon, submitted to Anal. Chem.

Chapter 8:

*A Novel Instrument for Spatially Resolved Surface Analysis with Laser Desorption Quadrupole Ion Trap Mass Spectrometry,* in preparation.

# Contents

# 1

# General introduction

Mass spectrometry is an increasingly important analytical tool for numerous applications in polymer chemistry, life science, environmental and marine science, archaeology, and art conservation. The remarkable developments of both instrumentation and methodology over the past decades have revolutionized the capabilities of mass spectrometry, ranging from the analysis of macromolecules with molecular weights of hundreds of thousands to measurements of attomoles of compound. There is an increasing push for higher mass resolving power and mass accuracy for larger molecular weights, higher sample throughput and more possibilities to obtain structural information. This thesis addresses the development and improvement of mass spectrometric methodologies with respect to trapped ion mass analyzers and the coupling of these analyzers with laser desorption techniques. In the next sections, the relevance of these subjects is clarified. Section 1.1 describes the advantages of laser desorption techniques compared to other desorption/ionization techniques. Section 1.2 deals with the special properties of trapped ion mass spectrometers and their ideal match with laser desorption techniques.

## 1.1 Desorption and Ionization of Large Molecules

A major issue in mass spectrometry is the formation of intact gaseous ions from compounds in the condensed phase. This process can be a severe problem if the compounds are polar, nonvolatile, of high molecular weight or thermally labile. Several desorption/ionization techniques have been developed to achieve this problematic conversion. These are generally referred to as *soft ionization* techniques, because of the (virtual) absence of fragmentation induced by the desorption and ionization event.

The various soft ionization techniques use different physical approaches to produce ions:

- A high electric field is applied to the sample in field desorption (FD) mass spectrometry [1].

- Ions are directly formed from small, charged liquid droplets in thermospray ionization [2] and electrospray ionization (ESI) [3].
- The sample is bombarded with highly energetic atoms or ions in fast atom bombardment (FAB) [4], $^{252}$Cf plasma desorption (PD) [5], and secondary ion mass spectrometry (SIMS) [6].
- Short and intense pulses of laser light are used to induce the formation of ions in laser desorption (LD) [7, 8] and matrix-assisted laser desorption and ionization (MALDI) [9].

Obviously, the choice for a particular ionization technique depends on the nature of the compounds under study and the type of information that is desired.

Application of the first two approaches (FD and ESI) to solid materials often requires time consuming sample preparation and separation steps before analysis. In addition, these methods do not readily allow the preservation of spatial information, which is often also of interest in the analysis of surfaces. Techniques based on the bombardment of the surface with energetic particles or photons do not encounter these difficulties. Sample preparation is usually not required. In addition, the primary beams can be focused to very small spot sizes. This allows localized desorption of surface material and makes it straight forward to couple the mass spectrometric information to spatial information. For example, SIMS is widely used for spatially resolved mass spectrometric characterization of semiconductors. If however dielectric materials are studied by means of SIMS, the analyses are complicated by a build-up of charge at the sample surface, as both the probe beam and the detected beam are ion beams. Further, SIMS is especially appropriate for determination of the inorganic fraction and the elemental composition of the sample surface, whereas it mainly produces non-specific ions from the organic fraction.

For the study of organic solid compounds, laser desorption mass spectrometry is the most promising technique. Similar to SIMS, a very attractive feature of this technique is the possibility to investigate complex samples directly, without the need for time-consuming sample preparation and separation steps before analysis. Additionally, it allows the production of intact gas-phase ions from fragile organic molecules. By virtue of these features, the technique has proven to be very successful in the characterization of the constituents at the surface of a broad range of samples, often with the preservation of spatial information [10–15]. Laser desorption has also been remarkably successful in the field of macromolecules since the introduction of MALDI. With the restriction that sample preparation is necessary for MALDI, intact molecules have been analyzed in the mass range up to $3 \cdot 10^5$ u [9, 16–18]. In fact, ESI is the only technique that is competitive to MALDI in these high mass ranges.

### 1.1.1 Development of LD-MS and MALDI-MS

The development of high power lasers as a tool in mass spectrometry for vaporization, atomization and/or ionization of materials starts only a few years after the discovery of the laser principle and goes back to the early 1960s. It was initiated by the problems posed by the trace analysis in dielectric samples with the then commonly used spark-sources. Honig [19] used in 1963 for the first time a laser for the production of ions for mass spectrometric analysis of non-conducting materials. Other early uses include the vaporization of graphite [20, 21] and coal [22] as well as elemental analyses [23]. The applicability of laser desorption to organic compounds was demonstrated in 1966 by Vastola and Pirone [24,25]. They reported the laser mass spectra of sodium hexylsulfonate salts. This is often cited as one of the first laser desorption results, because there was no fragmentation observed and the positive charge was carried by a sodium cation adduct. In the following period, a variety of lasers with wavelengths ranging from the far-UV to the far-IR and pulse widths ranging from picoseconds to continuous irradiation was combined with virtually every available type of mass spectrometer. It is not surprising that this led to a proportional variety in the results. Consequently, different combinations of lasers and spectrometers have evolved for different applications [7, 8].

The interest in the use of laser desorption for the analysis of non-volatile, high molecular weight, organic molecules probably originates from the work by Posthumus et al. [26] in the late 1970s. They used IR laser light to obtain mass spectra of oligosaccharides, glycosides and peptides in the mass range up to ∼1225 u with sector instruments. Around the same time, laser desorption was also applied in spatially resolved analyses. Given the fact that laser beams can be focused to spot sizes close to the diffraction limit of about 0.5 $\mu$m for UV light (although 5 $\mu$m is a more common value in practice), the laser desorption technique is ideally suited for spatially resolved analyses. Spatially resolved laser desorption, generally referred to as Laser Microprobe Mass Spectrometry (LMMS), became widely available with the introduction of commercial instruments, such as the LAMMA-500 [27], the LAMMA-1000 [28], and the LIMA [29]. In the following decades, it has been demonstrated that (spatially resolved) laser desorption is applicable to a variety of problems, both organic and inorganic in nature, and to a broad range of samples, conducting as well as nonconducting materials, thin sections as well as bulk materials. Depending on the experimental conditions, information was obtained on the elemental composition of the materials, or detailed speciation of inorganic compounds and structural characterization of organic molecules was demonstrated.

Several reviews [7, 8, 13–15, 30] describe applications, fundamentals, potential and limitations of laser desorption and LMMS. All early laser desorption experiments on organic molecules revealed an upper limit to the molecular weight of molecules that could be desorbed as intact ions. A rough estimate for this limit was ∼1000 u for biopolymers and up to 9000 u for synthetic polymers, depending on the analyzed molecules and laser parameters. A breakthrough toward higher masses came with the introduction of *Matrix Assisted* Laser Desorption and Ionization (MALDI) by Karas and Hillenkamp [31, 32] and by Tanaka and coworkers [33]. According to the MALDI technique, a low concentration of analyte molecules is embedded in a matrix consisting of species that highly absorbs the applied laser light. Since its introduction, the technique has evolved as one of the most successful volatilization and ionization methods for a wide variety of high molecular weight molecules, such as peptides, proteins, oligosaccharides, and synthetic polymers. Several reviews illustrate the continuously growing scope of MALDI-MS applications [9, 16–18, 34].

### 1.1.2 On Volatilization and Ion Formation in the Process of Laser Desorption

Numerous experiments have been performed to elucidate the nature of the laser desorption process. However, due to the many parameters that are essentially different for the various applications of laser desorption (i.e., without spatial resolution, LMMS, and MALDI), a proportional number of desorption mechanisms has been proposed. Although many of the mechanisms involved are still not unequivocally proven, it is nowadays generally accepted that the observed phenomena must be related to the principal mechanisms that are referred to as thermal, shockwave driven, and resonant processes and gas phase processes at the selvedge [35]. It is beyond the scope of this introduction to discuss the details of these ion formation modes. Instead, the main experimental observations and empirical rules are briefly summarized.

Firstly, measurements of the kinetic energy distributions of gaseous ions and neutrals produced by laser desorption led to the following observations:

1. Immediately after a laser pulse, particles are emitted that have relatively high kinetic energies. The ions that are emitted in this early stage are usually small fragments or even atomic.

2. Protonated or cationized molecules have relatively low kinetic energies.

3. In comparison to the number of ions, many more neutrals are emitted, and the release of these neutrals occurs for longer times.

Secondly, after more than two decades of systematic observations, two experimental requirements for the detection of undegraded species with laser desorption mass spectrometry have evolved:

1. Best results are obtained if efficient and controllable energy transfer to the sample is realized, which requires resonant absorption by the molecules at the laser wavelength. It has been demonstrated in a series of publications that a match between the irradiating wavelength and the molecular absorption band of the analyte leads to a drastic change in molecular ion production vs. production of fragments, threshold irradiance levels, and the effect of increasing the power density [36–39]. Generally, lasers emitting in the far UV (coupling with electronic states) and in the far IR (coupling with rovibrational states) are found to give the best results. The disadvantage of resonant excitation is that also energy deposition into photodissociation channels can be expected, which explains an upper limit to the size of intact desorbed molecules of 1000 u for biopolymers and up to 9000 u for synthetic polymers [9].

On the other hand, in nonresonant desorption experiments the necessary irradiances are very close to the onset of plasma generation, which again leads to fragmentation of large organic molecules [38].

2. Thermal decomposition of the thermally labile molecules is avoided by transferring the laser energy in a very short time (typically 1-100 ns range). It has been demonstrated experimentally that molecules can be desorbed intact and with relatively low internal energy at high heating rates, whereas they decompose at lower heating rates [40, 41]. As a consequence of the extremely fast energy deposition a strongly non-equilibrium population of energy levels in the solid is generated. The concepts for the relaxation and redistribution of these energy distributions range from rapid heating (Beuhler et al. [42]) to mechanical approaches (Williams [43]), to restricted energy transfer (Vertes and Gijbels [44]), to expansion cooling of the laser-generated plume (Vertes [45]).

Finally, it is presently believed that the use of a matrix in MALDI prevents fragmentation in the desorption process, even for high molecular weight molecules, because of the following reasons [9, 46]:

1. The strong absorbance of the matrix at the laser wavelength ensures an efficient and controllable energy transfer, which allows the operation of the laser at relatively low power densities. On the other hand, the analyte molecules usually exhibit only moderate absorption at the same wavelength. As a result no excessive energy is deposited into the analyte, which prevents decomposition.

2. The dilution of the analyte in a very high excess of matrix prevents association of the analyte molecules and reduces strong intermolecular interactions. These would otherwise lead to complexes too large to be desorbed and analyzed.

3. Analyte ionization may be strongly promoted by photochemical reactions. Photoexcitation or photoionization of matrix molecules followed by proton (or cation) transfer to the analyte molecules is supposed to be a major ionization mechanism for analytes, which can form stable cationized ions.

## 1.2 Mass Analysis of Ions Produced by Laser Desorption and Ionization

Once the choice for the optimal ionization technique has been made, the ideal type of mass analyzer is still to be determined. The aspects that determine whether a mass analyzer is suitable for a specific application include the mass range of interest and the desired mass resolution and accuracy. But first of all, the mass analyzer must be compatible with the applied ionization technique.

The pulsed nature of the ionization process in laser desorption allows scanning instruments to monitor only a single mass [47] or a narrow mass range if array detection [26] or rapid scanning [48] are applied. For this reason, quadrupole mass spectrometers and magnetic-sector instruments are rarely employed in combination with laser desorption. In contrast, Time-of-Flight (TOF) instruments are capable of panoramic registration of the mass spectrum with quasi-unlimited mass range for each individual laser pulse. In addition, TOF instruments are the mass analyzers with the highest sensitivity and their pulsed mode of operation matches ideally the pulsed nature of the laser desorption process. It is therefore not surprising that TOF instruments are mostly used in combination with laser desorption, especially since the introduction of commercially available TOF-based laser microprobes.

Limitations in mass resolution of TOF instruments, however, point to the need for high mass resolution experiments. The Fourier Transform Ion Cyclotron Resonance Mass Spectrometer (FTICR-MS), which is the most distinguished trapped ion mass analyzer, offers unequivocally high mass resolution, while the covered mass range for each laser pulse is still around $10^4$ u (for singly charged ions). The combination of FTICR-MS with laser desorption is particularly attractive because the production of discrete ion bunches matches its discontinuous mode of operation. Furthermore, optimization of the mass resolution does not necessarily decrease the signal intensity and ion detection is non-destructive. The latter means that the ions remain available for subsequent experiments such as collision induced dissociation and tandem mass spectrometry. The coupling between laser desorption and FTICR-MS has been pioneered by McCreary [49] et al. and Wilkins et al. [50]. In the following years, outstanding mass resolving powers have been evidenced, which ranged from 60,000 at $m/z$ 6000 for synthetic polymer distributions [51] to 3,600,000 for elemental silicium ions [52].

The second type of trapped ion mass analyzers is the quadrupole Ion Trap Mass Spectrometer (ITMS), which was invented by Paul and Steinwedel [53]. Routine use of an ion trap for mass spectrometry has been made feasible by a new mode of operation that was developed by Stafford et al., called mass selective instability [54]. The use of an ITMS as the mass analyzer in laser desorption experiments is a relatively new and unexplored area. The earliest reports of this combination date from only 1989 [55, 56]. Nevertheless, the ITMS is particularly appealing in its possibility of performing multiple-stage mass spectrometry experiments, the lack of pressure problems, its high sensitivity (comparable to the sensitivity of TOF analyzers), the low costs of manufacturing, and its ease of operation. Similar to FTICR-MS, the ion trap also matches the generation of discrete ion bunches excellently.

## 1.3 Overview of this Thesis

The central theme of the work presented in this thesis is the coupling of the laser desorption technique to the two types of trapped ion mass analyzers. Despite the attractiveness to implement laser desorption in trapped ion mass analyzers outlined in section 1.2, this coupling is certainly not trivial. Possible problems arise from the broad kinetic energy distribution of ions produced with lasers. Ions with high kinetic energies are difficult to recover by the application of low trapping potentials. Also the relatively limited dynamic range of trapping instruments can be a pitfall in analytical applications. These are typical issues that initiated the experiments described in this thesis.

From the viewpoint of the two types of trapped ion mass analyzers, i.e., the FTICR-MS and the ITMS, this thesis can be divided in two parts. Experiments performed with the FTICR-MS instrument are presented in the first part (Chapter 3,4, 5, and 6), while the second part deals with experiments performed in the ITMS instrument (Chapter 7 and 8). These chapters are preceded by a discussion on the operation principles and the hardware of the two trapped ion mass spectrometers in Chapter 2.

The first part starts with the implementation of laser desorption in the FTICR-MS instrument in Chapter 3. The performance of the new configuration is characterized by results of MALDI measurements of synthetic polymer samples. On basis of these results, new methods for processing the mass spectra are developed. These concern on the one hand the optimal utilization of the instrumental mass accuracy for the determination of polymer repeating units and end groups, and on the other hand the correction for a mass discrimination effect that is inherent to discrete ion bunches analyzed by external ion source FTICR-MS. Initiated by the growing interest of chemical industry for this subject, these are applied to a copolymer sample in Chapter 4. The copolymer results prove the validity of the methodologies proposed to process spectral data for accurate and detailed characterization of polymer samples and demonstrate the utility of MALDI-FTICR-MS for polymer characterization.

It became evident in the course of these experiments that the versatility of the FTICR-MS instrument is immensely expanded if ions can be manipulated in a mass selective way. Chapter 5 describes the design and performance of a novel arbitrary waveform generator, which has been constructed to address this need. Its ultra-high mass selectivity is demonstrated with the isolation of single isotopes in the FTICR-MS cell. In Chapter 6, this waveform generator is utilized to investigate isotope beating as a source of error in the determination of polymer molecular weight distributions. Also numerical simulations are included in this chapter to investigate the nature of the experimentally observed distortions.

The second part of this thesis starts with Chapter 7. In this chapter, the coupling of laser desorption to the ITMS is described. The synthetic polymer samples that were investigated by MALDI-FTICR-MS, were also studied in the ITMS instrument in order to characterize its performance. Finally, the experience obtained with respect to laser desorption as well as trapped ion mass spectrometry is exploited in Chapter 8 to develop a novel ion source for spatially resolved analyses. This laser microprobe ion source is successfully coupled to the ITMS instrument. First results are presented, which demonstrate that this combination offers great possibilities with respect to the analysis of organic fractions in heterogeneous surfaces.

## 2

# Theory and Operating Principles

*The results described in this thesis were obtained with two different mass spectrometers: a Fourier Transform Ion Cyclotron Resonance Mass Spectrometer and a Quadrupole Ion Trap Mass Spectrometer. This chapter deals with the theoretical concepts, the layout of the instruments, and the experimental procedures for both techniques.*

## 2.1 Introduction

In FTICR-MS and ITMS, ions are confined in a trap by the joint effect of an approximately quadrupolar electrostatic potential and a second force provided by either a static magnetic field (FTICR-MS) or a quadrupolar rf electric potential (ITMS). In both techniques, the motion of the ions inside the trap is modulated to determine the ion's mass-to-charge ratios. This chapter discusses some theoretical aspects of the ion motion in the two types of ion traps that are useful to understand the experimental techniques. These discussions are heavily based on the excellent book of Marshall and Verdun [57] and the mini-series of three volumes edited by March and Todd [58]. The theoretical discussions are followed by a description of the instrumental hardware and the experimental procedures that made it possible to measure the spectra presented throughout this thesis. The FTICR-MS technique is considered in Section 2.2. The ITMS technique will be considered in Section 2.3.

## 2.2 Fourier transform Ion Cyclotron Resonance Mass Spectrometry

A schematic diagram of the analyzer cell in the FTICR-MS instrument used within the framework of this thesis is shown in Figure 2.1. The analyzer cell is positioned inside the bore of a 7T superconducting magnet, to produce a homogeneous magnetic field in the $z$-direction inside the cell. The magnetic force that acts on ions with non-zero kinetic energy induces these ions to move in stable cyclotron orbits in the $xy$-plane, and therefore confines them in this plane. The ions are prevented from escaping in the $z$-direction from the

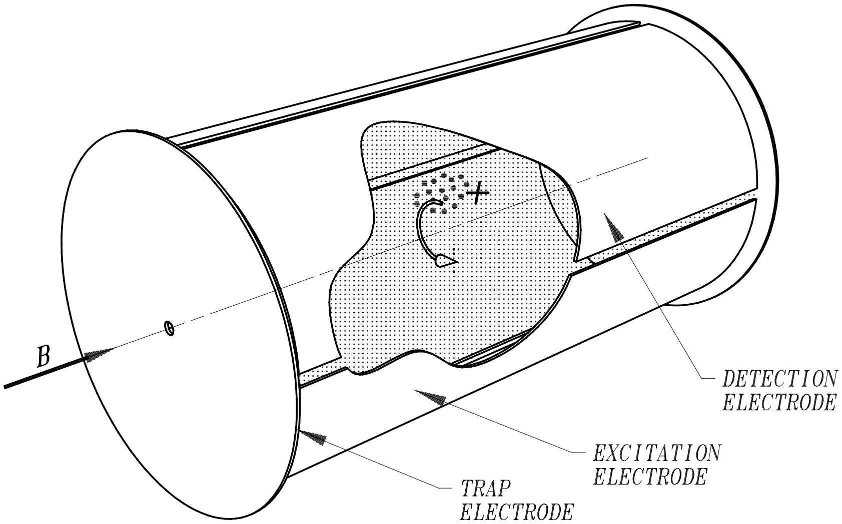

**Figure 2.1:** *Schematic of the FTICR analyzer cell. The cell is positioned inside the bore of a 7T superconducting magnet. Indicated are the three sets of opposed electrodes.*

cell by the application of an electrostatic potential well between the two opposed trapping electrodes. The use of a homogeneous magnetic field and an electrostatic potential to confine charged particles in space dates from the 1930s and is known as a Penning trap [59]. The natural ion motions induced by such a combination of fields are discussed in Section 2.2.1. From this discussion it will also follow that a determination of the frequency of the ion cyclotron motion is synonymous to a measurement of the mass-to-charge ratio of the ions. In section 2.2.2 it will be shown how an oscillating radiofrequency electric field applied to the excitation electrodes produces a coherent cyclotron motion. This motion can be detected by measurement of the image current that is induced by the coherently orbiting ions in the set of detection electrodes. The resulting time domain signal contains a manifold of frequency components that correspond to the different masses inside the cell. The Fourier analysis method transforms this complex waveform into a frequency domain index that describes the individual frequencies and their magnitudes. This information is used to determine the masses and abundances, and thus describes the ion population. The layout of the instrument used for the FTICR-MS measurement and the experimental procedures are described in detail in section 2.2.3.

### *2.2.1 Natural Motions inside the ICR Cell*

The motion of ions in circular orbits originates from the magnetic force that acts on the ions. The understanding of this cyclotron motion starts with the Lorentz force equation

$$\vec{F}_L = m\frac{\mathrm{d}\vec{v}}{\mathrm{d}t} = q\vec{E} + q\vec{v} \times \vec{B} \tag{2.1}$$

which gives the force that acts on a point charge $q$ with velocity $\vec{v}$ and mass $m$ in the presence of electric and magnetic fields $\vec{E}$ and $\vec{B}$. Consider the case of an ion that moves in the $xy$-plane with velocity $v_\perp$ in a uniform magnetic field along the $z$ axis and in the absence of electric fields, as is depicted in Figure 2.2. It is seen from eqn. 2.1 that this ion experiences a Lorentz force in the direction parallel to the $xy$-plane and perpendicular to its velocity. The Lorentz force will therefore act as a centripetal force, which changes only the direction of the ion velocity and not its magnitude. Consequently, the magnitude of the Lorentz force will remain constant as well, and the ion will move in a stable circular orbit with radius $r$. The frequency of this ion cyclotron motion is found by equation of the Lorentz force to the centripetal acceleration in a circular motion, $v_\perp^2/r$, multiplied by the ion mass:

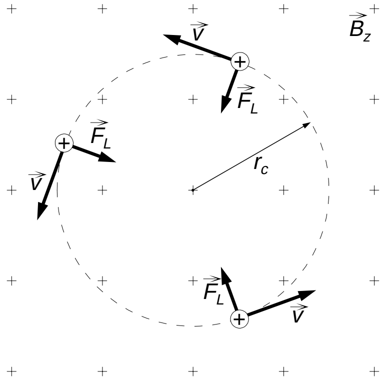

**Figure 2.2:** *Origin of the ion cyclotron motion. The velocity of the ion is perpendicular to the uniform magnetic field (the crosses represent the tail of the magnetic field vector), leading to a Lorentz force perpendicular to both. This causes the ion to move in a stable circular orbit.*

$$qv_\perp B = \frac{mv_\perp^2}{r} \tag{2.2}$$

This immediately gives the radius of the cyclotron motion:

$$r_c = \frac{mv_\perp}{qB} \tag{2.3}$$

Because angular velocity is defined by $\omega = v_\perp/r$, the frequency of the cyclotron motion in the absence of electric fields is given by:

$$\omega_c = \frac{qB}{m} \tag{2.4}$$

These expressions reveal several important aspects of the ICR technique. Firstly, it is seen from eqn. 2.4 that all ions of a given mass-to-charge ratio, $m/q$, have the same cyclotron frequency, independent of their initial velocity. Measuring the cyclotron frequency of an ion is therefore synonymous to measuring its $m/q$ ratio. Secondly, differentiation of eqn. 2.4 with respect to $m$ leads to:

$$\frac{\omega_c}{\mathrm{d}\omega_c} = -\frac{m}{\mathrm{d}m} \tag{2.5}$$

In other words, frequency resolution equals mass resolution in ICR mass spectrometry (except for a minus sign). Finally, insertion of the average $v_\perp$ of a thermal ion at room temperature ($m < v_\perp^2 >= 2kT$ where $k$ is the Boltzmann constant) into eqn. 2.3 yields that at a magnetic field strength of for example 7 T even relatively heavy ions are confined to small ($< 1$ mm) orbits. Conversely, computation of the translational energy of an ion at a larger orbital radius with eqn. 2.3 shows that ions can be “heated” to high translational energy in the relatively small ICR cell. This feature can be used to advantage to fragment ions by collisions with neutral gas molecules. The magnitude of the ion’s translational energy is plotted as a function of the mass-to-charge ratio for different cyclotron radii at a 7 T magnetic field strength in Figure 2.3.

The natural motion of ions in the presence of a magnetic field along the $z$-direction effectively confines these ions in the $xy$-plane. Let us now consider the confinement in the $z$-direction by the application of an electrostatic potential $V_T$ to each of the two trapping electrodes, with the remaining electrodes electrically grounded. This produces an approximately quadrupolar electric potential near the center of the trap, which can be written in the form

$$V = V_T\left(\alpha + \frac{z^2 - r^2/2}{2d^2}\right) \tag{2.6}$$

Here, $\alpha$ is a coefficient that depends on the trap dimensions as well as the configuration and shape of the trap electrodes, and $d$ is the internal diameter of the trap. Note the presence of the radial coordinate $r$ in the potential. This can be understood by Gauss’s law of electrostatics, which states that electric field lines that enter a closed electrically neutral region must also leave that region. The static voltage applied to the trap electrodes generates an electric field pointing inward along the $z$-axis to the center of the cell, and will therefore necessarily result into an electric field pointing radially outward.

The electric field in the axial direction is obtained from the negative $z$-derivative of the electrostatic potential:

$$E(z) = -\frac{\mathrm{d}V}{\mathrm{d}z} = -\frac{V_T}{d^2}z \tag{2.7}$$

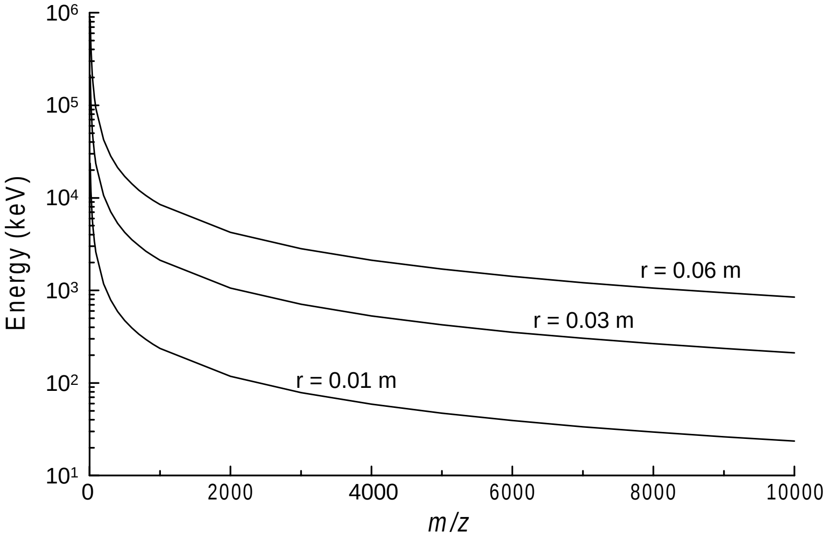

**Figure 2.3:** *Translational energy of ions in an ICR cell at a 7 T magnetic field strength as a function of the ion's mass-to-charge ratio for different cyclotron radii.*

Insertion of this electric field strength into the Lorentz force equation (eqn. 2.1) gives the equation of motion of the ion in the $z$ direction:

$$F(z) = m\frac{\mathrm{d}v_z}{\mathrm{d}t} = -\frac{qV_T}{d^2}z \tag{2.8}$$

Eqn. 2.8 is immediately seen to describe an harmonic oscillator in a quadratic potential well. Accordingly, the ions oscillate along the $z$-direction at a natural trapping frequency

$$\omega_T = \sqrt{\frac{qV_T}{md^2}} \tag{2.9}$$

With the addition of the electrostatic potential, the radial motion of the ions is no longer described by eqn. 2.2. The radial component of the potential of eqn. 2.6 introduces a radially repulsive electric field strength given by:

$$E_r = \frac{V_T}{2d^2}r \tag{2.10}$$

The total radial force on the ion is obtained from the radial component of the Lorentz force equation (eqn. 2.1):

$$m\frac{\mathrm{d}v_\perp}{dt} = qv_\perp B - \frac{qV_T}{2d^2}r \tag{2.11}$$

The repulsive radial potential has two consequences for the ions natural radial motion. First, the frequency of the cyclotron rotation is reduced because the centrifugal force on the ion (i.e., the radial Lorentz force) is reduced. Second, a drift of the center of the cyclotron orbit is superimposed in the direction perpendicular to the radial electric field. This drift is called magnetron motion. The reason for the magnetron motion becomes obvious from the physical picture drawn in Figure 2.4. There, it is seen that the ion is accelerated by the radial electric field when it moves radially outward due to its cyclotron motion. This increase in $v_\perp$ induces necessarily an increase in $r_c$. In the second half-cycle, when the direction of the cyclotron motion is radially inward, the ion is decelerated and decreases in $r_c$. The difference in $r_c$ on the exterior and interior sides of the cyclotron orbit relative to the center of the analyzer cell causes a drift of the guiding center.

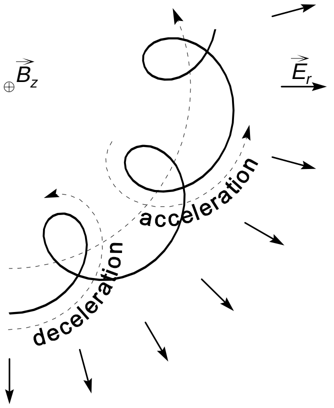

**Figure 2.4:** *Origin of the ion magnetron motion. The ion is accelerated when its cyclotron motion is in the direction of the radial electric field and decelerated when its cyclotron motion is in the opposite direction. The radii and frequencies of the magnetron and cyclotron motion are not scaled.*

To investigate the nature of the magnetron motion in more detail, it is realized that the cyclotron motion is unimpeded according to an observer moving with the guiding center. This means that with respect to the guiding center the electric force in the Lorentz force equation (eqn. 2.1) is canceled by the magnetic force:

$$\vec{E} + \vec{v}_{gc} \times \vec{B} = 0 \tag{2.12}$$

Here, $v_{gc}$ is the drift velocity. The vector product with $\vec{B}$ gives:

$$\begin{aligned} \vec{E} \times \vec{B} &= \vec{B} \times \left(\vec{v}_{gc} \times \vec{B}\right) \\ &= \vec{v}_{gc} B^2 - \vec{B}\left(\vec{v}_{gc} \cdot \vec{B}\right) \end{aligned} \tag{2.13}$$

The transverse components of this equation are

$$\vec{v}_{\perp,gc} = \vec{E} \times \vec{B} / B^2 \tag{2.14}$$

Elimination of the radial electric field with eqn. 2.10 shows that the motion of the guiding center is a circular motion with the same direction of rotation as the cyclotron orbit along a path of constant radial electric potential. The angular frequency of this motion, which is independent of $m$ and $q$, is given by:

$$\omega_{\perp,gc} = \frac{V_T}{2d^2} = \frac{\omega_z^2}{2\omega_c} \tag{2.15}$$

The frequencies of the natural ion motions in the $xy$-plane are again obtained by balancing the Lorentz force to the centripetal acceleration multiplied by the ion mass:

$$qv_\perp B - q\frac{V_T}{2d^2}r = m\frac{v_\perp^2}{r} \tag{2.16}$$

Rewriting with the angular velocity $\omega = v_\perp/r$ and the unimpeded cyclotron and trapping frequencies yields:

$$\omega_c\omega r - \frac{1}{2}\omega_T^2 r = \omega^2 r \tag{2.17}$$

Eqn. 2.17 has to two solutions for the natural frequency of ion motion in the $xy$-plane

$$\omega^+ = \frac{1}{2}\left(\omega_c + \sqrt{\omega_c^2 - 2\omega_T^2}\right) \tag{2.18}$$

$$\omega^- = \frac{1}{2}\left(\omega_c - \sqrt{\omega_c^2 - 2\omega_T^2}\right) \tag{2.19}$$

Here, $\omega^+$ represents the reduced cyclotron frequency and $\omega^-$ the frequency of the magnetron motion.

The frequencies of the natural ion motions have been calculated with eqns. 2.9, 2.18 and 2.19 for ions trapped in a cylindrical cell ($d = 0.06$ m) at a magnetic field strength of 7 T. The potential applied to the trapping electrodes was assumed to be 1 V. The results are plotted as a function of the ion mass in Figure 2.5. The plot shows that the trapping frequency is typically much smaller than the cyclotron frequency, and that the magnetron motion is again much smaller than the trapping frequency.

### 2.2.2 *Excitation and Detection of ICR signals*

In the previous section it was shown that the mass of an ion can be measured by detection of its cyclotron frequency. However, it is obvious that no measurable signals can be obtained when a large number of ions is orbiting with random phase and thermal energies. It is therefore necessary to move ions with equal mass spatially coherent off-center. This can be realized by application of an oscillating field to a pair of opposed excitation electrodes, which is resonant with the cyclotron frequency of the ions of interest, as is illustrated in Figure 2.6. Because the excitation plates are positioned parallel to the $xz$-plane, this will

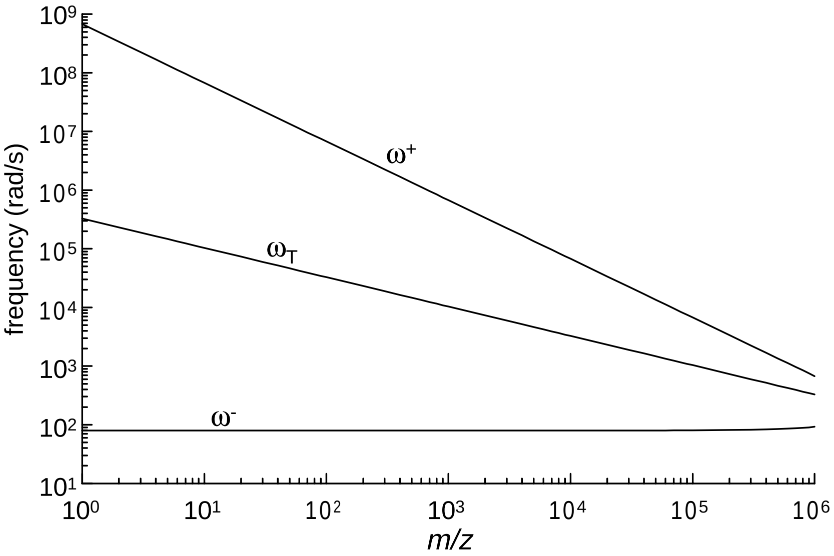

**Figure 2.5:** *The natural frequencies of motion as a function of the mass-to-charge ratio for ions in a 6 cm diameter cylindrical cell at a magnetic field strength of 7 T and a trapping potential of 1 V.*

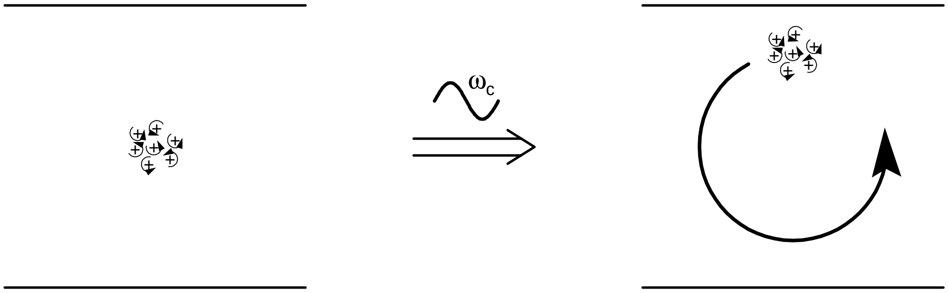

**Figure 2.6:** *Excitation of the ion cyclotron orbital motion. Application of a dipole field oscillating at the ICR frequency of the ions to the excitation plates converts incoherent cyclotron motion (left) to coherent motion (right).*

generate an electric excitation field inside the cell of the form

$$\vec{E}_{exc}(t) = E_0 \sin \omega_c t \vec{j} \tag{2.20}$$

Here, $\vec{j}$ is the unit vector in the $y$-direction. Ions in resonance with this field will absorb power according to

$$A(t) = q\vec{E}_{exc}(t) \cdot \vec{v} \tag{2.21}$$

to increase their cyclotron radius in time. The inner product in eqn. 2.21 is readily calculated if the excitation field is resolved into two counter-rotating components:

$$\begin{aligned} \vec{E}_{exc}(t) &= \vec{E}_1(t) + \vec{E}_2(t) \\ \vec{E}_1(t) &= \frac{1}{2}E_0\left(\sin \omega_c t + \cos \omega_c t\right) \\ \vec{E}_2(t) &= \frac{1}{2}E_0\left(\sin \omega_c t - \cos \omega_c t\right) \end{aligned} \tag{2.22}$$

Here, only the field that rotates in the same sense as the ions of interest is of importance for the absorption of energy because the time average of the energy absorption of the other field component is zero. Insertion of eqns. 2.22 into 2.1, solving for $v_\perp$, and finally inserting $v_\perp$ into eqn. 2.21 yields for the instantaneous rate of power absorption (in the absence of dampening mechanisms during the excitation):

$$A(t) = \frac{E_0^2 q^2 t}{4m} \tag{2.23}$$

The cyclotron radius of an excited ion is calculated by integration of eqn. 2.23 over the total excitation time, $T_{\text{excite}}$. If it is assumed that this total absorbed energy is entirely converted into kinetic energy, the ions are excited to a cyclotron radius of:

$$r = \frac{E_0 T_{\text{excite}}}{2B_0} \tag{2.24}$$

It is immediately seen from eqn. 2.24 that the cyclotron radius is independent of the ionic mass. Consequently, if the frequency spectrum (or magnitude spectrum) of the applied excitation electric field is constant over a certain frequency range, then all ions within the corresponding $m/q$ range are excited to the same cyclotron radius.

There are four methods commonly employed in FTICR-MS for the production of excitation signals with a reasonably flat magnitude spectrum over a desired $m/q$ range. The first and simplest excitation waveform is the rectangular pulse (or “impulse”) excitation and is shown in the top panel of Figure 2.7. It is seen that its magnitude spectrum significantly varies with frequency. The central peak in the spectrum corresponds to the frequency interval that is effectively excited and its width is inversely proportional to the excitation time.

The second method is generally used in high-resolution experiments. It is the single-frequency excitation, which is shown in the second panel of Figure 2.7. The excitation

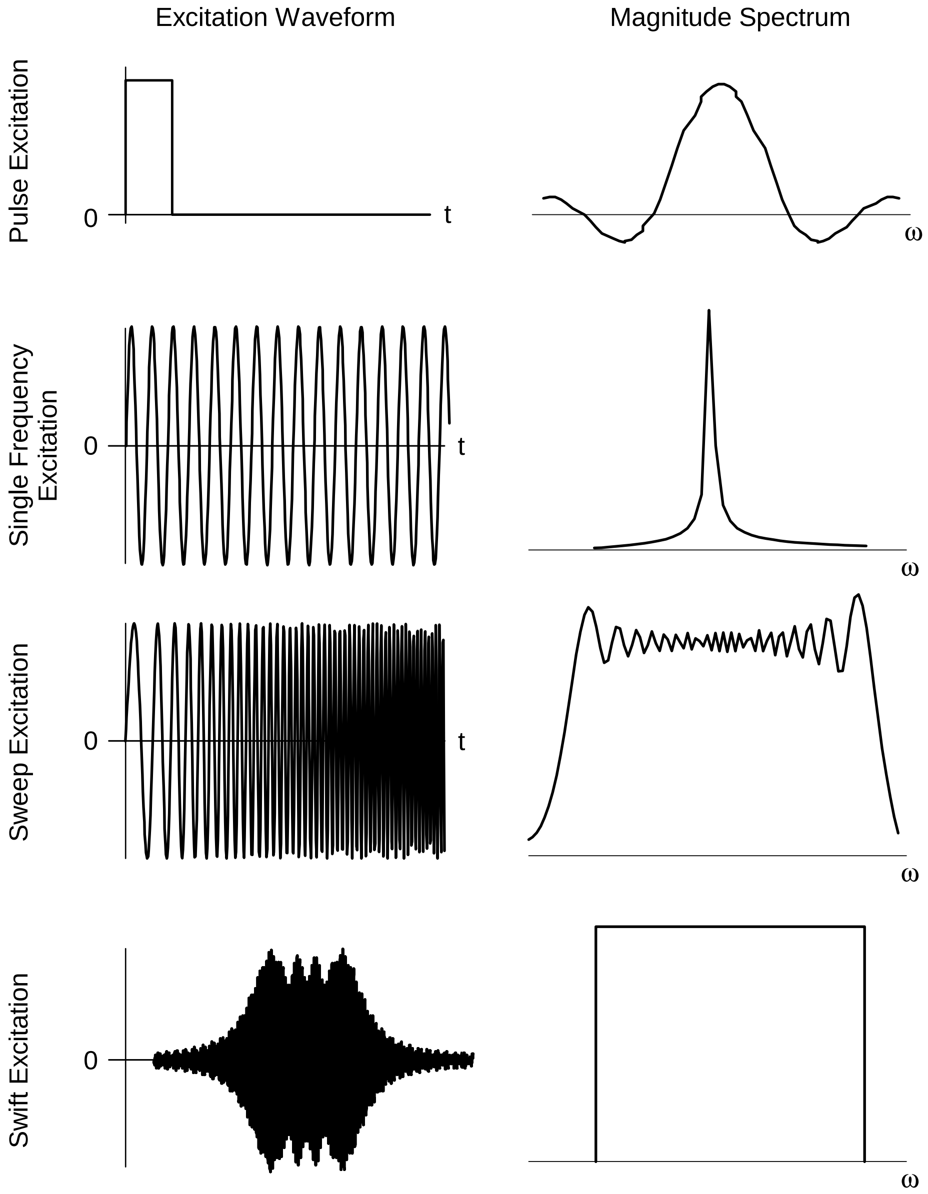

**Figure 2.7:** *The three different excitation waveforms and their frequency-domain magnitude spectra, which are frequently employed in FTICR-MS: for narrow band excitation the rectangular pulse excitation and for broad band excitation the frequency sweep and the SWIFT waveform.*

waveform is a sinusoid with fixed amplitude and frequency. The corresponding magnitude spectrum shows that this method is only suitable for excitation of ions within a very small mass range.

The cyclotron motion of ions can be excited over a wide $m/q$ range by application of a frequency sweep (“chirp”) excitation. This waveform consists of a sinusoid with constant amplitude, whose frequency changes linearly in time. An example of a frequency sweep excitation waveform and its magnitude spectrum are shown in the third panel of Figure 2.7. The figure indicates that the magnitude spectrum is relatively uniform over the scanned frequency range. The amplitude of the oscillations in the frequency spectrum is determined by the rate of frequency change in the excitation waveform. A slower sweep rate will lead to a more uniform excitation magnitude spectrum. The sweep excitation method is generally applied in broad band experiments.

The most sophisticated excitation method is the so-called Stored Waveform Inverse Fourier Transform (SWIFT) method [60]. According to this method, first the desired magnitude spectrum is specified. Subsequently, an inverse Fourier transformation is performed to generate the corresponding (discrete) time-domain excitation waveform. This waveform is stored in the memory of an arbitrary waveform generator and passed through a digital-to-analog converter to yield an analog signal, which can be used for excitation. The advantage of this method is that it is able to produce excitation waveforms with optimal flat magnitude spectra, as is illustrated in the bottom panel of Figure 2.7. In addition, it allows excitation magnitude spectra of nearly arbitrary shape. The SWIFT method will be described in more detail in Chapter 5, where the development of a novel arbitrary wave generator is discussed.

The necessity for an excitation waveform with a constant magnitude spectrum was already emphasized in the discussion of the different methods for the excitation of the ion cyclotron motion. This becomes more clear from the method that is applied to detect ionic masses from their excited cyclotron motion. In FTICR-MS, the cyclotron motions of all ions are first excited to an orbital radius that is a little smaller than the separation between the two opposed detector plates. Subsequently the excitation power is switched off and the image current on the detector plates resulting from the alternating charge induced by the coherently orbiting ions is measured. It is evident that the induced image current is proportional to the distance between the cyclotron orbit of the ions and the detector plates. Consequently, the relative intensities in the mass spectrum will be distorted if ions of different mass are excited to different cyclotron radii.

The mass resolution in FTICR-MS is proportional to the the time domain acquisition period (assuming that no signal dampening is present) and inversely proportional to the mass-to-charge ratio of the ions [57]. The fundamental limitation for the mass resolution is the duration of a detectable image current signal (which is determined by loss of phase-coherence due to collisions or significant variations in the individual average cyclotron frequencies [57]). On the other hand, the resolution might be unnecessarily limited if the image current signal is sampled directly (the so-called “broad band” or “direct” mode). This occurs if the memory size of the digitizer is not sufficient to store the entire ion signal for a given digitizer speed (the latter is determined by the lowest $m/z$ value of interest). In that case, the acquisition period can be elongated by application of an alternative detection mode: the “high-resolution” or “heterodyne” mode. In this mode, the ion signal is mixed with the signal of a reference oscillator, whose frequency is centered at the cyclotron frequency range of interest. The result is that all cyclotron frequency components present in the original ion signal are lowered to their difference with the reference frequency. In this way, it is possible to sample data at a much lower speed and thus for much longer acquisition times. The width of the frequency range that can be measured in the heterodyne mode is determined by the speed of the digitizer.

### *2.2.3 Instrumental Layout and Experimental Procedures for FTICR-MS measurements*

The FTICR-MS experiments were performed on a heavily modified Bruker-Spectrospin (Fällanden, Switzerland) APEX 7.0e FTICR-MS with an external ion source [61, 62]. A schematic of its vacuum system, which was in-house designed and build, is depicted in Figure 2.8. It consists of three regions, which are separated by pumping restrictions.

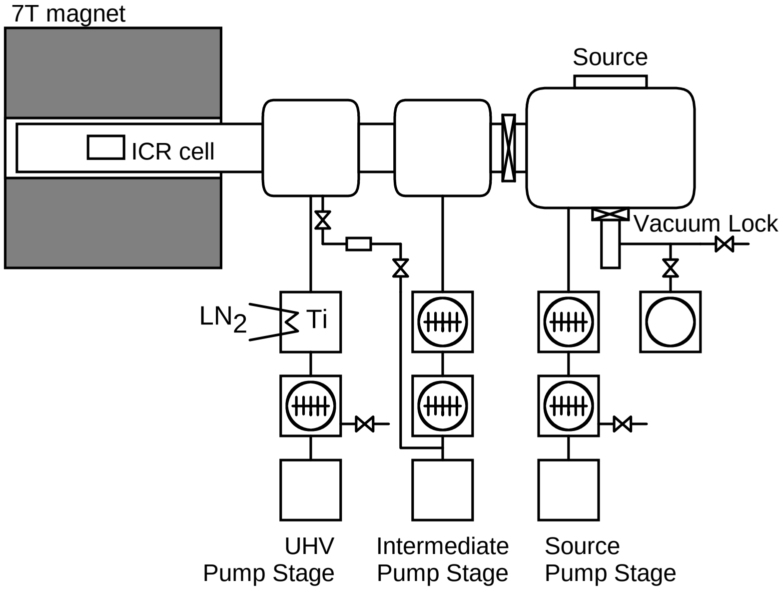

Figure 2.8: Vacuum system of the external ion source FTICR-MS.

The ICR analyzer cell, a so-called Infinity Cell [63], is installed in the UHV region, which is centered inside the bore of the 7 T superconducting magnet. The external ion source is mounted inside the source region at the other side of the vacuum system. In between is a region for intermediate pumping. The UHV region is pumped by a hybrid titanium sublimation and turbodrag pump, backed by an oil-free membrane pump. The other regions are pumped by a combination of a turbomolecular pump and a turbodrag pump, backed by an oil-free membrane pump. In this way, it is possible to maintain a pressure difference of 5 orders of magnitude between the ICR cell region (typically at a base pressure of $\sim 1 \cdot 10^{-10}$ mbar) and the ion source (typically at a base pressure of $\sim 1 \cdot 10^{-6}$ mbar). The advantages of this pumping scheme include a high compression rate for helium, optimal cleanliness inside the vacuum system, and ease of operation. The UHV region can be heated to 175°C while inserted in the bore of the superconducting magnet that is kept at room temperature. Bake out of the system for 2 days allows UHV pressures of $< 5 \cdot 10^{-11}$ mbar in the ICR cell region. Two pulsed valves are mounted on the UHV stage, which allow controlled introduction of collision gases for collisionally activated dissociation or quadrupolar axialization experiments [64].

At the beginning of an FTICR-MS experiment, the analyzer cell is emptied by application of a quench pulse to the trap electrodes. Subsequently, ions produced in the external ion source and extracted from the source region are injected into the cell. These ions are first accelerated to 3 keV through Bruker's electrostatic ion optics for penetration of the inhomogeneous strayfield of the magnet and finally decelerated to typically -1.9 eV at the entrance of the analyzer cell. In the configuration of the Infinity Cell, injection is realized by lowering the voltage on the source-side trapping electrode and a deflection electrode (positioned in front of this trapping electrode) to a negative entrance potential. This creates a channel for the ions through the trapping field. If ions are created by means of a pulsed ionization technique, this cell gating is accompanied by a TTL trigger pulse for the ionization event. The rear trapping electrode remains at typically 3.5 V to prevent ions from escaping the cell at the rear end. After a trapping delay, these electrodes are reset to a source-side trapping voltage of typically 2.5 V. In this way, ions are efficiently trapped inside the analyzer cell and further injection of ions is blocked as the ion beam is no longer directed to the cell entrance. The duration of the trapping delay is typically $10 - 100$ ms for ionization techniques producing a continuous ion beam. In the case of pulsed ionization techniques, this time delay is determined by the time required by the ions in the mass range of interest to travel from the source to the cell (see Chapter 3.4.1). After a delay of typically $50$ ms to permit the trapped ions to equilibrate inside the cell, the trapped ions are coherently excited to a radius close to the cell radius by means of a frequency sweep excitation from a frequency synthesizer. This excitation waveform consists of a number of single-frequency pulse excitations, which are shifted over the desired excitation frequency range. For example, ions in the mass range $m/z$ 280-6000 are efficiently excited in the present instrument if the frequency range 385.0-17.9 kHz is covered in 70 steps of 12 $\mu$s duration with an increment of 5240 Hz. The coherent cyclotron motion is detected by digitizing the image current induced on the detection electrodes using a 12-bit, 20 MHz analog-to-digital converter. The resulting time domain signal is stored in a 128 kbyte fast memory. Finally, discrete Fourier transformation and magnitude calculation of the time domain signal produces the frequency spectrum, which is transformed to a mass spectrum.

Control of the measurements on the FTICR-MS and data acquisition and processing are performed by the Bruker software XMASS running on an SGI Indigo R4000 (Silicon Graphics, Mountain View, CA) UNIX-based workstation.

## 2.3 Ion Trap Mass Spectrometry

The quadrupole ion trap is the three-dimensional analogue of the two-dimensional quadrupole mass filter. It consists of an arrangement of three electrodes that allows the confinement of gaseous ions by application of electric fields only. One of these electrodes is a cylinder symmetrical ring electrode that is positioned between the remaining two end cap electrodes, as is illustrated by the exploded schematic in Figure 2.9. In the case of the ideal quadrupole ion trap, the internal surfaces of the electrodes are shaped such that a pure quadrupole electric potential inside the trap is produced by application of a potential difference to the ring electrode, whereas the two end caps remain at ground potential. This requires that the internal surfaces correspond to hyperbolic equipotential surfaces of the desired potential.

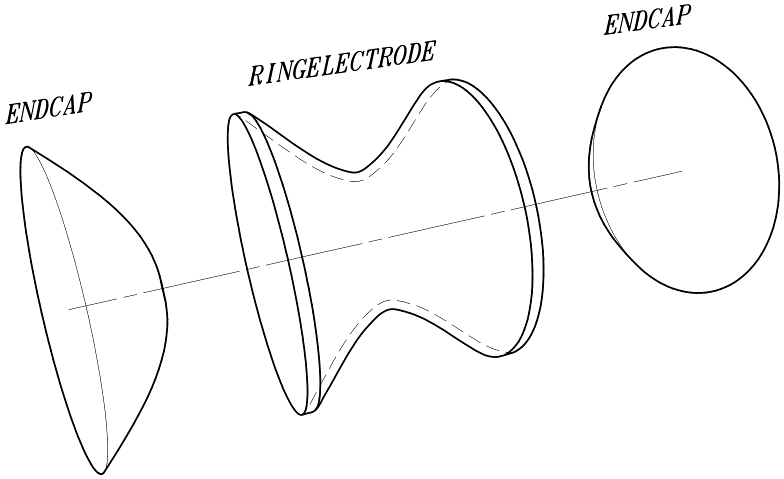

**Figure 2.9:** *Schematic of the ion trap. The trap consists of three electrodes: two end caps and a cylinder-symmetric ring electrode.*

The confinement of ions within the ion trap is illustrated by the quadrupole potential that is plotted in Figure 2.10 for a plane that intersects the trap's symmetry axis. The gradient of this potential is equal to the force that acts on ions. Because the potential is purely quadrupolar, this force varies linearly with the ion's position inside the trap. It can readily be seen from the plot that ions in the central region of the trap are confined in the

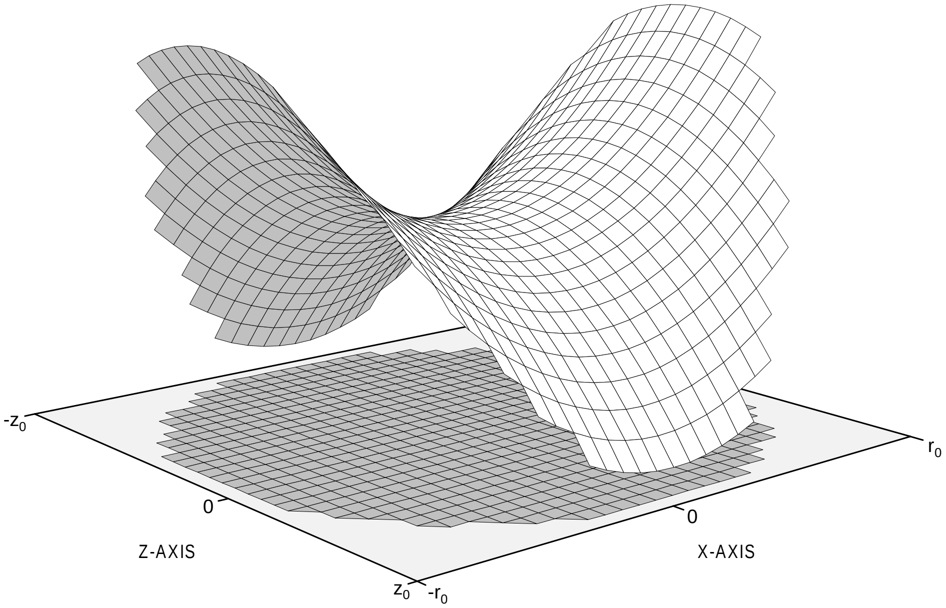

**Figure 2.10:** *Parabolic potential well that acts within an ideal ion trap if a potential difference is applied to the ring electrode whereas the end caps remain at ground potential. The z-axis is chosen along the trap's symmetry axis and the x-axis perpendicular to this axis.*

axial z-direction. However, in the radial direction, ions are accelerated towards the end caps and are not confined. Confinement in all directions can be obtained if the direction of the field is changed every time that the ions approach one of the trap electrodes. In other words, radial deceleration and axial acceleration constantly change to radial acceleration and axial deceleration and visa versa. This is realized by application of a radio frequent (rf) signal in the MHz range to the ring electrode. The result is that ions with a mass-to-charge ratio falling within appropriate limits will undergo stable oscillations.

### *2.3.1 Theory of the Ion Motion in a Quadrupole Ion Trap*

In this discussion it is assumed that both end cap electrodes are grounded and that an electric potential of [58]

$$\Phi = U + V \cos \Omega t \tag{2.25}$$

is applied to the ring electrode, where $U$ and $V$ are the direct and the alternating components of the potential and $\Omega$ is the angular frequency of the alternating component. In the ideal ion trap, this establishes the pure quadrupole potential that is in cylindrical polar coordinates ($r$,$z$) given by

$$\Phi(r,z) = (U + V\cos\Omega t)\,\frac{r^2 - 2z^2 + 2z_0^2}{r_0^2 + 2z_0^2} \tag{2.26}$$

Here, $r_0$ and $z_0$ are the inner radius of the ring electrode and the closest distance from the center of the trap to the end-cap electrode, respectively. The differential equations of motion are readily obtained from the gradient of this potential:

$$\frac{\mathrm{d}^2 r}{\mathrm{d}t^2} = -\frac{2e}{m(r_0^2 + 2z_0^2)}\,(U + V\cos\Omega t)\,r \tag{2.27}$$

$$\frac{\mathrm{d}^2 z}{\mathrm{d}t^2} = 2\frac{2e}{m(r_0^2 + 2z_0^2)}\,(U + V\cos\Omega t)\,z \tag{2.28}$$

It is seen that the axial component of motion is out-of-phase by half a cycle with respect to the radial component (hence the difference in sign), and the factor of two arises because of the asymmetry of the ion trap brought about by the need to obey the Laplace condition $\nabla^2\Phi = 0$ when applied to eqn. 2.26. These equations can be cast in the canonical form of the Mathieu equation, which has the generalized form

$$\frac{\mathrm{d}^2 u}{\mathrm{d}\xi^2} + (a_u - 2q_u\cos 2\xi)\,u = 0 \tag{2.29}$$

where $u = r, z$, $\xi = \Omega t/2$, and the Mathieu parameters $a_u$ and $q_u$ are given by

$$a_z = -2a_r = \frac{-16eU}{m(r_0^2 + 2z_0^2)\Omega^2} \tag{2.30}$$

and

$$q_z = -2q_r = \frac{8eV}{m(r_0^2 + 2z_0^2)\Omega^2} \tag{2.31}$$

The Mathieu parameters are fundamental to the operation of the ion trap since they determine whether the solutions of the Mathieu equation are bounded and the ion motion is stable. Solutions of eqn 2.29 have been studied in detail by McLachlan [65]. Stable solutions are known to have the general form

$$u(\xi) = A_u u_c(\xi) + B_u u_s(\xi) \tag{2.32}$$

where $A_u$ and $B_u$ are arbitrary constants and

$$u_c(\xi) = \sum_{n=-\infty}^{+\infty} C_{2n,u}\cos(2n + \beta_u)\xi \tag{2.33}$$

and

$$u_s(\xi) = \sum_{n=-\infty}^{+\infty} C_{2n,u}\sin(2n + \beta_u)\xi \tag{2.34}$$

The coefficients $C_{2n,u}$ give the amplitudes of the allowed modes in the spectral analysis of $u$. The spectrum of frequencies corresponding to the parameter pair $(a_u, q_u)$ is determined by $\beta_u$. Recalling that $\xi = \frac{1}{2}\Omega t$ it is seen that these frequencies $\omega_{u,n}$ are equal to

$$\omega_{u,n}|n + \frac{1}{2}\beta_u|\Omega, \qquad -\infty < n < \infty \tag{2.35}$$

It is beyond the scope of this discussion to solve the Mathieu equation to obtain expression for the various parameters in eqn. 2.32. Instead, only the resulting continued fraction expression for $\beta_u$ in terms of the Mathieu parameters as was deduced by McLachlan [65] is stated here for completeness:

$$\begin{aligned}\beta_u^2 = a_u + &\frac{q_u^2}{(\beta_u^2+2) - a_u - \frac{q_u^2}{(\beta_u^2+4)-a_u-\frac{q_u^2}{(\beta_u^2+6)-a_u-\cdots}}} \\ &+ \frac{q_u^2}{(\beta_u^2-2) - a_u - \frac{q_u^2}{(\beta_u^2-4)-a_u-\frac{q_u^2}{(\beta_u^2-6)-a_u-\cdots}}}\end{aligned} \tag{2.36}$$

This relationship has been used to produce the Mathieu stability diagrams that are shown in the subsequent discussion on stable ion motion.

### 2.3.2 Stable Ion Motions in the Quadrupole Ion Trap

The primary concerns in the operation of the ion trap are the experimental conditions that determine whether an ion is confined within the trap or is ejected, and either detected or lost to the environment. Evaluation of the solutions of the Mathieu equation [65] pointed out that these are stable for those values of $a_u$ and $q_u$ for which $2n < \beta_u < 2n + 1$. For other values, the solutions may be periodic but are unbounded. The stable solutions can be plotted in a diagram with $a_u$ and $q_u$ as coordinate axes. Such graphical representations of stable solutions are called stability diagrams. The stability diagrams for the axial and radial component of the Mathieu equation are depicted in Figure 2.11 A and 2.11 B, respectively. Note that only the positive values are shown along the $q_u$-axis. This is because symmetry exists about the $a_u$-axis. For the same reason, it is allowed to ignore the sign difference between $q_r$ and $q_z$ in the further discussion on stability diagrams. The regions that represent the $(a_z, q_z)$ values for which the Mathieu equation leads to stable solutions are shaded in Figure 2.11 A. The regions which correspond to solutions that are stable in the radial direction, are indicated in Figure 2.11 B, and are twice the size of the axial direction regions rotated about the $q_z$-axis.

Ions are confined in the ion trap if they are stable in both directions simultaneously. This condition is investigated by the superimposition of the stability diagrams in Figure 2.11 C. It should be noted that the scales of the axes in Figure 2.11 C are in units of $a_z$ and $q_z$, although the axes are labeled $a_u$ and $q_u$. The region closest to the origin in which

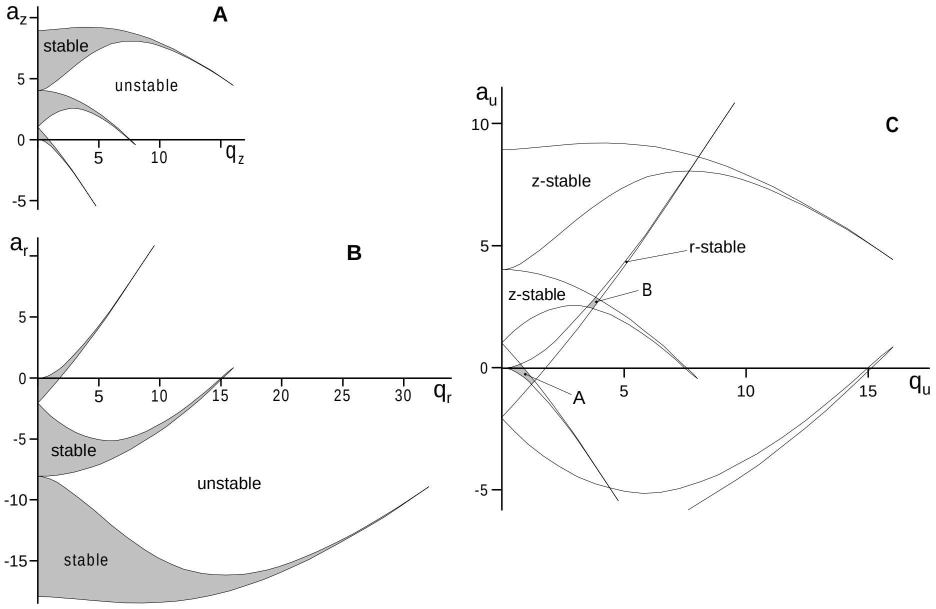

**Figure 2.11:** *Graphical representation of stable solutions of the Mathieu equation by stability diagrams. Shown are the stability diagram in the axial direction (A), in the radial direction (B), and for simultaneous stability in both directions (C). In C, the axes are labeled* $a_u$ *and* $q_u$*, but the scales are in units of* $a_z$ *and* $q_z$*.*

the condition of simultaneous stability is met, is shaded and indicated as region A. This region is of the greatest importance and is plotted in greater detail in Figure 2.12 Finally, it is important to mention that ions of different $m/z$ can simultaneously have a position within the stability region. The motion of these ions is however characterized by different $a_z$ and $q_z$ values for fixed $U$ and $V$. This dispersion according to mass is the basis of the mass separation with an ion trap, which is discussed in the next section.

### *2.3.3 Mass Separation with the Quadrupole Ion Trap*

There have been three essentially different methods to separate ions according to their mass when they were stored in the quadrupole ion trap. Initially, “mass-selective detection” was applied. According to this method, the motion of the ions was sensed by means of tuned circuits [66]. Subsequently, the method of “mass-selective storage” was introduced, in which the ions were trapped according to their $m/z$ ratios and then were ejected into an external detector [67,68]. The current separation method relies on “mass-selective ejection” of ions [54,69].

The operation of the ion trap in the mass-selective ejection mode is explained in Figure

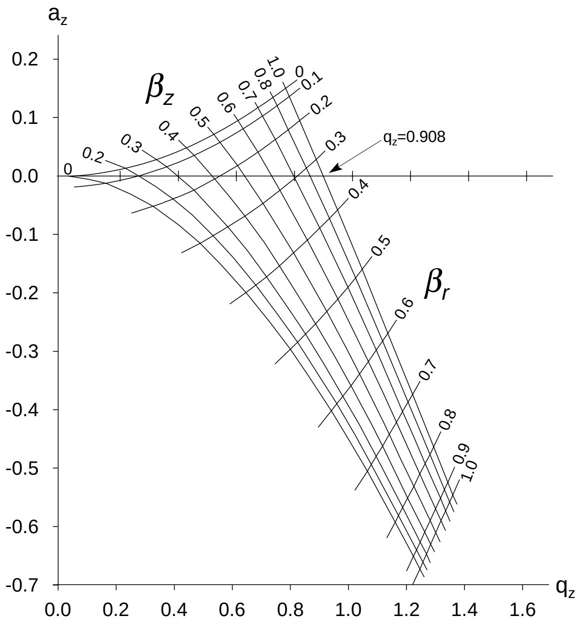

**Figure 2.12:** *Stability diagram in $(a_z, q_z)$ space for the region of simultaneous stability in both axial and radial directions. The iso-$\beta_r$ and iso-$\beta_z$ are shown in the diagram. The $\beta_z = 1$ boundary and the $q_z$-axis intersect at $q_z = 0.908$.*

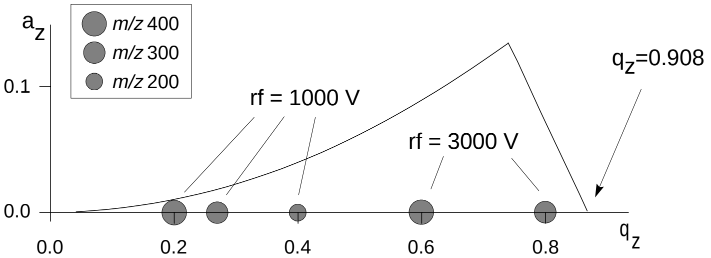

**Figure 2.13:** *Position of ions in the stability diagram for different $m/z$ ratios and rf amplitudes.*

2.13. In this figure, the position of different $m/z$ ions is depicted in the stability diagram for different rf amplitudes. It shows that an ion with a high $m/z$ becomes unstable at a higher rf amplitude than those with a lower $m/z$ ratio. In a mass-selective ejection scan, the rf voltage is linearly raised in time to increase the $q_z$ of all ions. If the $q_z$ value for a specific $m/z$ reaches the boundary of the stability region (where $q_z = 0.908$ if no direct voltage is applied and thus $a_z = 0$), the corresponding ions will become unstable in the axial direction and be ejected from the trap through one of the end caps. In this way, ions of increasing $m/z$ are ejected in sequence and can be detected as a function of the applied rf voltage (i.e., time). The voltage scale is easily converted into a mass scale by rewriting the expression for $q_z$ (eqn. 2.31):

$$\frac{m}{e} = \frac{4V}{r_0^2 \Omega^2 q_z^{\text{eject}}} \tag{2.37}$$

Here, $q_z^{\text{eject}}$ is the value of $q_z$ at which instability occurs.

Eqn. 2.37 reveals also that the mass range in which ions can be analyzed is limited for given frequency and maximum amplitude of the rf voltage. For example, in the Finnigan MAT ion trap, which is the first commercial instrument that applied the mass-selective ejection scan, masses up to approximately $m/z$ 650 can be analyzed (rf frequency 1.1 MHz; maximum rf voltage 7500 $\text{V}_{0-p}$; radius $r_0$=0.01 m). There are obviously four ways to extend the mass range of the ion trap to higher masses:

1. Operation of the trap at lower angular frequencies ($\Omega$).
2. Operation of the trap at higher values of rf voltages ($V$).
3. Reduction of the trap dimensions ($r_0$)
4. Ejection of ions at a lower value of $q_z$.

The first two options have already been implemented in recent instruments. For example, the commercial Bruker ion trap that is used for the experiments described in this thesis (Chapter 7 and 8) employs an rf frequency of 781 kHz, and a maximum voltage of 10,000 $\text{V}_{0-p}$. This extends theoretically the mass range to $m/z$ 1600. A further decrease of $\Omega$ and increase of $V$ is instrumentally demanding and therefore not attractive. The same applies to a reduction of the trap dimensions.

The simplest way to extend the mass range is to cause the trapped ions to become unstable at a value of $q_z$ lower that 0.908. This is achieved by modulation of the ion motion at a chosen frequency with a dipole electric field applied across the end caps. Ions that have a secular frequency in the axial direction equal to the applied dipole frequency increasingly gain amounts of translational energy and are ejected from the trap. This means that the value of $q_z^{\text{eject}}$ can be arbitrarily set by adjustment of the dipole frequency. This process is known as resonant ejection.

Conceptually, the supplementary dipole field creates a line of resonant ejection in the stability diagram for which $q_z$ corresponds to the frequency applied to the end caps. This

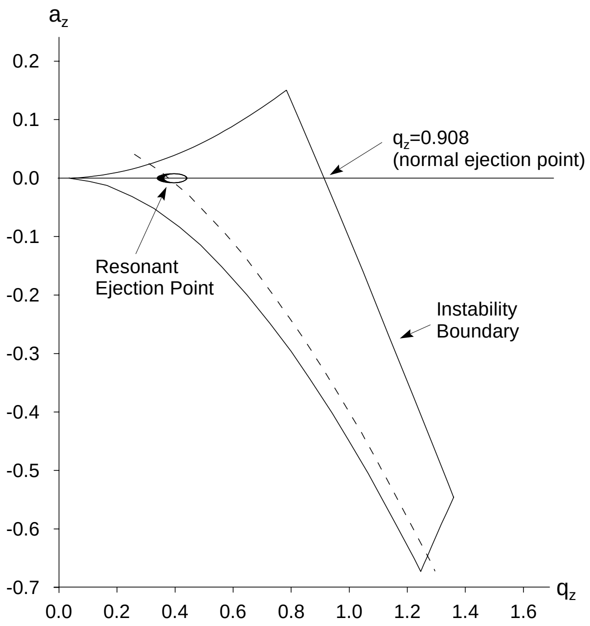

**Figure 2.14:** *The effect of resonant ejection on the stability of ions. The dashed line indicates where instability is introduced by the dipole field. Intersection of this iso-$\beta$ line and the scan line corresponds to $q_z^{eject}$.*

is visualized in Figure 2.14 by the dashed line. The intersection of this iso-$\beta$ line with the mass-selective instability scan line, which is the $q_z$-axis if the instrument is operated without a direct voltage on the ring electrode, creates a hole in the stability diagram that corresponds to $q_z^{\text{eject}}$.

The potential of the resonant ejection mode to extend the mass range is nicely illustrated by high mass experiments carried out by Kaiser et al. [70]. They used a reduced rf frequency of 920 kHz and a resonance dipole frequency of 4600 Hz ($\beta_{\text{eject}} = 0.01$, $q_z^{\text{eject}} = 0.02$). The result was an expected mass range extension to 72,000 u, which allowed the measurement of positive singly-charged $(\text{CsI})_n\text{Cs}^+$ cluster ions up to $n = 171$ ($m/z$ 44,560).

### 2.3.4 Experimental Procedures for ITMS Measurements

The ITMS experiments described in this thesis were performed with an in-house constructed instrument. The ion trap in this instrument was obtained from Bruker-Franzen Analytik GmbH (Bremen, Germany), and is identical to the one in the commercial Bruker Esquire instrument. The operation of the trap is discussed in this section. Details on the complete instrument will be given in the instrumental sections of Chapter 7 and 8, because its construction was an important aspect of the work described in these chapters.

A schematic diagram of the Bruker-Franzen ion trap is shown in Figure 2.15. It is a so-called “multipole-superimposed” ion trap. This means that the mainly quadrupolar field has contributions from hexapolar and octopolar fields. These contributions are created by a slight change in the angle of the asymptotes associated with the hyperbolic shape of the end caps and ring electrode. The effect of higher order poles in the design has been discussed by Franzen et al. [71]. The practical importance is that additional resonances are introduced in the stability diagram. The resonance at $\Omega/3$ is in particular of interest, because this is also the secular frequency at which ions are resonantly ejected from the trap in the standard measuring mode.

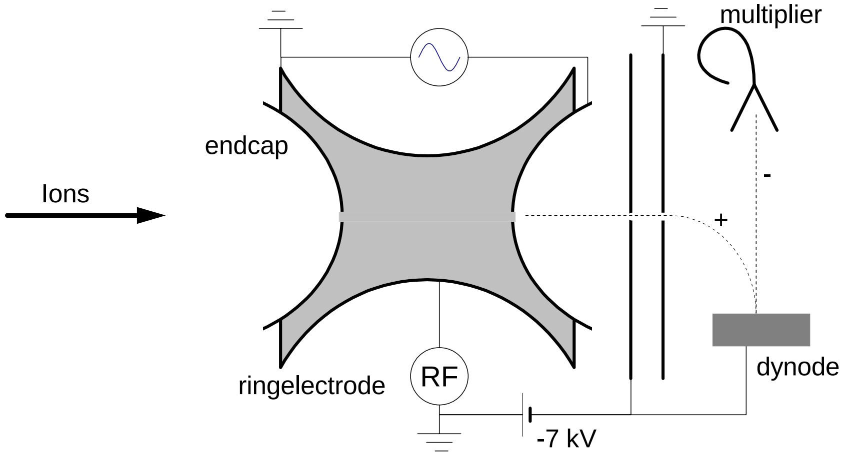

**Figure 2.15:** *Schematic diagram of the Bruker-Franzen ion trap. Ions that are ejected from the trap are detected by a combination of a conversion dynode and an electron channel multiplier.*

The frequency of the rf voltage that is applied to the ring electrode is 781 kHz and its maximum amplitude is 10 $\mathrm{kV}_{\text{0-p}}$. The exit end cap that faces the ion detector is connected to the auxiliary rf voltage for resonant excitation, whereas the entrance end cap is kept at ground potential (Figure 2.15). The primary and the dipole field are phase locked, which provides reproducible ion excitation and preferential ejection of ions through the exit end cap. The amplitude of both rf voltages are ramped during the non-linear resonance ejection scan. The ramp rate of the primary rf voltage and the frequency of the dipole field depend on the mode of analysis. These are listed in Table 2.1. The externally produced ions are injected into the active trapping field of the ion trap. Helium background gas is introduced into the ion trap at an estimated pressure of $10^{-3}$ mbar to aid in the ion trapping by collisional dampening of the ion kinetic energies. The amplitude of the rf voltage during injection is determined by the so-called cut-off mass $M_{\text{cut-off}}$. The value of $M_{\text{cut-off}}$ corresponds to the $m/z$ ratio that is in resonance with the dipole field at that

**Table 2.1:** *The four modes of measuring and the corresponding operation parameters that are available in the Bruker software.* $^{*}$*The upper mass limit for the high mass mode was restricted to 3400* u *due to software limitations during the measurements presented in this paper.* $^{**}$*Maximum scan width for which it is possible to store the complete multiplier signal as function of time.*

| Mode of analysis | Mass range | Scan rate | Maximum scan width$^{**}$ | dipole frequency |
|---|---|---|---|---|
| Standard | 50-2000 | $\sim$ 2000 u/s | 800 | $\Omega/3$ |
| High res. | 50-2000 | $\sim$ 500 u/s | 400 | $\Omega/3$ |
| Extended | 50-3400 | $\sim$ 1700 u/s | 1200 | $\Omega/6$ |
| High | 100-6000$^{*}$ | $\sim$ 8000 u/s | 1200 | $\Omega/11$ |

amplitude. The relation between the amplitude during injection and the cut-off mass is in the standard mode given by:

$$V_{rf} = \frac{0.2}{e}\Omega^2 r_0^2 M_{\text{cut-off}} \tag{2.38}$$

This relation is obtained by insertion $q_z^{\text{eject}} = 0.8$ into eqn 2.37. As can be deduced from the stability diagram in Figure 2.12, $q_z^{\text{eject}} = 0.8$ corresponds to $\beta_z = 0.67$, which in turn corresponds to a secular frequency that is equal to that of the dipole field.

In case tandem mass spectrometry experiments are performed, a (software imposed) maximum of six stages of precursor ion isolation and subsequent excitation can be included in the experiment (prior to the mass-selective ejection scan). Precursor ions are isolated by application of a dipole field with an associated broad band frequency spectrum that contains all resonance frequencies covered by the analyzed mass range except for the resonance frequency of the precursor ion. The time required for the isolation step is typically 60 ms. This is followed by resonant excitation to induce decomposition by collisions with the background gas. The excitation waveform comprises a small frequency band around the precursor ion's resonance frequency.

Ions that are ejected from the trap are detected by the combination of a conversion dynode and an electron channeltron detector. In this configuration, the ions are accelerated over 7 kV towards the dynode to induce a secondary electron signal. This signal is detected by the channeltron (model 7596mh3, K and M Electronics, Westspringfield, MA) that is operated at typically -1.2 kV (maximum operation voltage 3000 V). The multiplier signal is digitized at a rate of 10 u$^{-1}$ for the standard and the high resolution measuring mode and at a rate of 6 u$^{-1}$ in the other modes. This is however only possible if the maximum width of the mass range that is listed in Table 2.1 is not exceeded. The multiplier signal is converted in a bar graph that represents intensities for integer masses only if larger mass ranges are examined.

# 3

# Accurate Determination of Polymer End Groups and Molecular Weight Distributions by MALDI-FTICR-MS

*The performance of a newly configured external ion source Matrix Assisted Laser Desorption and Ionization Fourier Transform Ion Cyclotron Resonance Mass Spectrometer (MALDI-FTICR-MS) is examined. Experiments on low molecular weight polymers are carried out to investigate two key issues in the performance: the accuracy of the mass determinations and mass discrimination effects that distort the measured spectra. Mass accuracies are investigated by the determination of end group masses of native and derivatized polyethylene glycols (average molecular weights* $\sim 1000$ *u and* $\sim 4000$ *u). Two methods to determine end group masses from the spectral data are evaluated: a regression method and an averaging method. The averaging method is demonstrated to allow end group mass determinations with an accuracy within 0.003 u for the molecular weight range from* $m/z$ *500 to 1400 and within 0.02 u for* $m/z$ *3400 to 5000. End group determination on a polyvinyl pyrrolidone sample illustrates that this is sufficient to identify the elemental composition of end groups in unknown polymer samples. Mass discrimination effects are probed by examination of measured molecular weight distributions of polyethylene glycol (average molecular weight ∼1000 u). It is observed that these are subjected to flight-time induced distortions as different ion populations are measured for varied delay times between ionization and trapping. It is shown that the distortions are compensated by superimposition of several mass spectra acquired at different trapping times, whereas summation of these spectra merely causes further distortions and can cause loss of signal/noise. The superimposition procedure is applied to a poly(styrene) chromatographic molecular weight standard (specified average molecular weight 950 u). The distribution of the polystyrene reference material is observed to have a* $\sim 20\%$ *error in the specified peak mass.*

## 3.1 Introduction

Mass spectrometric methods in combination with soft ionization techniques, which minimize fragmentation during ionization and thus produce (pseudo-) molecular ions, have become unique and powerful tools for accurate and detailed molecular weight data on high molecular weight materials. In the field of polymer chemistry, for example, soft ionization techniques that have been applied include secondary ion mass spectrometry [72], plasma desorption [73], fast-atom bombardment [74], laser desorption [75], electrospray ionization [76, 77] and MALDI [9, 18, 78, 79]. Within this range of techniques, especially MALDI mass spectrometry has rapidly become a routine tool for analysis of polymeric systems. Since its introduction by Tanaka and coworkers [33] and by Karas and Hillenkamp [32] the technique has been successfully applied to volatilize and ionize a wide variety of intact molecules apart from synthetic polymers, such as peptides, proteins, oligosaccharides. Several reviews illustrate the continuously growing scope of MALDI applications [9, 16–18].

The increased importance of MALDI mass spectrometry in synthetic polymer chemistry has been driven primarily by its ability to provide detailed information on the individual components of polymer samples that cannot be obtained by methods such as size-exclusion chromatography (SEC), light scattering, and osmometry. MALDI is currently used extensively for determination of molecular weight distributions, copolymerization structure [80], and homogeneity [81], and is beginning to be used for branching studies [82]. The rapid, low cost analysis provided by MALDI Time-of-Flight (TOF) instruments has allowed mass accuracies of 0.1% with oligomeric mass resolution [83]. The advent of delayed extraction has extended this to isotopic resolving power for polymers up to $\sim 4000$ u with mass accuracies of $\sim 150$ ppm [84–86] and, recently, 10-15 ppm mass accuracy for peptides from 1000 to 4000 u [87]. However, only the FTICR-MS [88–91] is currently capable of isotopically resolving polymers up to $23 \cdot 10^3$ u with mass accuracies better than 10 ppm for electrospray ions [77], and up to $\sim 4500$ u with $< 20$ ppm mass accuracies on ions produced by MALDI [92–94]. It has been successfully employed to determine the composition of polymers [95] and molecular weight distributions [92, 94]. Although, the latter is easily complicated by mass discrimination effects.

The MALDI process produces ions with a broad, mass-independent velocity distribution [96]. Consequently, the various components in a polymer sample will enter the trap of the FTICR-MS with different, mass-dependent kinetic energies. As the trapping efficiency is highly dependent on the kinetic energy of the ions, this will obviously lead to mass discriminations in the MALDI experiments [97, 98]. If the MALDI experiments are carried out in an internal source geometry, trapping of higher kinetic energy ions is achieved with gated deceleration potentials [92, 99, 100]. Because MALDI-ions with higher masses have higher kinetic energies compared to low mass ions, it requires longer gated trapping times to slow these ions down. Hence the duration of the gated deceleration potentials determines the mass range over which ions will be efficiently trapped. In this chapter it will be shown that also in external source MALDI the mass range in which ions are efficiently trapped depends on timing in the experiment. In the external geometry, the post-source acceleration during the transport of the ions to the ICR-cell induces a mass-dependent flight-time between ion formation and trapping, and results in a flight-time induced discrimination that is determined by the delay between ionization and trapping.

This chapter deals with the mass accuracies that can be obtained with the newly configured MALDI-FTICR-MS instrument, and with flight-time induced mass discriminations that distort spectra measured with this instrument. In Section 3.3, measurements on native, perdeutero methylated, propylated and acetylated polyethylene glycol (with known end group structures) as well as measurements on polyvinyl pyrrolidone (with unknown end group elemental composition) are discussed to compare two different methods for end group and monomer mass determination from exact measurements of the components of a polymer molecular weight distribution. Error analysis is carried out to test the accuracy of the methodology. Section 3.4 is devoted to flight-time induced mass discriminations. These are probed by variation of the delay time between ionization and trapping in a series of measurements on polyethylene glycol and polystyrene. A methodology based on the superimposition of spectra acquired at different delay times is proposed to yield the correct molecular weight distribution.

## 3.2 Experimental

### *3.2.1 Instrumental*

The MALDI-FTICR-MS experiments were performed on the heavily modified Bruker-Spectrospin (Fällanden, Switzerland) APEX 7.0e FTICR-MS, equipped with an Infinity cell and an 7 T superconducting magnet (see Chapter 2). The configuration of the external ion source for the MALDI experiments is schematically shown in Figure 3.1. The figure shows the external ion source, the Bruker ion transfer optics, and the laser optics. The home-build MALDI ion source, which is drawn in detail in the expanded view, consists of a source housing, an ion repeller and a set of extraction plates. MALDI samples, which were deposited on the stainless steel tip of a direct insertion probe, were inserted into the source via a vacuum lock. The probe tips were in electrical contact with the source housing upon insertion. The source housing was at a potential of typically 15 V, and an efficient ion extraction field was created by the application of typically 5 V and 23 V to the extraction plates and the ion repeller, respectively. A variable potential difference between the two extraction plates allowed for steering of the ions to optimize the extraction efficiency. The standard Bruker electrostatic ion optics were used to transfer the ions to the analyzer cell. The ions were accelerated to 3 keV to prevent radial ejection in the inhomogeneous stray field of the magnet and subsequently decelerated to approximately 1 eV into the Infinity cell (trap voltages $+2$ and $+3$ V, entrance voltages $-1.9$ V).

The laser beam of a Photon Technology PL2300 (London, Ontario, Canada) nitrogen laser (337.1 nm wavelength, 1.3 mJ pulse energy and 600 ps pulse duration) was used to

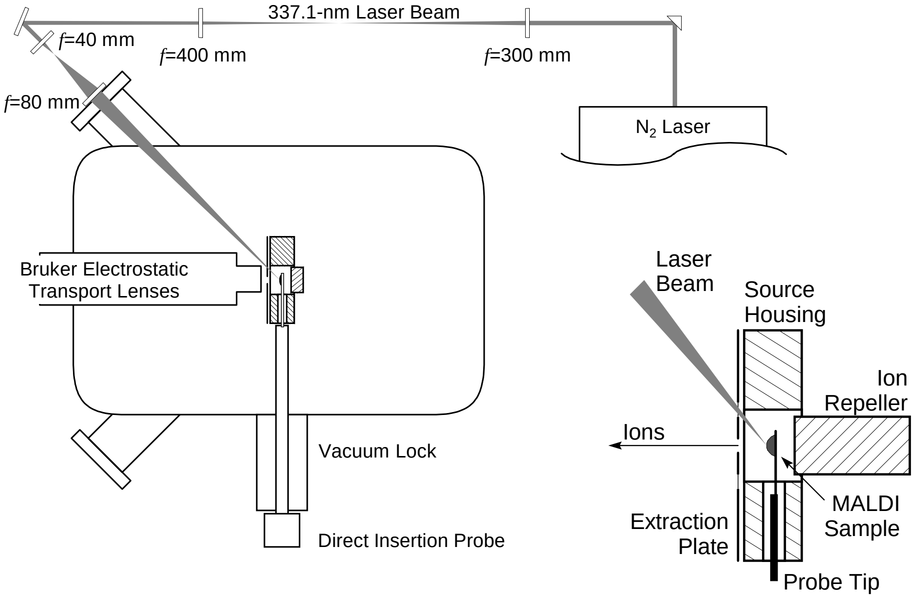

**Figure 3.1:** *Schematic overview of the external source geometry used for MALDI-FTICR-MS experiments. Indicated are the external ion source, the Bruker ion transfer optics, and the laser optics. The inset shows an expanded view of the MALDI ion source.*

produce MALDI ions. A set of biconvex lenses with 300, 400, 40, 80 mm focal length, respectively, were used to transfer the laser light efficiently to the ion source over a distance of 2 m and to focus it on the MALDI probe with an incident angle of $45°$. The exposed area on target was 4.5 mm$^2$, as was determined by the discoloration of photosensitive paper. The transmitted energy per pulse was measured to be 0.48 mJ at the position of the MALDI probe inside the ion source, which results in a fluence of 10.6 mJ/cm$^2$ (i.e., a power density of 17.5 MW/cm$^2$) on the MALDI target.

As was described in Chapter 2, the Infinity cell uses a set of electrodes in front of the source side of the cell that are pulsed to a negative voltage when the laser is fired, which creates a channel for the ions through the trapping field. After a trapping delay, the electrodes are reset to the source-side trapping voltage. This arrangement effectively gates the cell for ions during the event of ion injection, but otherwise deflects ions from the cell entrance. For the experiments dealing with end group determinations (Section 3.3), the trapping delay was optimized for maximal signal-to-noise (S/N) at the center of the measured molecular weight distributions. This was typically 1000 $\mu$s for polymer distributions in the mass range around $m/z$ 1000 and 2000 $\mu$s for distributions around $m/z$ 4000. For the experiments concerning flight-time induced shifts in the measured distributions (Section 3.4), the trapping delay was varied between 400 and 2000 $\mu$s. Experiments were also carried out in which ions were continuously directed to the cell entrance, as will be described further below.

The trapped ions were excited to a high, coherent cyclotron orbit by single-frequency excitations, each of 20 $\mu$s duration. The frequency was shifted over the desired excitation range in steps of 5240 Hz to cover the mass range of interest. The image current induced on the detection electrodes was detected at a 500 kHz acquisition rate into 128 kword data points. All spectra were signal averaged for 20 to 100 shots to increase S/N and to eliminate shot-to-shot variations in the MALDI experiment. During the experiments presented in Section 3.4, a constant S/N level on a PEG standard was maintained in order to compensate for drifts in the total ion yield.

### *3.2.2 Sample Preparation*

The polyethylene glycol (PEG) 1000 and 4000 samples were obtained from Feinbiochemica (Heidelberg, Germany) and from Fluka Chemical (Buchs, Switzerland), respectively. For the alkylation, 80 mg KOH powder was added to 25 mg PEG, and the samples were subsequently dried in vacuo over phosphorus pentoxide at 50 °C for one hour. The samples were dissolved in 1 mL dry dimethyl sulfoxide and 0.2 mL (methyl-$d_3$) iodide or propyl iodide was added. The methylation was completed at room temperature in two hours; the propylation was completed at 60 °C in five hours. The reaction was stopped by addition of 5 mL of ice water and the derivatized PEG's were extracted with trichloromethane (3 $\times$ 2 mL). The combined extracts were washed with water (3 $\times$ 2 mL). The $CHCl_3$ was evaporated under a stream of nitrogen and the residues were dried in vacuo over phosphorus pentoxide at 50 °C for one hour. The acetylated sample was prepared by dissolving 30 mg PEG in 1 mL dry pyridine. Acetic anhydride was added and the sample was allowed to react for sixteen hours at 100 °C. The pyridine and acetic anhydride were evaporated under a stream of nitrogen.

The polyvinyl pyrrolidone (PVP3000) with unknown end groups was provided by Unilever Research Laboratories (Vlaardingen, The Netherlands). Details on the origin of the sample and its properties were not communicated.

For the measurements of these samples, 2,5-dihydroxybenzoic acid (DHB; Sigma Chemical Co., St Louis, USA) was used as the MALDI matrix. The samples were prepared by mixing a 1 M matrix solution in ethanol with approximately 10 g/L analyte solution in ethanol. For PEG4000 the molar ratio 4000:1 was found to be the optimum, whereas for the other compounds the molar ratio 1000:1 gave the best results. The resulting sample matrix solution was deposited on a stainless steel probe tip using the electrospray setup depicted in Figure 3.2. In this setup, a Harvard Apparatus (South Natick, MA) syringe pump (model 55-1111) is used to deliver 0,30 mL/h of the matrix-analyte solution to a 180 $\mu$m internal diameter capillary for 20 min. This capillary is electrically isolated from the pump with a PEEK insulator and is typically set to 4 kV. The MALDI probe tip is located about 7 mm behind the capillary and is set to ground potential. The resulting analyte amount on the probe is approximately 10 ng. In comparison with the dried droplet

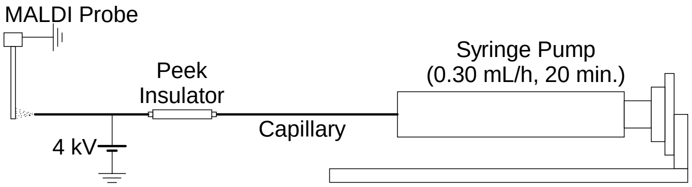

Figure 3.2: Electrospray setup for improved MALDI sample deposition.

method [9], this method of sample deposition provides smaller crystals, which result in an improvement of S/N ratio by a factor of 2 in our instrument.

The polystyrene chromatographic molecular weight standard (Merck, Darmstadt, Germany; $M_p$=950) was mixed in a 1:1 mass ratio with silver trifluoroacetate (AgTFA) and dissolved in the liquid matrix of 2-nitrophenyl octyl ether. A small drop of this mixture was applied to the probe.

## 3.3 High Resolution End Group Determination

### 3.3.1 Theoretical Considerations of End Group Analysis

Most polymeric materials consist of mixtures of molecules of various sizes due to the statistical nature of the polymerization process. Because the MALDI ionization technique leads to protonated or cationized molecules, the measured masses $M_{\text{meas}}$ of the component (homo-) polymers in such a molecular weight distribution can be written as

$$M_{\text{meas}} = n \times M_{\text{mon}} + M_{\text{end}} + M_{\text{cat}} \tag{3.1}$$

Here, $n$ is the degree of polymerization, and $M_{\text{mon}}$, $M_{\text{end}}$and $M_{\text{cat}}$ are the mass of the repeating unit, the residue mass of the end group and the mass of the cation (or proton) respectively. Note that this expression holds only for the $^{12}$C monoisotopic peaks in the measured molecular weight distribution and that all ions are assumed to be singly charged. If component polymers that contain one or more $^{13}$C isotopes are considered, an additional term has to be introduced that incorporates the mass difference between $^{12}$C and $^{13}$C isotopes. Linear regression analysis on the measured molecular weights of an isotopically resolved selected series of cationized component polymer molecules as a function of the degree of polymerization will yield the mass of the repeating unit and the sum of the residue mass of the end group plus the mass of the cation. The slope of the fitted line gives the mass of the repeating unit and the intercept with the y-axis will represent the combined mass of the end group and the cation. There are two problems inherent to this method: first, the determination of the cation adduct; second, the assignment of the degree of polymerization to the different molecular peaks in the spectra. For many polymer samples the first problem can be solved by comparison of a series of measurements in which different alkali salts are successively added to the matrix as dopants. This addition of alkali salts will influence the abundance of the cationized species and it becomes possible to identify the different adducts. The assignment of the degree of polymerization is more ambiguous. A criterion for the assignment of $n$ is that the estimated end group mass corresponds with elemental compositions that are plausible in the context of reaction mechanisms in polymer synthesis and synthetic routes that lead to the polymer. Consequently, one has to evaluate in principle all possible end group masses given by

$$M_{\text{end}} = M_0 + i \times M_{\text{mon}} \tag{3.2}$$

(in which $M_0$ is the smallest possible end group mass and $i = 0, 1, 2, ...$).

In the foregoing method both the monomer mass and the end group mass are determined from the measured data. It is obvious that an error in the monomer mass determination will introduce a progressive error in the end group mass because of the extrapolation of the regression line necessary to find the intercept with the y-axis. Therefore, a significant improvement of the accuracy of the intercept can be obtained when the elemental composition of the repeating unit has been determined. In that case the slope of the line can be fixed to the actual residual monomer mass and only the intercept will be fitted. This method is equivalent to determination of the end group for each individual peak in the spectrum (by subtracting $n$ times the monomer mass from the measured mass) and subsequent averaging of the results.

The accuracy in the end group mass determination according to both methods can be compared by performing an error analysis. The uncertainty in the determination of the end group mass as a result of the (expectation value of the) accuracy of the mass measurements $\sigma_{\text{data}}$ using the first method (the regression method) is determined by the uncertainty in the estimation of the coefficients $a$ and $b$ in the fit of the straight line $Y = an + b$ through the set of data points. In this fit $a$ and $b$ reflect the monomer and the end group mass, respectively. The errors are found to be [101]:

$$\begin{aligned} \sigma_a^2 &= \frac{N\sigma_{\text{data}}^2}{N\sum_{i=1}^{N} n_i^2 - \left(\sum_{i=1}^{N} n_i\right)^2} \\ \sigma_b^2 &= \frac{\sigma_{\text{data}}^2 \sum_{i=1}^{N} n_i^2}{N\sum_{i=1}^{N} n_i^2 - \left(\sum_{i=1}^{N} n_i\right)^2} \end{aligned} \tag{3.3}$$

where $n_i$ is the degree of polymerization that corresponds to a measured mass $M_i$ and $N$ is the number of data points. The uncertainty in the determination of the end group mass is equal to $\sigma_b$. To compare the uncertainties for the two methods, eqns. 3.3 are simplified by considering the case in which the degrees of polymerization are distributed equally around the origin. This can be obtained for any data set by redefinition of the origin that performs the translation $n' = n - \bar{n}$ (where $\bar{n}$ is the average degree of polymerization), which is a linear transformation and therefore does not effect the magnitudes of the uncertainties. After transformation of the data, it follows from eqns. 3.3 that the uncertainties in fitting the line $Y' = a'n' + b'$ in the new coordinate system (note that primed symbols refer to the new coordinate system) are given by

$$\sigma'^2_a = \frac{\sigma^2_{\text{data}}}{\sum_{i=1}^N n'^2_i} \qquad \sigma'^2_b = \frac{\sigma^2_{\text{data}}}{N} \tag{3.4}$$

Insertion of $n' = n - \bar{n}$ into the expression for $\sigma'_a$ shows that the uncertainty in the parameters $a$ and $a'$ remains unchanged, that is, $\sigma'_a \equiv \sigma_a$. To find the mass of the end group in the new coordinate system, $n' = -\bar{n}$ is substituted into $Y' = a'n' + b'$, which results in

$$M_{\text{end}} = b' - a'\bar{n} \tag{3.5}$$

The corresponding uncertainty is obtained by calculation of the propagation of errors in the extrapolation [101]

$$\sigma^2_{\text{end}} = \sigma'^2_b + \bar{n}^2\sigma'^2_a = \frac{\sigma^2_{\text{data}}}{N} + \bar{n}^2\frac{\sigma^2_{\text{data}}}{\sum_{i=1}^N n'^2_i} \tag{3.6}$$

For the second method (the averaging method) the uncertainty in the determination of the end group mass as calculated from the propagation of errors [101] is given by

$$\sigma^2_{\text{end}} = \frac{\sigma^2_{\text{data}}}{N} \tag{3.7}$$

Comparison of eqns. 3.6 and 3.7 shows that the difference between the accuracies of the two methods is the (progressive) contribution of the uncertainty in the determined monomer mass $\sigma_a$. Higher end group mass accuracies are consequently obtained if the monomer elemental composition is known.

### 3.3.2 Tests of the Methodology on PEG1000 and PEG4000

The polymer samples investigated in a first set of experiments were polyethylene glycols with different molecular weight averages. Because these PEGs are reference samples with known polymer structure, system performance could be optimized and characterized in the course of these experiments. Figure 3.3 shows the MALDI-FTICR-MS spectrum of PEG1000 in broad band (mass range $m/z$ 500 - 5000) and two expansions of the mass scale. Sodium iodide was added to the matrix to increase the S/N ratio. The broad-band mass spectrum covers the entire molecular weight distribution of PEG1000. The resolution in broad band mode $(m/dm)_{50\%}$ is 30,000 with a S/N ratio of 100 at $m/z$ 921 for a sample amount of 10 ng on target. The right-hand inset shows that the resolution is sufficient to resolve the natural occurring $^{12}$C/$^{13}$C isotopes of the component molecules. Therefore, no further optimization of the mass resolving power was attempted. The molecular weight distribution is near Gaussian shaped as can be expected from the statistical nature of the polymerization process [102]. The spectrum predominantly shows

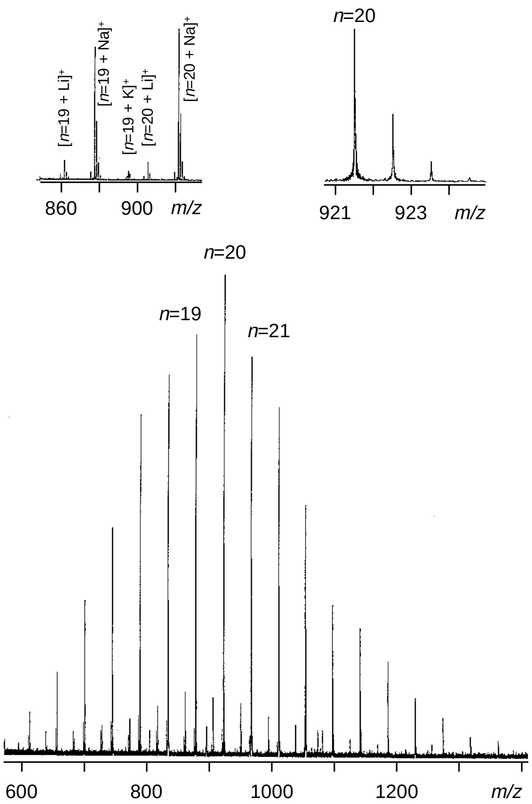

**Figure 3.3:** *Broadband MALDI-FTICR-MS spectrum of native PEG1000 with sodium iodide added to the matrix. Two expansions of the mass scale are given. The left-hand inset shows the different cation adducts and the right-hand inset shows the high resolution of the measurement (30,000).*

sodium cationized PEG molecules at equidistant intervals that are nominally 44 u. Also lithium and potassium cationized components are present at lower abundance. Matrix adduct ions are not observed. For example, the PEG nonadecamer pseudomolecular ions $[\mathrm{M{+}Li}]^+$, $[\mathrm{M{+}Na}]^+$ and $[\mathrm{M{+}K}]^+$ are observed at $m/z$ 861, $m/z$ 877, and $m/z$ 893, respectively (left-hand inset in Figure 3.3). The alkaline salt contamination from the sample preparation process was sufficient to produce the lithium and potassium cation adducts. The identity of the ionizing species was proved in a series of measurements in which the alkali salts lithium iodide, sodium iodide or potassium iodide were respectively added to the matrix (Figure 3.4) for the successive measurements. It can be seen from the mass shifts in the measured distributions in Figure 3.4 that these additions cause the com-

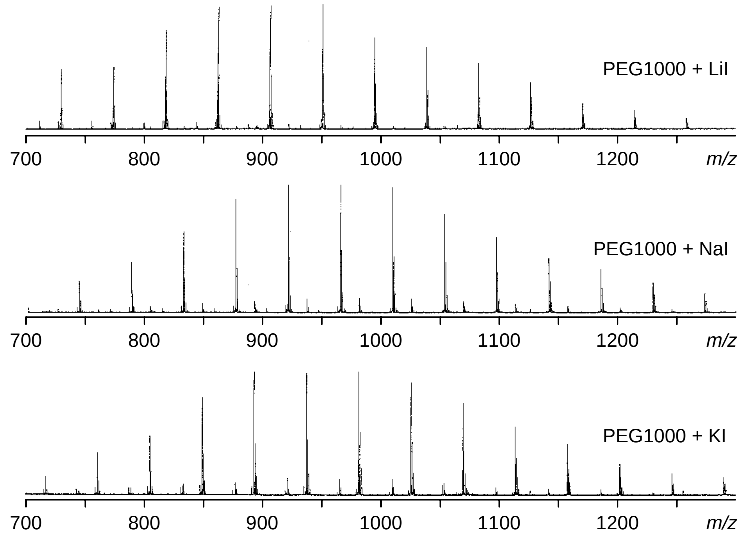

**Figure 3.4:** *Broadband MALDI-FTICR-MS spectrum of native PEG1000 with lithium, sodium, and potassium iodide, respectively, added to the matrix.*

ponent molecules to form the corresponding cation adducts. Finally, the lithium, sodium and potassium cationized perdeutero methylated PEG1000 molecular weight distributions were similarly measured (spectra not shown). The masses of all the measured PEG1000 peaks are listed in Table 3.1. The individual components of the molecular weight distributions were measured with a mass accuracy better than 8 ppm. The accuracy in the experimental data ($\sigma_{\text{data}}$) was assumed to be $8 \cdot 10^{-3}$ u (which corresponds to a mass accuracy of 8 ppm) for all components in the calculation of the uncertainties in the error analysis. This value changes only marginally over the relatively narrow mass range of interest. The measurements on PEG1000 as described in the preceding text were used to test the accuracy of the two methods of end group mass determination (eqns. 3.6 and 3.7). Only the peaks with S/N>10 were part of the calculations. The results are presented in Table 3.2. It is evident that both methods lead to an accuracy that is sufficient to confirm the identity of the distal parts of the polymer. As argued in Section3.3.1, the second method yields a higher accuracy for the end group mass. The errors in the determined end group masses are well in agreement with the predicted values, given the 8 ppm mass measurement accuracy.

After the encouraging results from the PEG1000, similar experiments were performed with PEG4000. The spectrum of the native PEG4000 is shown in Figure 3.5. The components of the molecular weight distribution are measured with a mass accuracy better than 15 ppm and their masses are listed in Table 3.3. The polymer ($n = 95$) at $m/z$ 4239 $[\text{M+K}]^+$ is resolved with a resolution of 6000 and a S/N ratio of 75. The polymer molec-

**Table 3.1:** *The measured masses of the components of the PEG1000 molecular weight distributions and the corresponding degree of polymerization* $n^*$

| $n$ | $[CD_3O$ –(···)– $CD_3+K]^+$ | $[CD_3O$ –(···)– $CD_3+Li]^+$ | $[CD_3O$ –(···)– $CD_3+Na]^+$ | [HO –(···)– H+Li]$^+$ | [HO –(···)– H+Na]$^+$ |
|---|---|---|---|---|---|
| 13 | | | 647.4081 | | 613.3384 |
| 14 | 707.4106 | 675.4617 | 691.4337 | 641.3891 | 657.3643 |
| 15 | 751.4368 | 719.4868 | 735.4623 | 685.4159 | 701.3918 |
| 16 | 795.4634 | 763.5145 | 779.4892 | 729.4439 | 745.4162 |
| 17 | 839.4909 | 807.5419 | 823.5145 | 773.4672 | 789.4445 |
| 18 | 883.5183 | 851.5663 | 867.5407 | 817.4949 | 833.4701 |
| 19 | 927.5440 | 895.5934 | 911.5668 | 861.5236 | 877.4956 |
| 20 | 971.5715 | 939.6196 | 955.5931 | 905.5470 | 921.5234 |
| 21 | 1015.5962 | 983.6456 | 999.6205 | 949.5742 | 965.5499 |
| 22 | 1059.6226 | 1027.6736 | 1043.6462 | 993.5971 | 1009.5764 |
| 23 | 1103.6456 | 1071.7010 | 1087.6736 | 1037.6250 | 1053.6008 |
| 24 | 1147.6751 | 1115.7285 | 1131.6983 | 1081.6543 | 1097.6229 |
| 25 | 1191.7000 | 1159.7523 | 1175.7244 | 1125.6790 | 1141.6498 |
| 26 | 1235.7216 | 1203.7772 | 1219.7547 | 1169.7014 | 1185.6777 |
| 27 | 1279.7584 | 1247.8005 | 1263.7776 | 1213.7335 | 1229.7017 |
| 28 | 1323.7756 | 1291.8335 | 1307.7954 | 1257.7552 | 1273.7362 |
| 29 | 1367.8143 | 1335.8586 | 1351.8314 | 1301.7752 | 1317.7501 |
| 30 | 1411.8354 | 1379.8839 | 1395.8468 | 1345.8129 | 1361.7832 |
| 31 | 1455.8645 | 1423.9114 | | | |

$^*$The chain of PEG monomeric units is denoted by –(· · ·)–.

**Table 3.2:** *Masses and deviations in the analysis of native and perdeutero methylated PEG1000 end groups by MALDI-FTICR-MS*$^*$

| Masses and Deviations (u) | $[CD_3O$ –(···)– $CD_3+K]^+$ | $[CD_3O$ –(···)– $CD_3+Li]^+$ | $[CD_3O$ –(···)– $CD_3+Na]^+$ | [HO –(···)– H+Li]$^+$ | [HO –(···)– H+Na]$^+$ |
|---|---|---|---|---|---|
| $M_{\text{mon, act}}$ | 44.0262 | 44.0262 | 44.0262 | 44.0262 | 44.0262 |
| $M_{\text{mon, regr}}$ | 44.0265 | 44.0264 | 44.0261 | 44.0261 | 44.0260 |
| $\Delta M_{\text{mon, regr}}$ | 0.0003 | 0.0002 | -0.0001 | -0.0001 | -0.0002 |
| $\sigma_{\text{mon, regr}}$ | 0.0004 | 0.0004 | 0.0004 | 0.0004 | 0.0004 |
| $M_{\text{end, act}}$ | 91.0432 | 59.0955 | 75.0693 | 25.0260 | 40.9998 |
| $M_{\text{end, regr}}$ | 91.0392 | 59.0913 | 75.0708 | 25.0244 | 41.0012 |
| $\Delta M_{\text{end, regr}}$ | -0.0041 | -0.0042 | 0.0015 | -0.0016 | 0.0014 |
| $\sigma_{\text{end, regr}}$ | 0.0084 | 0.0084 | 0.0080 | 0.0089 | 0.0080 |
| $M_{\text{end, av}}$ | 91.0460 | 59.0963 | 75.0685 | 25.0227 | 40.9971 |
| $\Delta M_{\text{end, av}}$ | 0.0028 | 0.0008 | -0.0008 | -0.0034 | -0.0027 |
| $\sigma_{\text{end, av}}$ | 0.0019 | 0.0019 | 0.0019 | 0.0019 | 0.0019 |

$^*$These results were obtained using the masses listed in Table 3.1. $\Delta$ denotes the difference between the actual and the estimated mass. The standard deviations $\sigma_{\text{mon}}$ and $\sigma_{\text{end}}$ were calculated from eqns 3.3, 3.6 and 3.7. The $\sigma_{\text{data}}$ is taken to be $8 \cdot 10^{-3}$ u. The chain of PEG monomeric units is denoted by –(· · ·)–.

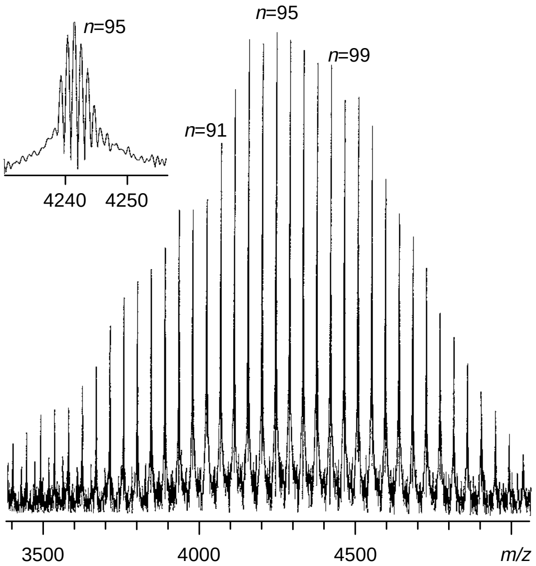

**Figure 3.5:** *Broadband MALDI-FTICR-MS spectrum of native PEG4000. The inset shows the unit mass resolved peak at* $m/z$ *4239.*

ular weight distribution covers the mass range $m/z$ 3400 - 5200 (S/N>2). To test the accuracy of the methods and the experimental conditions, the dipropylether and the diacetate of PEG4000 were studied in addition to the native PEG4000. The residual masses of the dipropyl and diacetate end groups differ only by $72 \cdot 10^{-3}$ u. Consequently, a resolving power of at least 56,000 at $m/z$ 4000 is required to distinguish the two derivatives. The measured molecular weight distributions of the derivatized PEG4000 compounds were similar to those from native PEG4000 and the masses determined from these spectra are also listed in Table 3.3. It is obvious that the resolution in broad band mode is not sufficient to resolve the two derivatives in one spectrum. On the other hand, the mass accuracy should be sufficient to distinguish the two derivatives on the basis of end group mass determinations from different measurements. The results of the analysis of the data are listed in Table 3.4. The uncertainties in the error analysis are calculated by taking $60 \cdot 10^{-3}$ u as the accuracy in the experimental data $\sigma_{\text{data}}$ (which corresponds to 15 ppm mass accuracy at $m/z$ 4000). Note that the peaks in the spectrum, which correspond to polymers that contain two $^{13}$C isotopes, have the highest abundance in the mass range around $m/z$ 4000. These are therefore used for the end group analysis. The identification of these peaks is based on calculated isotopic patterns. The implication of this choice is that the determined end group masses will be the summation of the end group mass, the mass of the cation and the mass difference between $^{12}C_2$ and $^{13}C_2$.

It is concluded from the results that the regression method becomes less accurate for

**Table 3.3:** *The measured masses of the components of the PEG4000 molecular weight distributions and the corresponding degree of polymerization* $n^*$

| *n* | [HO –(···)– H+K]$^+$ | [CH$_3$(CO)O –(···)– (CO)CH$_3$+Na]$^+$ | [C$_3$H$_7$O –(···)– C$_3$H$_7$+Na]$^+$ |
|---|---|---|---|
| 78 | | 3561.130 | |
| 79 | | 3605.151 | |
| 80 | | 3649.173 | |
| 81 | | 3693.246 | 3693.145 |
| 82 | | 3737.280 | 3737.182 |
| 83 | | 3781.298 | 3781.223 |
| 84 | | 3825.290 | 3825.260 |
| 85 | 3785.265 | 3869.350 | 3869.261 |
| 86 | 3829.291 | 3913.363 | 3913.284 |
| 87 | 3873.255 | 3957.389 | 3957.319 |
| 88 | 3917.258 | 4001.410 | 4001.342 |
| 89 | 3961.342 | 4045.440 | 4045.369 |
| 90 | 4005.355 | 4089.462 | 4089.403 |
| 91 | 4049.355 | 4133.486 | 4133.419 |
| 92 | 4093.393 | 4177.523 | 4177.442 |
| 93 | 4137.418 | 4221.563 | 4221.486 |
| 94 | 4181.472 | 4265.576 | 4265.510 |
| 95 | 4225.486 | 4309.593 | 4309.541 |
| 96 | 4269.525 | 4353.622 | 4353.556 |
| 97 | 4313.557 | 4397.655 | 4397.576 |
| 98 | 4357.574 | 4441.665 | 4441.614 |
| 99 | 4401.540 | 4485.732 | 4485.627 |
| 100 | 4445.613 | 4529.722 | 4529.665 |
| 101 | 4489.715 | 4573.738 | 4573.688 |
| 102 | 4533.703 | 4617.754 | |
| 103 | | 4661.813 | |
| 104 | | 4705.852 | |
| 105 | | 4749.851 | |

$^*$The chain of PEG monomeric units is denoted by –(· · ·)–.

higher masses because of the large effect of the extrapolation. Furthermore, the results show that the predicted errors are much higher than the actual errors. This difference is caused by a relatively large variation of $\sigma_{\text{data}}$ over the molecular weight distribution (roughly a factor of 2), which implies that the assumption of a constant measurement uncertainty no longer holds. The error from the averaging method still allows the confirmation of the identity of the end groups with an accuracy within $20 \cdot 10^{-3}$ u. This means that it is possible to distinguish between the two derivatives with isobaric nominal end group mass using end group determinations according to the averaging method. Because the error in the averaging method scales linearly with the error in the experimental data, this method is expected to work for molecular weights up to roughly $m/z$ 10,000 provided that the measured spectra will be unit mass resolved.

**Table 3.4:** *Masses and deviations in the analysis of native, dipropyl, and diacetyl PEG4000 end groups by MALDI-FTICR-MS*$^*$

| Masses and Deviations (u) | [HO –(···)– H+K]$^+$ | [$CH_3$(CO)O –(···)– (CO)$CH_3$+Na]$^+$ | [$C_3H_7$O –(···)– $C_3H_7$+Na]$^+$ |
|---|---|---|---|
| $M_{\text{mon, act}}$ | 44.0262 | 44.0262 | 44.0262 |
| $M_{\text{mon, regr}}$ | 44.0285 | 44.0264 | 44.0264 |
| $\Delta M_{\text{mon, regr}}$ | 0.0023 | 0.0002 | 0.0002 |
| $\sigma_{\text{mon, regr}}$ | 0.0025 | 0.0014 | 0.0020 |
| $M_{\text{end, act}}$ | 43.007 | 127.101 | 127.028 |
| $M_{\text{end, regr}}$ | 42.79 | 127.09 | 127.02 |
| $\Delta M_{\text{end, regr}}$ | -0.22 | -0.02 | -0.01 |
| $\sigma_{\text{end, regr}}$ | 0.24 | 0.13 | 0.18 |
| $M_{\text{end, av}}$ | 43.004 | 127.106 | 127.039 |
| $\Delta M_{\text{end, av}}$ | -0.003 | 0.005 | 0.011 |
| $\sigma_{\text{end, av}}$ | 0.014 | 0.011 | 0.013 |

$^*$These results were obtained using the masses listed in Table 3.3. $\Delta$ denotes the difference between the actual and the estimated mass. The standard deviations $\sigma_{\text{mon}}$ and $\sigma_{\text{end}}$ were calculated from eqns 3.3, 3.6 and 3.7. The $\sigma_{\text{data}}$ is taken to be $60 \cdot 10^{-3}$ u. The chain of PEG monomeric units is denoted by –(· · ·)–.

### 3.3.3 Application: End Group Analysis of Polyvinyl Pyrrolidone with Unknown End Groups

The experiments described in the preceding text demonstrate the validity of the end group determination via MALDI-FTICR-MS. In a second series of experiments, a polymer sample with an unknown end group structure was investigated. The spectrum of this compound, polyvinyl pyrrolidone (PVP3000), in Figure 3.6 shows abundant [M+Na]$^+$ cations. The identity of these sodium adducts was confirmed by comparison of the spectrum with the result of a second measurement in which potassium iodide was added to the matrix, similar to the experiments presented in Figure 3.4 (data not shown). The molecular weight distribution was again measured in broadband mode. The masses of the component [M+Na]$^+$ ions (listed in Table 3.5) were correlated with the degree of polymerization. The resulting end group and monomer masses are also given in Table 3.5. According to the average method the possible end group (without cation adduct) masses are $60.0588 + i * 111.0684$. For $i = 0$, the end group mass is indicative for the elemental composition $C_3H_8O$. Isopropanolate anions are well recognized initiators in base-induced polymerization of PVP. In this anionic polymerization reaction the alkyl group of the initiator is incorporated in one of the end groups of the reaction product. Generally, these polymerization reactions are quenched by the addition of H$^+$. Therefore, it is concluded that the end groups of the PVP3000 polymer are (CH3)$_2$CHO- and H-. For $i > 0$, there are no plausible candidates for the end group of the polymer based on polymer chemical synthesis. This end group assignment was confirmed by the supplier.

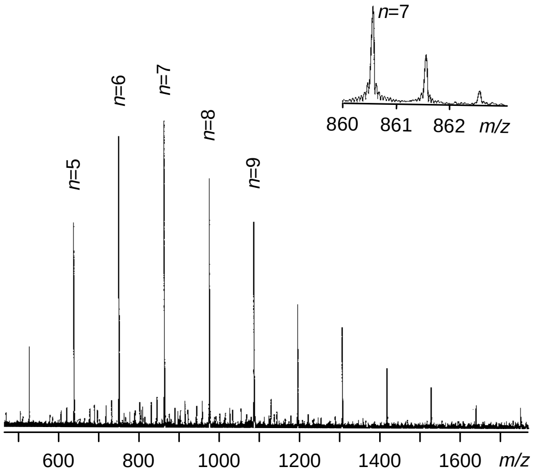

**Figure 3.6:** *Broadband MALDI-FTICR-MS spectrum of PVP3000 with unknown end group structure.*

**Table 3.5:** *The measured masses of the components of the PVP3000 molecular weight distributions for the different degrees of polymerization* $n$ *and the results of the end group analysis of these data**

| $n$ | $[(CH_3)_2CHO{-}(\cdots){-}H+Na]^+$ | Masses and Deviations (u) | |
|---|---|---|---|
| 4 | 527.3247 | $M_{mon, act}$ | 111.0684 |
| 5 | 638.3927 | $M_{mon, regr}$ | 111.0667 |
| 6 | 749.4606 | $\Delta M_{mon, regr}$ | -0.0017 |
| 7 | 860.5268 | $\sigma_{mon, regr}$ | 0.0012 |
| 8 | 971.5933 | $M_{end, act}$ | 83.0473 |
| 9 | 1082.6618 | $M_{end, regr}$ | 83.0591 |
| 10 | 1193.7240 | $\Delta M_{end, regr}$ | 0.0118 |
| 11 | 1304.7931 | $\sigma_{end, regr}$ | 0.0097 |
| | | $M_{end, av}$ | 83.0465 |
| | | $\Delta M_{end, av}$ | -0.0008 |
| | | $\sigma_{end, av}$ | 0.0028 |

* $\Delta$ denotes the difference between the actual and the estimated mass. The standard deviations $\sigma_{\mathrm{mon}}$ and $\sigma_{\mathrm{end}}$ were calculated from eqns. 3.3, 3.6 and 3.7. The chain of PVP monomeric units is denoted by $-(\cdots)-$.

## 3.4 Mass Discriminations Induced by Mass Dependent Flight-Times

### 3.4.1 Examination of Flight-Time Induced Distortions in Measured Molecular Weight Distributions

With external ion source MALDI-FTICR-MS, the ions are created ∼1.5 m from the ICR cell using a short duration (600 picoseconds) laser pulse and subsequently transferred to the ICR cell for detection. This is illustrated in Figure 3.7. Figure 3.7 A is the standard experimental sequence (used to generate the data in Figure 3.8). According to this sequence, the laser is fired, the ions are directed onto the analyzer cell, and the cell is gated to admit ions at the same time. After the variable trapping time all voltages are reset. Figure 3.7 B is a modified experimental sequence (used to generate the data in Figure 3.10) which will be discussed further below.

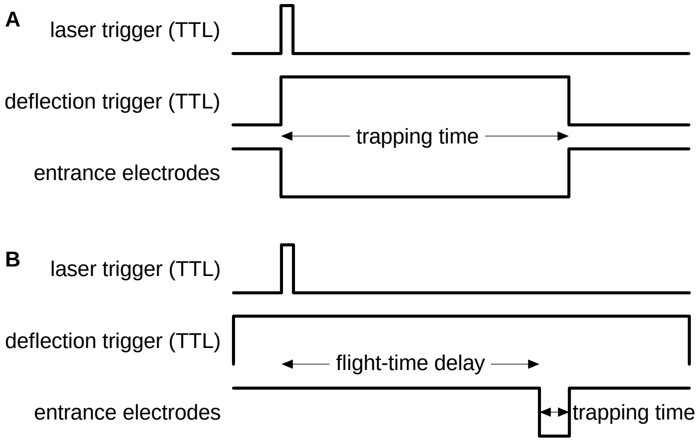

**Figure 3.7:** *(A) Standard trapping pulse sequence. Ions are injected into the analyzer cell when the deflection trigger is high (that is, the ions are directed onto the cell entrance) and the entrance electrodes are low. (B) The modified trapping pulse sequence to characterize arrival time profiles and residence times.*

It is obvious that any post-source acceleration of the ions for transport to the cell induces a mass-dependency in the flight-time. This means that different masses will arrive at different times at the entrance of the cell. In combination with the finite ion accumulation time, this will create a flight-time induced mass discrimination and polymer molecular weight distributions will become distorted. In order to examine these flight-time induced distortions in the measured molecular weight distributions, a series of PEG spectra were acquired at different trapping times. These are plotted as a contour plot in Figure 3.8. In the contour plot, 60 evenly spaced contour levels were used with the lowest contour set at 3 times the root-mean-square (rms) noise level and the highest contour set

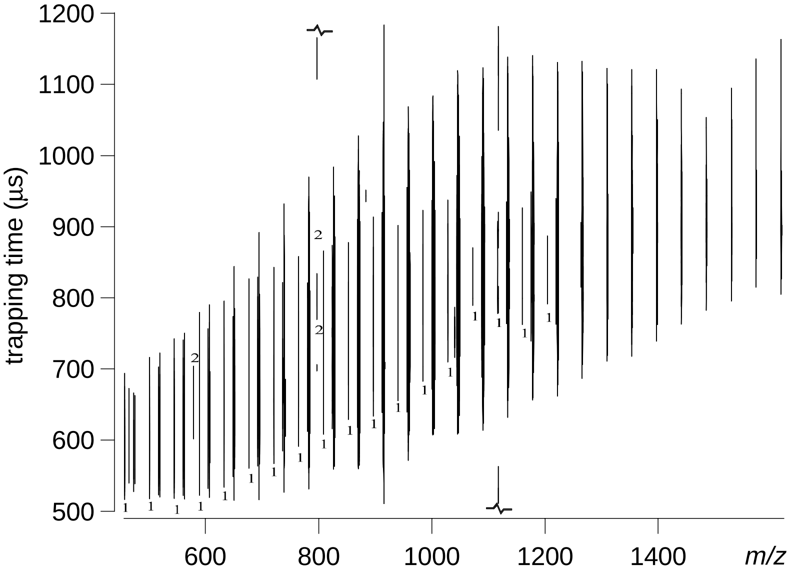

**Figure 3.8:** *Contour plot of the poly(ethylene glycol) distributions as a function of trapping time. The main distribution is sodiated, but "1" indicates additional lithiated peaks while "2" indicates potassiated peaks. The "∼" sign indicates a laboratory noise peak.*

to the intensity of the most abundant peak in the complete series of spectra. It reveals that there is a significant distortion in the measured molecular weight distribution and that this distortion shifts as a function of the trapping time. This is easily explained on basis of the distance between the ion source and the ICR cell and the pulsed nature of both the ionization and the analysis event. After all, the ion packet created in the MALDI ionization event is post accelerated to 3 keV to penetrate the inhomogeneous strayfield of the magnet and then decelerated for trapping. The different masses present in the ion packet will therefore separate in space during the transport, and a mass dependent time of arrival at the cell entrance is the result. Of course, the mass-independent velocity distributions in the MALDI process [96] and variations in the exact point in space and time of ionization cause a distribution in this arrival time. On the other hand, ions arriving at the entrance will enter the cell as long as the entrance channel is open. After being reflected at the rear end of the cell, they will fall back out the entrance channel if it is still open. Therefore, the combination of the moment that the entrance channel is closed (i.e., the trapping time) and the residence time of the ions in the cell determines which segment of the packet will be analyzed.

### 3.4.2 Correction of Flight-Time Induced Distribution Shifts

A useful feature of this flight-time induced mass discrimination is that it prevents the analyzer cell from filling to its space-charge limit with low-mass matrix ions prior to the arrival of the ions of interest. However, it necessitates a compensation for this mass discrimination in the data analysis in order to accurately characterize molecular weight distributions. A method has been described in the literature for the compensation of mass-selective trapping in MALDI-FTICR-MS experiments in an internal source geometry using gated deceleration potentials [92, 99, 100]. According to this method, a series of spectra is acquired at different trapping times and linearly summing these spectra leads to the correct molecular weight distribution [92]. The thought experiment illustrated in Figure 3.9 shows that this approach does not lead to the real molecular weight distributions in the case of an external ion source geometry. The following assumptions are made in this thought experiment:

1. The number of ions with mass $m_i$ arriving at the cell entrance follows the Gauss function.
2. The average time of arrival $t_{\text{arr}}$ of these ions is linearly proportional to $m_i$.
3. The width of the Gauss function is equal to twice the difference in the arrival time of two adjacent polymer peaks (i.e., $t_{\text{arr}}(m_i) - t_{\text{arr}}(m_{i-1})$).
4. The residence time of the ions inside the cell is mass-independent and equal to $t_{\text{arr}}(m_i) - t_{\text{arr}}(m_{i-9})$.
5. Experiments are performed for $t_{\text{trap}} = t_{\text{arr}}(m_5)$, $t_{\text{arr}}(m_{12})$, and $t_{\text{arr}}(m_{17})$.
6. Each oligomer in the comb-like polymer distribution that is plotted in Figure 3.9 B has equal intensity.

The first three assumptions lead to the theoretical profile depicted in Figure 3.9 A. The remaining three produce the theoretically "measured" spectra that are drawn in Figure 3.9 C. The sum of these spectra is presented in Figure 3.9 D, which demonstrates that this method leads to an exaggeration of the overlapping regions relative to the rest of the oligomers.

The assumptions made in the thought experiment make it possible to apply an alternative correction method. A direct consequence of the assumptions is that the residence time of the ions inside the analyzer cell is much larger than the widths of their arrival time profiles. This means that it is possible to acquire a spectrum for each component in the polymer distribution in which the component's arrival time profile coincides entirely with the segment of the ion packet that is trapped. A complete set of such spectra is obtained in a series of MS experiments in which the trapping time is increased in steps smaller than the difference between the width of the arrival time profile and the residence time. Superimposing the spectra such that the intensity of each component is equal to its maximum intensity in the set will thus reveal the original polymer distribution. The

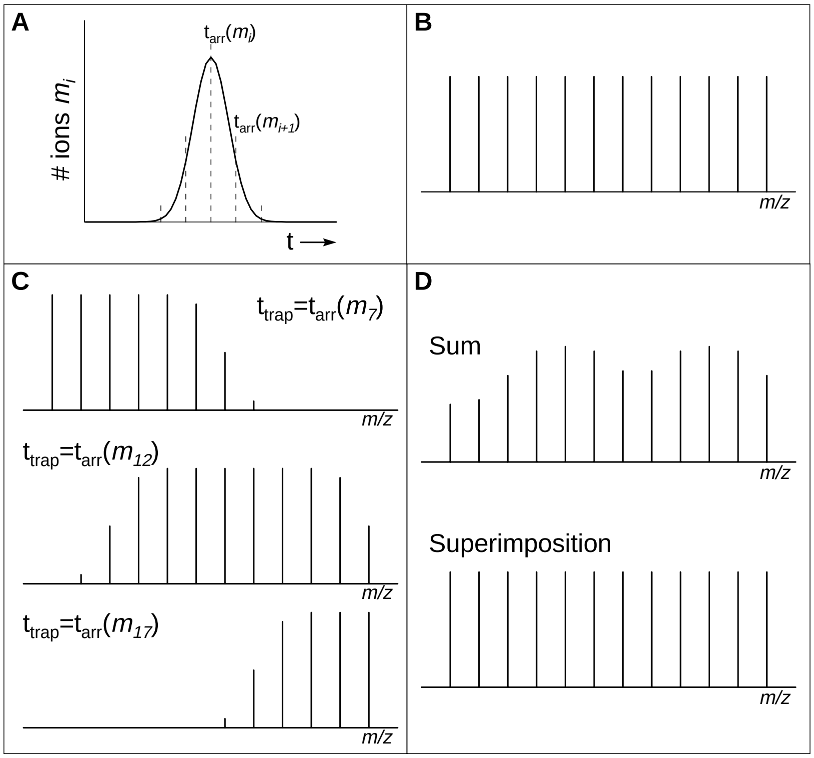

**Figure 3.9:** *Thought experiment for the development of a method for compensation of flight-time induced mass discrimination effects. Depicted are (A) the assumed number of ions at* $m/z\ m_i$ *arriving at the analyzer cell as a function of time, (B) a theoretical comb-like polymer distribution, (C) theoretical "measured" spectra for different trapping delays, and (D) overall spectra obtained by summation and projection, respectively, of the individual "measured" spectra.*

result of this method applied to the thought experiment is also included in Figure 3.9 D, which demonstrates that it leads to an accurate representation of the theoretical "comb" distribution.

Thus, application of the superimposition method to the experiments presented in Figure 3.8 requires the fulfillment of the following two conditions:

1. The arrival time profile is substantially smaller that the residence time.

2. The increase in trapping time between subsequent spectra in the set is smaller than the difference between the width of the arrival time profile and the residence time.

Fulfillment of these conditions was examined by characterization of the arrival time profiles and the residence times of the various components in the PEG molecular weight distribution. For these experiments, the pulse sequence was modified as illustrated in Figure 3.7. Figure 3.7 A shows the standard trapping pulse sequence that was used to produce the data in Figure 3.8. In the modified sequence (depicted in Figure 3.7 B) the potential on the deflection electrodes was lowered to the entrance potential prior to the laser pulse to allow all ions to get to the cell entrance. Following a variable flight-time delay, which determines the segment of the ion packet to be sampled, the entrance electrodes were gated open for 100 $\mu$s. This flight-time window was shifted across the ion packet profile to obtain the required detailed insight in the flight-time profiles of the individual components. The resulting data are plotted as before in a contour plot with 60 evenly spaced constant level contours with the lowest contour set at 3 times the rms noise level and the highest contour set to the intensity of the most abundant peak in the complete series of spectra in Figure 3.10. In comparison to Figure 3.8, the various oligomers' flight-times shifted to a shorter time scale. This is caused by the 100 $\mu$s difference in the definition of the trapping

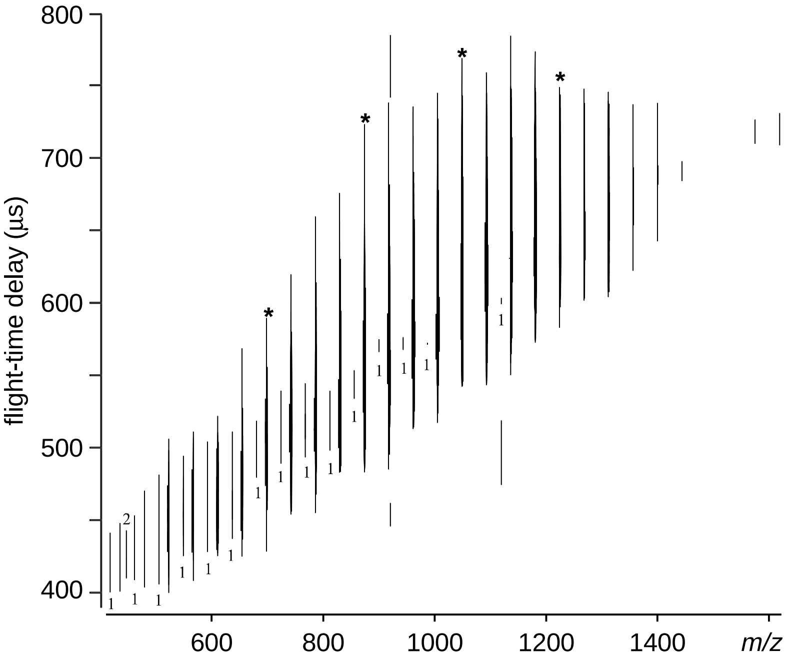

**Figure 3.10:** *Contour plot of the poly(ethylene glycol) distributions measured with the modified trapping pulse sequence as a function of the flight-time delay. These ions are primarily sodiated although some lithiated ions are observed (marked "1"). The line marked "2" indicate $3\omega_+$ harmonic peaks.*

time and the flight-time delay. More important is that the distributions are narrower in time, which reflects the sampling of the profile instead of the ion residence times in the cell. The arrival time profiles are characterized by the flight-time delay cross sections that are plotted in Figure 3.11 for the peaks marked with an asterisk in Figure 3.10. It is seen that the center of the cross sections shifts 125 $\mu$s for the oligomer at $m/z$ 701 to the one at $m/z$ 1229. This expresses the shift in arrival time due to different flight-times. The width of the arrival time profiles can be estimated on the basis of the width of the cross sections, which is observed to be only slightly larger than the time that the cell was gated open (<150 $\mu$s). Recall that this width is determined by the sum of the trapping time and the width of the arrival time profile. Therefore, it can be concluded that the latter is substantially smaller than 100 $\mu$s. Of course, this only applies if there is no leakage of ions with kinetic energies larger than the trapping voltage into the cell. Although the modified pulse sequence allows such leakage, it is suggested by the absence of a significant high-velocity tail in the cross sections shown that this effect does not significantly perturbs the analysis. Moreover, the same sequence was run without gating the cell open and in these experiments leakage was found to be negligible.

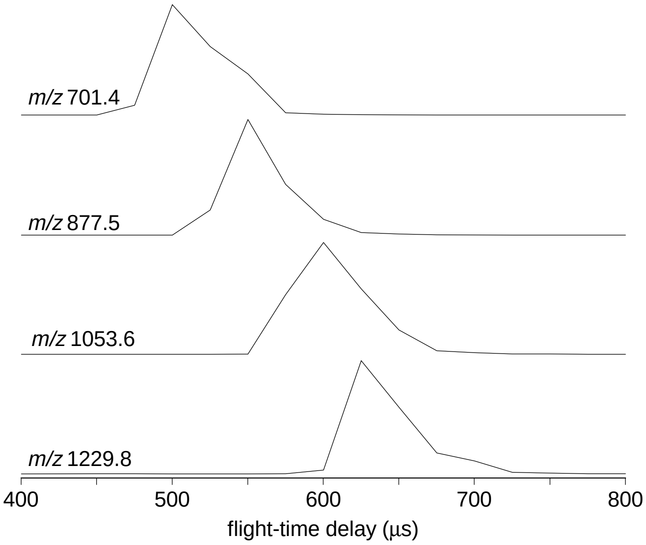

**Figure 3.11:** *Delay time cross sections from Figure 3.10 indicating the arrival time profiles of the PEG ions.*

Let's return to the results presented in Figure 3.8 (with no 100 $\mu$s window). There, the range of trapping times in which a specific component is detected, is determined by the sum of the width of its arrival time profile and its residence time. It is seen in the figure that this sum is typically 400-500 $\mu$s, which means that the residence time is roughly a factor of 10 larger than the width of the arrival time profile. Consequently, the superimposition method applied to a series of experiments in which the trapping time is increased by $\sim 50$ $\mu$s between two experiments results in the correct molecular weight distributions.

### 3.4.3 Application: Determination of the Molecular Weight Distribution of a Polystyrene Sample

It was investigated to what extent the superimposition and the sum method lead to different characterizing molecular weight averages for a polystyrene SEC calibration standard. Polystyrene has traditionally been a difficult molecule to analyze by MALDI, but several recently reported matrices [18] have made this ionization possible. The results are presented in Figure 3.12 A in the usual contour plot. The superimposition and the summation of the individual spectra are plotted in Figure 3.12 B and 3.12 C, respectively. Both overall molecular weight distributions are centered around $m/z$ 1250. The peaks in the spectra correspond to the polystyrene components of the form $[C_4H_9\text{-}(C_2H_3(C_6H_5))_n\text{-H+Ag}]^+$ ions with an end group mass of nominally 58 u + $Ag^+$ and a monomer mass of nominally 104 u. The $Ag^+$ with its two roughly equally abundant isotopes at 106 u and 108 u gives the isotopic pattern shown in the inset. The number average-molecular weight ($M_n = \sum_i M_i N_i \sum_i N_i$, with $M_i$ and $N_i$ the mass and abundance, respectively, of the polymer component $i$), the weight-average molecular weight ($M_n = \sum_i M_i^2 N_i \sum_i M_i N_i$), and the polydispersity factor ($M_w/M_n$) were calculated for both distributions. The results are listed in Table 3.6. The previous observation that the sum method underestimates the wings of the distribution is reflected in the polydispersity factors. These show that the width of the distribution obtained from the sum method is slightly smaller in comparison to the one obtained from the superimposition method. Of course, the differences between the calculated numbers are too small to be reflected in measurable physical properties of the polymer. It must be noted that this is partly due to the limited number of peaks that were part of the calculation (the measured mass range extended not over the entire molecular weight distribution). The difference in results obtained by the two methods manifests more clearly in a comparison of the S/N ratios in the spectrum. The S/N ratio in the superimposition spectrum (Figure 3.12 B) and the sum spectrum (Figure 3.12 C) are about equal in the center of the distribution (S/N=23 vs 22

**Table 3.6:** *$M_n$, $M_w$, and $M_w/M_n$ determined from the total polystyrene molecular weight distribution reconstructed by superimposing and summing, respectively, the individual distributions.*

| | Superimposition | Sum | Difference |
|---|---|---|---|
| $M_n$ | 1135 | 1153 | 1.6 % |
| $M_w$ | 1192 | 1205 | 1.1 % |
| $M_w/M_n$ | 1.05 | 1.045 | 0.5 % |

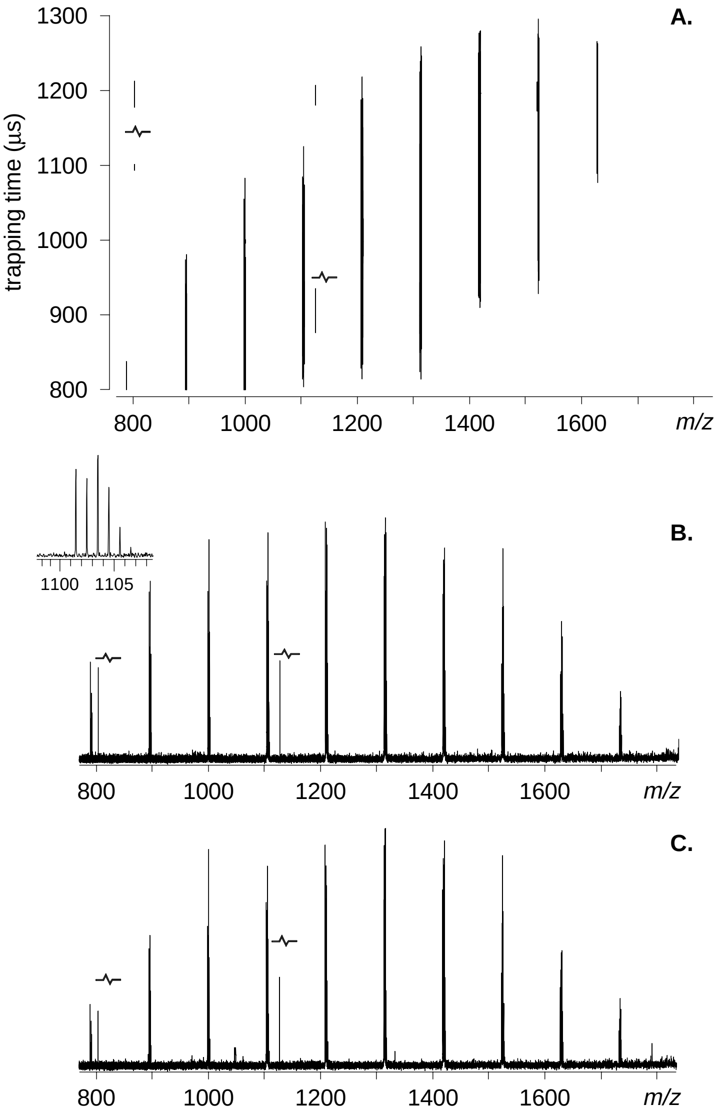

**Figure 3.12:** *Polystyrene molecular weight distribution measured by MALDI-FTICR-MS at different trapping times. Shown are the contour plot(A) and the total molecular weight distributions as obtained by superimposition (B) or summation (C) of the individual distributions. The isotopic pattern shown in the inset confirms the presence of the* $Ag^+$ *as cation adduct.*

for $m/z$ 1310). In the wings of the distribution, however, the sum spectrum exhibits an underestimation of S/N by $\sim 30\%$ (S/N=9.3 vs 6.3 for $m/z$ 780), which clearly demonstrates that the sum method does not fully compensate for the distortions in the measured distributions.

Finally, it is interesting to note that the molecular weight of this molecular standard was listed with a peak mass of 950 u, whereas the spectra in Figure 3.12 reveal a peak mass of 1250 u. Discrepancies between molecular weight distributions measured by MALDI mass spectrometry and distributions obtained by size-exclusion chromatography (SEC), have also been observed by Montaudo et al. [103] for polydisperse distributions. These observations have been supported by theoretical considerations by Jackson and coworkers [104, 105]. The discrepancies are caused by the fundamental difference between the measurement of the *number* fraction versus $m/z$ (as in MS) and the *weight* fraction versus the logarithm of the molecular mass (as in SEC). The consequence is that the high mass tail of the polydisperse distribution disappears much earlier into the baseline noise in MS measurements compared to analyses by SEC. This is in accordance with the results of Jackson et al. [104], which indicate that the peak mass value of a polymeric distribution measured by mass spectrometry should be two oligomers *lower* in mass than the same sample studied by chromatographic methods. However, this does not explain the discrepancy observed in Figure 3.12, where the peak mass is approximately two oligomers *higher* in mass, which implies an even greater error. There was no indication found for mass discrimination effects that could possibly reconcile the measured discrepancy. Therefore, it is presently assumed that the specified peak mass of 950 u is in error and that chromatographic calibration with this polystyrene standard would give a low-mass "error" of $\sim 20\%$.

## 3.5 Summary and Conclusions

The determinations of the exact elemental composition of the repeating units and end groups of low molecular weight polymers demonstrate that the newly configured external ion source MALDI-FTICR-MS is an instrument with superior mass accuracy. Two methods were evaluated for the determination of end group masses: linear regression on the molecular weights versus the degree of polymerization, and the averaging of the end group masses as determined from each individual peak in the mass spectrum. The methods were applied to native, perdeutero methylated, propylated, and acetylated PEG samples, and to a PVP sample with unknown end group elemental composition. The measurements in the mass range $m/z$ 500 - 1400 allow the determination of the masses of the component polymers with a mass accuracy of better than 8 ppm, leading to end group determinations with an accuracy within $10 \cdot 10^{-3}$ u and $3 \cdot 10^{-3}$ u, respectively, for the two methods. By virtue of this high accuracy it was possible to determine unambiguously that the elemental compositions of the PVP end groups were (CH3)$_2$CHO- and H-. Measurements in the mass range $m/z$ 3400 - 5000 could be performed at mass accuracies better than 15 ppm. This allows the end group mass determination with an accuracy of $240 \cdot 10^{-3}$ u and $20 \cdot 10^{-3}$

u, respectively. It clearly illustrates that the accuracy in the end group masses determined by the regression method decreases drastically with increasing mass. The accuracy in the determination of the monomer mass scales only with the accuracy in the molecular weight assignment of the individual components, and is still sufficient to validate proposals for the elemental composition of the monomeric unit. The latter applies also to the error in the end group determination by the averaging method. It is therefore expected that the combination of both methods applied to MALDI-FTICR-MS data allows the identification of the elemental composition of the different parts of synthetic (home-)polymers in the mass range up to $m/z \sim 10,000$.

The results also demonstrate that quantitative measurements with external ion source MALDI-FTICR-MS are complicated by flight-time induced mass discriminations. In addition to discrimination effects and chemical distortions in the plume [98], MALDI can cause different kinetic energy profiles for different masses [92]. This is true for all MALDI-FTICR systems, but it is particularly pronounced if the ions are produced in an external ion source. In such a geometry, the distance between the ion source and the mass spectrometer is often more than a meter, leading to a significant time of flight broadening. External injection ion optics accelerate the ions through the fringing magnetic field, which further distorts the initial velocities. Although this is useful to prevent low mass matrix ions from loading the cell to the space charge limit, it also distorts molecular weight distributions. Hence, it is necessary to acquire a series of spectra in different time of flight windows. Superimposition of these spectra so that the total oligomer intensity is equal to its maximum intensity in the set yields accurate molecular weight distributions on polymeric systems. This technique was used to demonstrate an error of ∼20% in the specified peak mass of the molecular weight distribution of a polystyrene standard.

# 4

# Determination of the Individual Block Length Distributions of poly(oxypropylene) and poly(oxyethylene) Block Copolymers by MALDI-FTICR-MS

*External ion source MALDI-FTICR-MS was used to analyze the block length distributions of triblock polymers of poly(oxypropylene) and poly(oxyethylene) (EOPO). The results presented demonstrate that flight-time induced mass discrimination (see Chapter 3), which distorts molecular weight distributions generated by MALDI in external ion source FTICR-MS, is not the only effect that must be considered before accurate information on block length distributions can be obtained. The variation of isotopic patterns over the measured mass range and overlap of peaks in the spectrum also complicate the analysis of the block length distributions. An analytical treatment of the spectral data is presented to correct measured molecular weight distributions for these effects. The corrected EOPO molecular weight distribution was used to determine the individual block length distributions. By virtue of this methodology it was possible to obtain for the first time detailed and accurate molecular weight data on such a complex sample. The results independently validate the data provided by the manufacturer. The experimentally verified random coupling hypothesis supports the validity of the flight-time correction method and the proposed treatment of the spectral data.*

## 4.1 Introduction

In Chapter 3, the properties of polymer molecular weight distributions were utilized to characterize and optimize the performance of external ion source MALDI-FTICR-MS with respect to mass accuracy and flight-time induced mass discrimination. The results clearly demonstrated that MALDI-FTICR-MS can provide detailed information on the individual components of polymeric samples based on the technique's unequaled mass accuracy and mass resolving power. A superimposition methodology was proposed to compensate for mass distortions induced by mass dependent flight-times, which allowed accurate description of polymer molecular weight distributions. Together, these properties make the technique well suited for many of the questions addressed in polymer analysis [61,77,90,91,106–113]. The methodology is evaluated in this chapter by the investigation of a Pluronic block copolymer.

Pluronics are water-soluble triblock polymers of poly(oxypropylene) and poly(oxyethylene) and find widespread application as nonionic surface-active agents. The surfactant properties of polyoxyalkylene block copolymers have been utilized as lubricants, dispersants, antistatic agents, foam control agents, solubilizers, and numerous other applications in the areas of pharmaceuticals, cleaning agents, foods and personal care products [114, 115]. The diversity in applications results from the various structural possibilities of poly(oxyalkylene) block copolymers. In these materials, ethylene oxide blocks provide the hydrophilicity and propylene oxide blocks the hydrophobicity necessary for surfactancy. The chemical composition can be optimized to achieve the desired surfactant performance. A complete description of the molecular composition distribution of the individual blocks in the copolymer is required to understand the structure-function relationships of surfactants with respect to physical, rheological, and mechanical properties. Important information is the detailed knowledge about the sequence and distributions of EO and PO blocks, the degree of polymerization and block size, the identity and structure of particular end groups (initiator and terminator type), and the presence of impurities. Various analytical approaches have been followed to investigate these properties. Detailed reviews on the analysis of poly(oxyalkylene) nonionic surfactants [116–119] describe useful methods such as liquid chromatography, infrared spectroscopy, raman spectroscopy, viscosimetry, calorimetry and NMR spectroscopy. In general, these methods provide only average data on specific structural features and are not suitable for the characterization of the individual components of the polymeric samples. In recent years, it has been demonstrated that mass spectrometric methods in combination with soft ionization techniques such as MALDI [18, 32, 33, 79] can provide this information [95].

In this Chapter, a method is developed to process spectral data obtained by MALDI-FTICR-MS to yield the individual block length distributions in a Pluronic sample. The Pluronic sample is a challenging test case as its constituent monomer units are small relative to the overall size of the copolymer, which means that overlap between different components of the molecular weight distribution is likely and high resolution mass spectrometry is imperative. It is demonstrated that the Pluronic sample offers a unique possibility to test the corrections on distortions induced by the experimental technique. An equal distribution in the block length of one of the constituents for different block lengths of the other constituent would confirm the validity of the correction method if the random coupling hypothesis is assumed. The final results will be shown to independently validate the manufacturers data and demonstrate the unique potential of MALDI-FTICR-MS for the analysis of this type of polymers.

## 4.2 Experimental

### 4.2.1 Instrumental

The MALDI-FTICR-MS experiments were performed on the heavily modified Bruker-Spectrospin (Fällanden, Switzerland) APEX 7.0e FTICR-MS with the external ion source operating in the MALDI mode. The instrumental layout and experimental procedures are described in detail in Chapter 2 and 3. Briefly, the MALDI samples were deposited on the stainless steel tip of a direct insertion probe and introduced into the external ion source via a vacuum lock. Ions were produced by irradiation of the samples with the 337.1 nm wavelength beam of a nitrogen laser and subsequently transferred by electrostatic ion optics to the analyzer cell. After trapping, the ions were excited to a high, coherent cyclotron orbit and detected at an acquisition rate of typically 500 kHz into 128k data points. This time domain signal was zero-filled to 256k, followed by discrete Fourier transformation and magnitude calculation. The resulting frequency spectrum was transformed to a mass spectrum.

### 4.2.2 Sample Preparation

The copolymeric sample investigated was Pluronic L31, a triblock copolymer of poly-(oxypropylene) and poly(oxyethylene) from BASF (Mount Olive, NJ). According to the specifications of the manufacturer, Pluronic L31 has the general structure HO-$(C_2H_4O)_X$-$(C_3H_6O)_Y$-$(C_2H_4O)_Z$-H. Further, it was specified that the average molecular weight of the PO part was 950 u and that the EO parts constituted 20% of the final molecules. For the MALDI experiments, 2,5-dihydroxybenzoic acid (DHB) from Sigma Chemical Co. (St. Louis, MO) was used as the matrix.

The MALDI samples were prepared by mixing a 1 M matrix solution in ethanol with approximately 10 g/L analyte solution in ethanol in a molar ratio of approximately 1000:1. The resulting analyte matrix solution was electrosprayed on the stainless steel probe tip (Section 3.2.2) over a distance of approximately 7 mm and a voltage difference of typically 4 kV between the capillary and the probe tip. A total of 2 $\mu$g sample was deposited on the probe tip.

## 4.3 Experimental Determination of the Distribution of Units

The distributions in the EO and PO monomers of the Pluronic copolymer were evaluated on the basis of MALDI-FTICR-MS measurements. Figure 4.1 shows an example of a MALDI-FTICR-MS magnitude spectrum of Pluronic L31 in broadband mode. For this spectrum the trapping delay was optimized to be 900 $\mu$s for maximum signal-to-noise at the center of the molecular weight distribution, i.e., it was not compensated for the flight-time induced mass discrimination discussed in section 3.4.1. The spectrum was obtained by summing the spectra of 250 consecutive laser shots. The expansion of the mass scale shows that the resolution is sufficient to resolve the naturally occurring isotopes of a

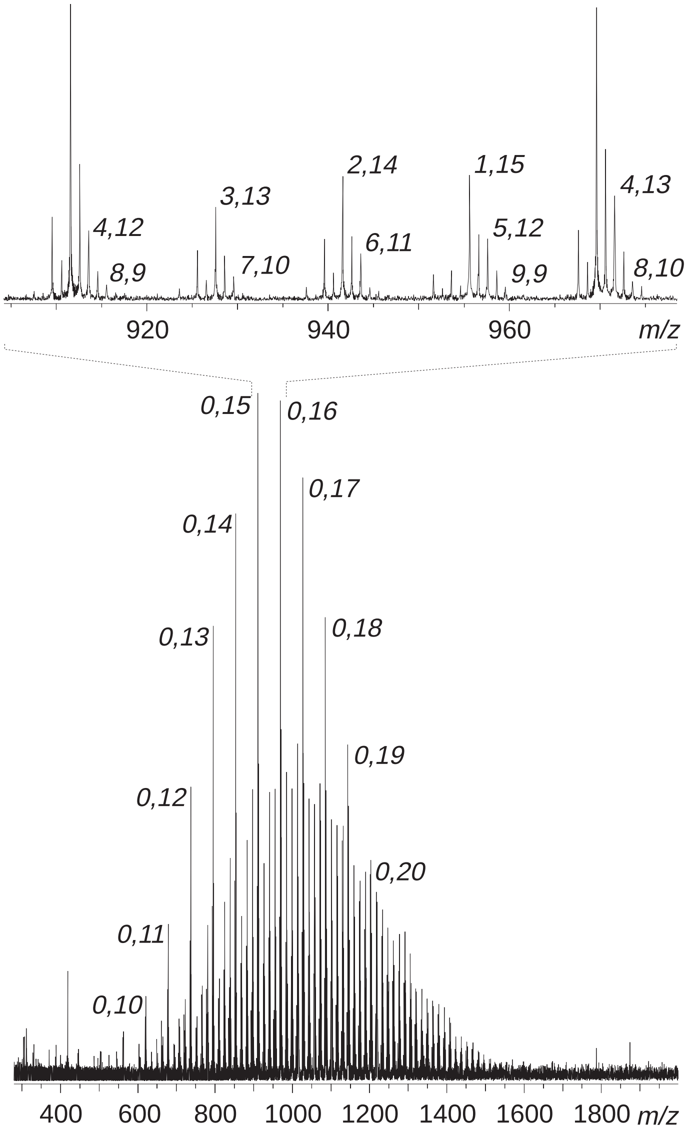

**Figure 4.1:** *MALDI-FTICR-MS spectrum of poly(oxyethylene)-poly(oxypropylene). For this measurement the trapping delay was optimized to be 900 $\mu$s for the center of the molecular weight distribution. The spectra from 250 laser shots were summed. The series of poly(oxypropylene) homopolymers is indicated (the first number refers to $n^{EO}$, the second number to $n^{PO}$). In the expanded mass scale the composition of all monoisotopic copolymers is indicated.*

component molecule. For example, the resolution in broad band mode $(m/\mathrm{d}m)_{50\%}$ is 15,000 with a S/N ratio of 330 at $m/z$ 969.6.

Each copolymer (pseudo-)molecular ion consists of several units of propylene oxide (molecular weight $M_{\text{PO}} = 58.0419$), a few segments of ethylene oxide (molecular weight $M_{\text{EO}} = 44.0262$), the end groups -H and -OH (total molecular weight of the end groups $M_{\text{end}} = 18.0106$), and the cationizing species (molecular weight $M_{\text{cat}}$). Therefore, the molecular weight of the cationized molecular ions can be written as:

$$m/z_{\text{calc}} = n^{\text{PO}} M_{\text{PO}} + n^{\text{EO}} M_{\text{EO}} + M_{\text{end}} + M_{\text{cat}} \tag{4.1}$$

where $n^{\text{PO}}$ and $n^{\text{EO}}$ are the number of segments of PO and EO respectively. From eqn. 4.1 follows that, if the identity of the ionizing species is known, the values for $n^{\text{PO}}$ and $n^{\text{EO}}$ can be obtained by comparison of the measured values for $m/z$ in the spectrum with the calculated masses. The identity of the cation was determined by evaluation of the series of peaks which are relatively abundant in the spectrum, i.e., $m/z$ 1027, $m/z$ 1085, $m/z$ 1143, $m/z$ 1202, etc. The equidistant intervals between these peaks are nominally 58 u (which corresponds to the mass of the PO unit). Linear regression (Section 3.3) on these measured masses versus the estimated degree of polymerization, yields from eqn. 4.1 the mass of the cation plus the mass of the EO segments: $M_{\text{cat}} + n^{\text{EO}} M_{\text{EO}} = 22.990 + i \cdot 58.0419$ u ($i = 0, 1, 2, ...$) (note that the identity of the end groups was known, and that the mass of the end groups has already been subtracted here). For $i = 0$, this series of peaks corresponds to the sodiated poly(oxypropylene) homopolymers (i.e., $n^{\text{EO}} = 0$). For $i > 0$, there are no plausible candidates for the cationizing species and the copolymer composition. In heterodyne mode (similar to Figure 4.4), the presence of cationizing species other than sodium was investigated for the poly(oxypropylene) homopolymers. There was no evidence for other cation adducts; therefore, it is concluded that only signals for sodiated molecules are present in the spectrum. The peaks in the spectrum in Figure 4.1 that correspond to monoisotopic (pseudo-)molecular ions and with S/N>2 were labeled and were used for further analysis. The composition of these copolymer molecules is indicated for the series of poly(oxypropylene) homopolymers in the figure and in the expanded mass scale for all monoisotopic peaks. Here the first number refers to the number of EO units present in the copolymer ($n^{\text{EO}}$), and the second number refers to the number of PO units present ($n^{\text{PO}}$). In this way, 130 monoisotopic peaks were identified, leading to 130 data objects, which are referred to with the following notation (which is in accordance with the notation used in the paper of Wilczek-Vera et al. [80]):

| peak no. | $m/z$ | $n^{\text{EO}}$ | $n^{\text{PO}}$ | relative intensity |
|---|---|---|---|---|
| 1 | $(m/z)_1$ | $n_1^{\text{EO}}$ | $n_1^{\text{PO}}$ | $I_1^{\text{exp}}$ |
| $\vdots$ | $\vdots$ | $\vdots$ | $\vdots$ | $\vdots$ |
| $k$ | $(m/z)_k$ | $n_k^{\text{EO}}$ | $n_k^{\text{PO}}$ | $I_k^{\text{exp}}$ |

(in this data format, $m/z$ increases for increasing $k$). The distribution of both components of the copolymer is visualized by the measured intensities as a function of both $n^{\text{EO}}$ and

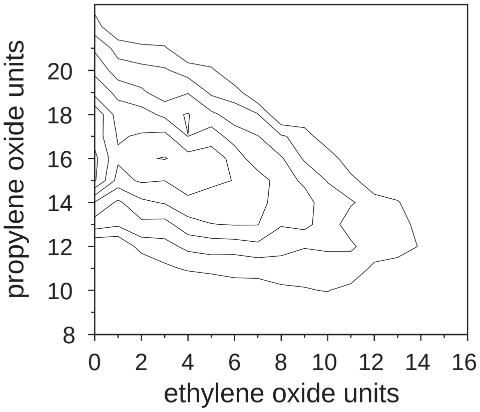

**Figure 4.2:** *Distribution of monomer units as a function of the individual monomer units in the polymer. The data plotted are extracted from the spectrum in figure 4.1.*

$n^{\mathrm{PO}}$ in the contour map in Figure 4.2. This plot indicates that a strong coupling exists between the molecular weight distributions of the individual parts because there is a significant shift of the center of the distribution in the PO part of the copolymer as a function of the number of EO units. However, for this type of block copolymer the polymerization process is expected to follow the random coupling hypothesis (i.e., no correlation between the molecular weights of the individual parts). In fact, the observed asymmetric distribution reflects again the flight-time induced mass discrimination discussed in the previous section. In order to use the superimposition method to correct for this discrimination, a series of 10 experiments were performed, in which the trapping time was varied from 600 $\mu$s up to 1000 $\mu$s, and from 1050 $\mu$s up to 1450 $\mu$s in steps of 100 $\mu$s. At each trapping time setting, multiple laser shots (in the measurements presented typically 250 laser shots) have been averaged to minimize the "shot-to-shot" variations in the MALDI process. All the spectra were recorded from the same spot, which eliminated "spot-to-spot" variations. Finally, a possible decrease in the total ion production in the MALDI process was monitored by taking reference spectra (with the trapping delay at 900 ms) in the course of the series of measurements. No decrease was observed, and therefore it was allowed to apply the superimposition method. The corrected spectrum is shown in Figure 4.3. It can be seen that the molecular weight distribution in Figure 4.3 has become significantly broader in comparison to the spectrum that resulted from the single measurement in Figure 4.1. Especially the lower mass range was affected by the flight-time effect. This explains the shift of the center of the distributions in the PO part toward higher numbers for lower numbers of EO units in Figure 4.2. After all, discrimination of lower masses means a discrimination of the lower end of the distributions in the PO part, which becomes less apparent for larger EO lengths.

Before the spectrum in Figure 4.3 can be processed to reveal the individual block

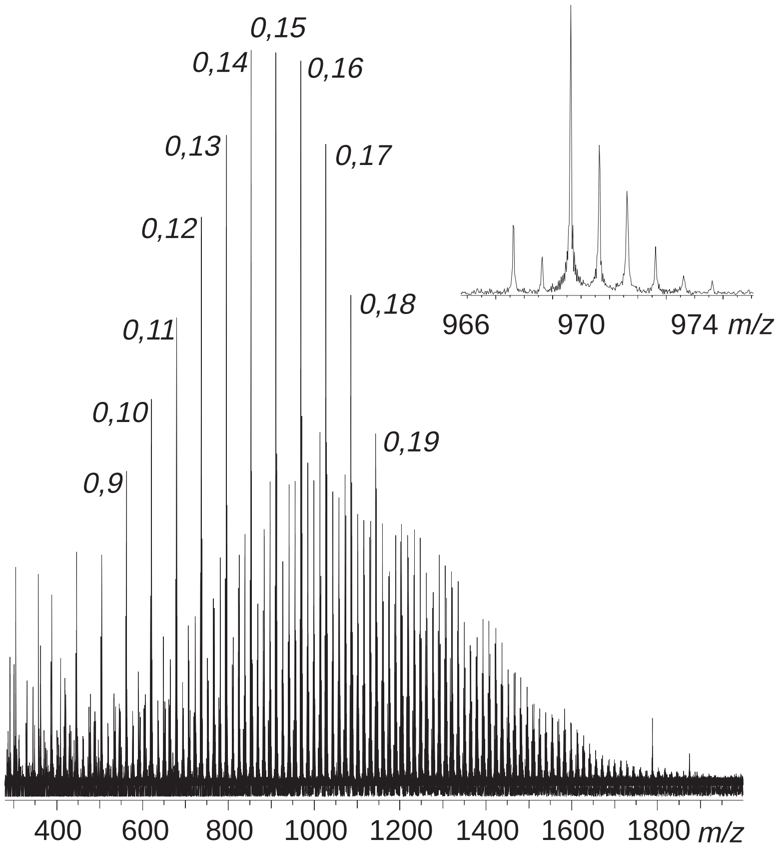

**Figure 4.3:** *Overall MALDI-FTICR-MS spectrum of poly(oxyethlylene)- poly(oxypropylene). The molecular weight distribution was constructed by superimposition of the spectra from a series of experiments performed at different trapping times.*

length distributions, two additional phenomena, which affect the measured molecular weight distribution, have to be taken into account. First, the contribution of the naturally occurring isotopes in the molecular ion changes over the mass range of interest. For example, 62% of the sodium cationized homopolymer with 13 PO units at $m/z$ 796 will be monoisotopic, whereas only 40% of the molecular ions will be monoisotopic for the homopolymer with 25 PO units at $m/z$ 1492. Taking the monoisotopic peaks as the relative abundance of the molecular ions will evidently induce significant errors and, therefore, will distort the molecular weight distribution.

The second effect can be illustrated with the peak at $m/z$ 971.6 in the expanded mass scale in Figure 4.1, where it is seen that no distinction can be made between the second isotopic peak of the homopolymer with $n^{\mathrm{EO}} = 0$ and $n^{\mathrm{PO}} = 16$ (monoisotopic peak at $m/z$

969.6) and the monoisotopic peak of the copolymer with $n^{\mathrm{EO}} = 4$ and $n^{\mathrm{PO}} = 13$ at $m/z$ 971.6. Because all the components of the molecular weight distribution of the Pluronic sample differ by an even number of mass units, and because contributions of isotopic peaks of polymers with a monoisotopic molecular weight less than or equal to $(m/z)_{k-4}$ may be neglected as these can be estimated to be smaller than 1% in the molecular weight range considered here, the intensities of the peaks in the spectrum at $(m/z)_k$ which satisfy

$$(m/z)_k - (m/z)_{k-1} \cong 2 \tag{4.2}$$

have to be corrected for the contribution from the molecular ions with the monoisotopic peak at $(m/z)_{k-1}$. To illustrate the importance of this correction, let us consider the two homopolymers used in the previous example. In the case of the 13-mer, 8% of the molecular ions will contain two $^{13}$C isotopes (or $^{13}$C+$^{17}$O or 2$^{17}$O or $^{18}$O); for the 25-mer this will be 17%. On the basis of the intensities in the mass spectrum in Figure 4.3, it was determined that the contribution of the 2$^{13}$C isotope of the 13-mer to the peak that corresponds to the monoisotopic $(n^{\mathrm{EO}}, n^{\mathrm{PO}}) = (4, 10)$ was ~50%; for the 2$^{13}$C isotope of the 25-mer and for the $(n^{\mathrm{EO}}, n^{\mathrm{PO}}) = (4, 22)$, this was determined to be 10%. This second effect is further illustrated by utilization of the high mass resolution of the instrument in the heterodyne mode. The mass range $m/z$ 930 - 1015 was recorded in this high-resolution mode and resulted in the spectrum shown in Figure 4.4. The inset reveals that the resolution $(m/\mathrm{d}m)_{50\%} = 135,000$ (at $m/z$ 669.7) is sufficient to separate the two peaks around $m/z$ 971.7.

In principle, the heterodyne mode would be a potential way to overcome the problem of peak overlap. However, it would take approximately 20 experiments for each different trapping delay (i.e., a total of 200 experiments) to cover the entire molecular weight distribution. Such large numbers of experiments can practically not be correlated due to inevitable variations in ion yields. Therefore, it is proposed to apply a correction method instead. This method is checked by comparison of the data from the high resolution spectrum in Figure 4.4 with those from the broad band spectrum in Figure 4.3. It is determined from the peaks at $m/z$ 969 and at $m/z$ 971.65 in the high-resolution spectrum that the ratio between the abundance of the monoisotopic $(n^{\mathrm{EO}}, n^{\mathrm{PO}}) = (4, 13)$ copolymer and the abundance of the monoisotopic $(n^{\mathrm{EO}}, n^{\mathrm{PO}}) = (0, 16)$ copolymer would be 0.19. Determination of this ratio from the spectrum in Figure 4.3 yields the value 0.36. After correction of the intensities for the expected overlap (according to the method which is proposed below) this value became 0.18, which is in excellent agreement with the result from the high-resolution measurement, and thus confirms the validity of the correction method. This example also illustrates that the precision of the correction process for the individual intensities is of the order of 5% (off course, for very low S/N ratios, this value might increase significantly).

Corrections for the change of the isotopic patterns over the mass range and the overlap of peaks can easily be calculated with analytical expressions. The first step in the derivation of these expressions is the calculation of the probability that the poly(oxyethylene)-poly(oxypropylene) molecule is monoisotopic. Standard probability theory [120] yields

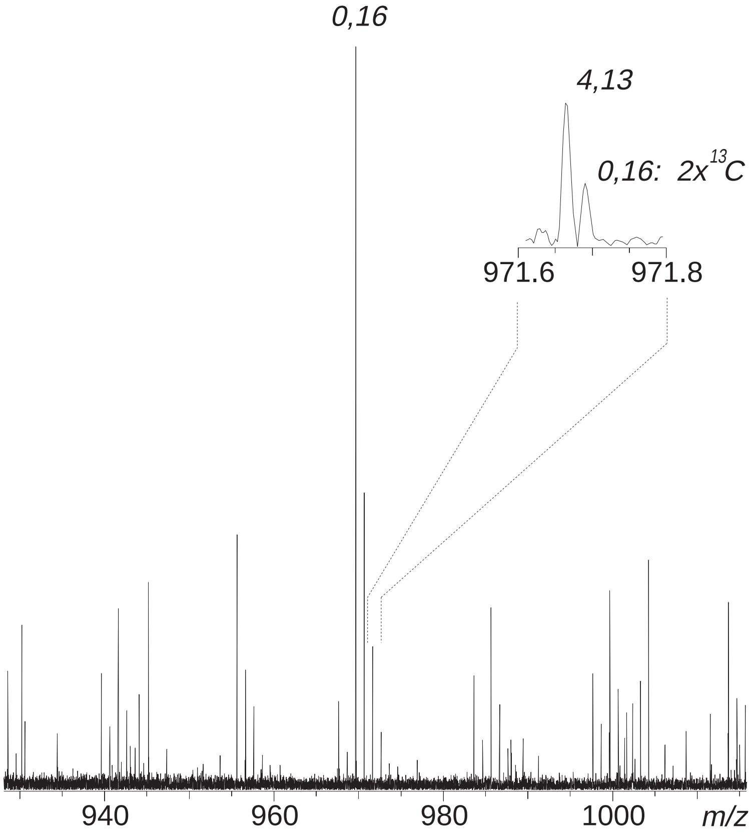

**Figure 4.4:** *High resolution (heterodyne) MALDI-FTICR-MS spectrum of poly(oxyethlylene)- poly(oxypropylene) around* $m/z$ *970. The expansion of the mass scale shows that the second isotopic peak of the* $(n^{EO}, n^{PO}) = (0, 16)$ *copolymer and the monoisotopic peak of the* $(n^{EO}, n^{PO}) = (4, 13)$ *copolymer are separated, which can not be accomplished in broad band experiments.*

for the probability that a copolymer which consists of $n_k^{\mathrm{EO}}$ EO units and $n_k^{\mathrm{PO}}$ PO units (i.e., [HO-($C_2H_4O$)$_{n_k^{\mathrm{EO}}}$-($C_3H_6O$)$_{n_k^{\mathrm{PO}}}$-H]) has a mass of $(m/z)_k$ (i.e., it is monoisotopic):

$$P(n_k^{\mathrm{EO}}, n_k^{\mathrm{PO}}, (m/z)_k) = A^{2n_k^{\mathrm{EO}}+3n_k^{\mathrm{PO}}}(^{12}\mathrm{C}) \cdot A^{n_k^{\mathrm{EO}}+n_k^{\mathrm{PO}}+1}(^{16}\mathrm{O}) \tag{4.3}$$

where $A^b(^m\mathrm{X})$ denotes the $b$th power of the natural abundance of the isotope $^m\mathrm{X}$. If there is no polymer present in the spectrum with a monoisotopic molecular weight $(m/z)_{k-2}$, then the corrected abundance for this component of the molecular weight distribution is simply given by:

$$I_k^{\text{corr}} = \frac{I_k^{\text{exp}}}{P(n_k^{\text{EO}}, n_k^{\text{PO}}, (m/z)_k)} \tag{4.4}$$

where $I_k^{\text{exp}}$ refers to the measured intensity of the peak at $(m/z)_k$. If there is a peak at $(m/z)_{k-2}$, the probability has to be calculated that also the mass of the copolymer described by $n_{k-1}^{\text{EO}}$ and $n_{k-1}^{\text{PO}}$ equals $(m/z)_k$. This probability is equal to the sum of the individual probabilities that this molecule contains two $^{13}$C isotopes, one $^{13}$C and one $^{17}$O isotope, or one $^{18}$O isotope (the chance that two $^{17}$O isotopes are present is negligible). The calculation of this probability is analogous to the one in eqn. 4.3.

With these probabilities, the corrected abundance becomes

$$I_k^{\text{corr}} = \frac{1}{P(n_k^{\text{EO}}, n_k^{\text{PO}}, (m/z)_k)} \left( I_k^{\text{exp}} - \frac{P(n_{k-1}^{\text{EO}}, n_{k-1}^{\text{PO}}, (m/z)_k)}{P(n_{k-1}^{\text{EO}}, n_{k-1}^{\text{PO}}, (m/z)_{k-1})} I_{k-1}^{\text{exp}} \right) \tag{4.5}$$

A small computer program was developed to aid in the interpretation of the copolymer spectra and the processing of the large data sets. This program uses the elemental composition of the two different monomeric units and the end groups of the copolymer as input in order to determine the composition of the copolymer for each peak in the spectrum with eqn. 4.1. Subsequently, it calculates the corrected intensities for all the components of the molecular weight distribution with eqns. 4.4 and 4.5. Finally, it calculates the characterizing numbers presented below.

The effect of the corrections can be quantified by calculation of the number- and the weight-average molecular weights ($M_n$ and $M_w$, respectively), and the polydispersity factor ($M_w/M_n$) for the copolymers with $n^{\text{EO}} = 4$ for the uncorrected data, for the data corrected only for the isotope effect, and for the fully corrected data. The resulting values are listed in Table 4.1. It should be mentioned here that all peak intensities were determined by integration over the peaks, because otherwise the correction for the peak overlap would not hold. For example, if the overlapping peaks do not entirely coincide, then peak broadening will occur, and the use of peak heights will underestimate the actual intensities. It can be seen from the table that, for the sample under investigation, the change induced by each correction is about the same. The total percentile change in

**Table 4.1:** *$M_n$, $M_w$, and $M_w/M_n$ determined from the individual molecular weight distribution of the copolymers with 4 ethylene oxide units.*

| | $M_n$ | $M_w$ | $M_w/M_n$ |
|---|---|---|---|
| uncorrected | 1047 | 1104 | 1.055 |
| corrected for isotope effect | 1083 | 1136 | 1.049 |
| fully corrected | 1125 | 1177 | 1.047 |

the values listed in the table is 6-8%. Off course, these differences in molecular weight do not lead to measurable differences in physical properties. However, the corrections appear to be valuable in the evaluation of the second step of the synthesis of the block polymer (where the propylene block is sandwiched between ethylene blocks). In order to fully characterize the sample under investigation, we calculated the usual molecular weight averages (number average), (weight average), and the polydispersity factor from the complete molecular weight distribution. In addition, some averages which describe the chemical composition of the block copolymer in terms of the individual segments are introduced:

1. the average number of units for segment X (X=EO,PO) in the block copolymer:

$$\overline{n}_n^X = \frac{\sum_k n_k^X I_k^X}{\sum_k I_k^X} \tag{4.6}$$

2. the weight average number of units for segment X:

$$\overline{n}_n^X = \frac{\sum_k (n_k^X)^2 I_k^X}{\sum_k n_k^X I_k^X} \tag{4.7}$$

3. the polydispersity factor for segment X:

$$\frac{n_w^X}{n_n^X} \tag{4.8}$$

4. the chemical composition of segment X:

$$\overline{x}^X = \frac{M_X \overline{n}_n^X}{M_n} \tag{4.9}$$

The values of these quantities were calculated from the data extracted from the spectrum in Figure 4.3 before as well as after correction and are listed in Table 4.2. The characterizing numbers according to the manufacturer are $\overline{n}_n^{\text{PO}} = 16 (\approx 950/58.04$; error margin $\approx 0.5$) and $\overline{x}^{\text{EO}} = 0.2$ (error margin $\approx 0.03$). When these numbers are compared with the values presented in Table 4.2 ($\overline{n}_n^{\text{PO}} = 15.57$ and $\overline{x}^{\text{EO}} = 0.17$ after correction), it can be seen that our results derived from MALDI-FTICR-MS confirm the manufacturers specifications with greater accuracy.

The individual block length distributions are visualized in contour maps. Figure 4.5A shows the data after flight-time compensation and Figure 4.5B shows the fully corrected data. Comparison of the two contour maps shows that the full correction removes the discontinuity in the EO distribution around $n^{\text{EO}} = 4$ (a local maximum). This discontinuity arose from the peak overlap of the second isotopic peaks with $n^{\text{EO}} = 0$ (i.e., the poly(oxypropylene) homopolymers) and the monoisotopic peaks with $n^{\text{EO}} = 4$. The contour map in Figure 4.5B clearly reveals the random coupling hypothesis for this type of

**Table 4.2:** *Properties of the Pluronic L31 sample calculated from the spectrum in Figure 4.3.*

| | uncorrected | | corrected | |
|---|---|---|---|---|
| | EO block | PO block | EO block | PO block |
| $\overline{n}_n^X$ | 4.53 | 14.78 | 4.11 | 15.57 |
| $\overline{n}_w^X$ | 8.51 | 15.83 | 8.14 | 16.55 |
| $n_w^X/n_n^X$ | 1.88 | 1.07 | 1.98 | 1.06 |
| $\overline{x}^X$ | 0.19 | 0.81 | 0.17 | 0.83 |
| $M_n$ | 1098.4 | | 1125.7 | |
| $M_w$ | 1175.9 | | 1200.6 | |
| $M_w/M_n$ | 1.07 | | 1.07 | |

copolymers, as the distribution in the PO units remains the same for different EO segments. Moreover, the fact that the experiment verifies the random coupling hypothesis indicates that the correction of MALDI-FTICR-MS spectra with the methods described above leads to the real molecular weight distribution. This means also that other possible mass discrimination effects in MALDI-FTICR-MS with an external ion source (for example, discriminations in the MALDI processes, mass-dependent transfer efficiencies, mass-dependent trapping, and discriminations in the excitation and detection event) are negligible over the mass range considered here. The random coupling hypothesis can be verified more accurately by calculation of the experimental marginal probabilities for the

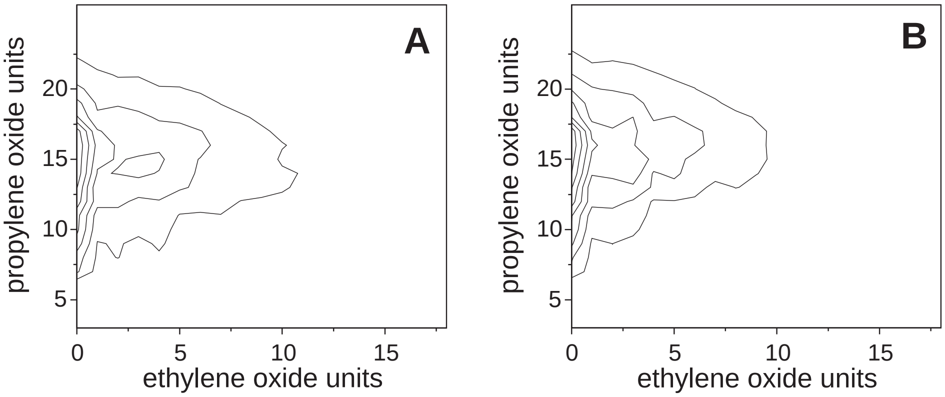

**Figure 4.5:** *Contour maps of the overall distribution of monomer units as a function of the individual monomer units in the polymer, both before (A) and after correction (B) for the isotope effect and peak overlap. The data plotted are determined from the reconstructed molecular weight distribution in Figure 4.3.*

two components of the copolymer [80, 120]. For the PO units the marginal probability $\Gamma^{\mathrm{PO}}_{\exp}$ is defined by:

$$\Gamma^{\mathrm{PO}}_{\exp}(n_j^{\mathrm{PO}}) = \sum_i \Gamma^{\mathrm{PO}}_{\exp}(n_i^{\mathrm{EO}}, n_j^{\mathrm{PO}}) \tag{4.10}$$

where $\Gamma^{\mathrm{PO}}_{\exp}(n_i^{\mathrm{EO}}, n_j^{\mathrm{PO}})$ is the experimental distribution function, which is equal to the measured intensity for given $n_i^{\mathrm{EO}}$ and $n_j^{\mathrm{PO}}$. According to this formula, all the measured intensities for a given $n_j^{\mathrm{PO}}$ are summed. Similarly, the marginal probability $\Gamma^{\mathrm{EO}}_{\exp}$ for the EO units is defined. If the random coupling hypothesis holds, then the experimental distribution function can be represented as the product of the two marginal distributions [120]:

$$\Gamma^{\mathrm{PO}}_{\exp}(n_i^{\mathrm{EO}}, n_j^{\mathrm{PO}}) = \Gamma^{\mathrm{PO}}_{\exp}(n_i^{\mathrm{EO}})\Gamma^{\mathrm{PO}}_{\exp}(n_j^{\mathrm{PO}}) \tag{4.11}$$

In order to test eqn. 4.11, it was assumed that the distributions in the PO units for each number of EO units would follow the Gaussian function. If the heights of the (fitted) Gaussian functions are considered to be representative for the distribution in the EO units, it is possible to rewrite eqn. 4.11 as:

$$\Gamma^{\mathrm{PO}}_{\exp}(n_i^{\mathrm{EO}}, n_j^{\mathrm{PO}}) = A(n_i^{\mathrm{EO}}) \exp - \left( \frac{(n_j^{\mathrm{PO}} - n_c^{\mathrm{PO}})^2}{w} \right) \tag{4.12}$$

If eqn. 4.12 holds, it follows that the fitted PO distributions have equal centers $n_c^{\mathrm{PO}}$ and equal widths $w$. This is evaluated in Figure 4.6, were the results of the individual fits are

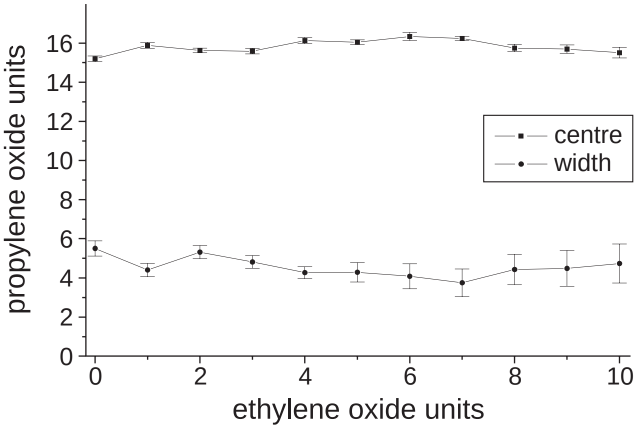

**Figure 4.6:** *Test of the random coupling hypothesis for the Pluronic L31 copolymer. The measured distribution in the propylene oxide units is fitted with a Gaussian function for different numbers of ethylene oxide units. The center and width of the fitted Gaussian functions are plotted as a function of the number of ethylene oxide units.*

plotted as a function of $n^{\mathrm{EO}}$. It is seen that values for $w$ and $n_c^{\mathrm{PO}}$ are randomly distributed around the average value of 4.26 and 13.67, respectively. The observed fluctuations are most probably caused by differences in S/N ratios. At lower S/N ratios ($<3$), the accuracy in the determination of the peak intensities becomes of the order of the corrections for peak overlap; consequently these corrections will induce additional errors to the sides of the overall 2D distribution. As there are no significant trends visible in Figure 4.6, it is concluded that the random coupling hypothesis is valid for this particular Pluronic copolymer system.

## 4.4 Summary and Conclusions

The molecular weight distribution of a triblock polymer of poly(oxypropylene) and poly-(oxyethylene) was measured with MALDI-FTICR-MS. The superimposition method that was proposed in Chapter 3 was applied to compensate for flight-time induced mass discriminations during the ion transport from the ion source to the ICR-cell. An additional correction algorithm was developed to process the data from the MS peaks in order to correct for the change in the isotopic patterns over the measured molecular weight distribution and for the overlap of different isotopic peaks. The magnitude of these corrections on the molecular weight data for the copolymer sample under study is as large as 10%. The results demonstrate that the experimental technique is very useful for characterization of the individual block length distributions, even in those cases where the difference in mass of the different components of the molecular weight distribution is very small (down to several milli-mass units).

The random coupling hypothesis was tested and was found to hold for the copolymer system studied. This result is also a further experimental verification of the superimposition method and proves that the actual molecular weight distribution of synthetic polymers can be obtained with MALDI performed in the external ion source of an FTICR-MS.

# 5

# Design and Performance of an Arbitrary Waveform Generator for Ion Excitation in Trapped Ion Mass Spectrometry

*The design of a novel arbitrary waveform generator, which has been developed for the excitation of ion motions in ion traps, is presented. The system is equipped with a 192 Mb solid state memory for the storage of excitation waveforms. A local processor ensures its real-time operation and controls the waveform generation. Its platform-independent design provides an easy interfacing to virtually any experimental environment. The system performance is demonstrated with the isotope depletion of a complex polyoxyalkeneamine distribution (produced by matrix assisted laser desorption/ionization) and the isolation of a single isotope from the charge-state distribution of cytochrome c (produced by electrospray ionization) in FTICR-MS measurements.*

## 5.1 Introduction

The theoretical considerations in Chapter 2 demonstrate that the intrinsic versatility of ion traps derives from the ability to manipulate the ions with radio frequency (rf) fields. For example, frequency-selective excitation makes it possible to detect, eject or kinetically excite ions of selected $m/z$ ratios. Marshall and co-workers developed the concept of Stored Waveform Inverse Fourier Transform (SWIFT) excitation, inspired by “tailored” broadband selective excitation in Nuclear Magnetic Resonance (NMR) spectroscopy [121] to address this need of frequency-selectivity. Their method no longer constructs the waveforms in the time domain. Instead, the desired post-excitation cyclotron radius spectrum is arbitrarily specified in the frequency domain. The corresponding time domain excitation waveform is subsequently calculated by inverse Fourier transformation of that spectrum. The immediate problem in this approach is imposed by the potentially wide frequency range involved in FTICR-MS broad band excitations, because the initial time domain excitation power is determined by the integrated magnitude spectrum. In an FTICR-MS instrument equipped with a 7 T magnet for example, the cyclotron frequencies of ions in the mass range $10^1 < m/z < 10^4$ cover the frequency range from $10^4 ... 10^7$ Hz . Excitation of ions to a cyclotron radius of 1 cm over this frequency range would require rf excitation powers of $10^4 - 10^5$ V. In practice, generation of such a waveform would be equivalent to impulse excitation, and spectral resolution would be lost. Modern SWIFT algorithms deal with this amplitude problem by specification of a quadratic continuous phase spectrum next to the arbitrary magnitude spectrum, which effectively spreads the excitation power over the duration of the waveform [60, 122–125].

Naturally, it is not possible to generate SWIFT excitation signals with (programmable) frequency generators. Since the first SWIFT experiments, which were carried out using home-built electronics [121], PC-based systems [126] and, more recently, commercially available arbitrary waveform generators (AWG) [127, 128] have been used to convert the digital data to analog excitation signals. These systems typically consist of a static memory bank of 16 kword to 1 Mword and a digital-to-analog converter (DAC) with a precision of typically 8 to 12 bit. The sample rates vary from 1 to 20 MHz, which corresponds according to the Nyquist criterion to maximum output frequencies of 0.5 to 10 MHz. Although such system properties already allow for a wide range of experiments, the flexibility in designing experimental event sequences is still rather constrained. Given that a single SWIFT waveform can easily occupy up to a few Mword of memory, it is generally not possible to use several SWIFT waveforms in a single sequence without transferring new data to the waveform memory. The latter brings about a dead time of typically several seconds in between subsequent waveforms.

To overcome these limitations, we have developed a novel AWG system dedicated to ion excitation in ion traps. Its user interface is hosted by a UNIX-based workstation, which is also used to calculate the digital waveforms. This configuration possesses unique features based on its unprecedented solid state memory size of 192 Mb, its real-time properties and its stand-alone operation. For example, the size and number of waveforms used in a sequence is practically unlimited because virtually all required waveforms can be stored in the system's memory prior to the start of an experiment. Thus, no limitations are imposed by the rate and the volume of the data transfer to the system. In addition, the AWG system can be connected to any experimental apparatus, because the interface merely consists of a trigger and an analog signal line. The required output sequences are produced by programming the sequencing software that runs on the local AWG processor.

In this chapter, the details of the in-house designed electronics and the functionality of the in-house developed software are described. The performance of the novel AWG system is demonstrated with FTICR-MS measurements. The results of isolating a number of components of a synthetic polymer molecular weight distribution by simultaneous ejection of all other components and isolating a multiply charged protein isotope illustrate the versatility and frequency selectivity of the system.

## 5.2 Design

### 5.2.1 General Design

Figure 5.1 shows the block diagram of the electronics that are of importance for the AWG-based FTICR-MS experiments. The dashed lines indicate the physical separation of the newly constructed AWG system, its host computer, and the FTICR-MS instrument with its relevant components, which run as "stand-alone" systems. Details on the in-house developed hardware and software will be presented below. Here, the basic operating principles are described briefly.

The arbitrary excitation waveforms are calculated on the host computer and are subsequently transferred to the memory of the AWG system. Also AWG event sequences are constructed on the host computer using waveforms stored in the AWG system. Delays, triggers, and loops can be added to these waveforms. After loading the event sequence into the local processor, experiments can be started. During experiments, the AWG system is exclusively waiting for external triggers from the FTICR-MS control electronics to generate analog signals from the digital data. The order of the waveforms, delays, and triggers are controlled by the local processor. If necessary, it also switches hardware settings (e.g., the bandwidth and the attenuation level) in between subsequent waveforms. The output of the AWG system is connected to the FTICR-MS instrument, where it is amplified and split into two 180° out-of-phase channels to drive the excitation plates of the ICR analyzer cell.

### 5.2.2 Description of the AWG hardware

The backbone of the AWG system is the VME instrumentation bus. The local processor (25 MHz VME processor board 68040, Motorola) is its bus master and is booted automatically via the Ethernet using the host computer (Indigo Irix 5.3 UNIX-based workstation, Silicon Graphics, Mountain View, CA) as boot site. It configures the various system components prior to the generation of a waveform. The waveforms are loaded from the host computer via the BIT3 Bus Bridge connection to the VME bus into the memory boards of the AWG system ($3 \times 64$ Mbyte, Chrislin Industries Inc., Westlake Village, CA). The waveforms have to be encoded in a special format, in which every three 32 bit words contain 8 samples of 12 bits each (corresponding to the resolution of the DAC). According to this format, the three nibbles (4 bit entities of data) composing each of the eight samples are divided over the three 32 bit words. In turn, each set of three 32 bit words is divided over the three memory boards and stored at the same memory location. This data format is introduced to obtain a sustained sample rate of maximally 20 MHz next to a maximum cycle rate of 10 MHz at the VME Subsystem Bus (VSB bus), as will be shown later. An additional advantage is the optimal usage of the available memory (the packed format allows for 128 Mword sample storage in the AWG system).

Sample processing hardware was designed in-house to read the data describing the waveforms from the memory modules and to convert them into a continuous stream of

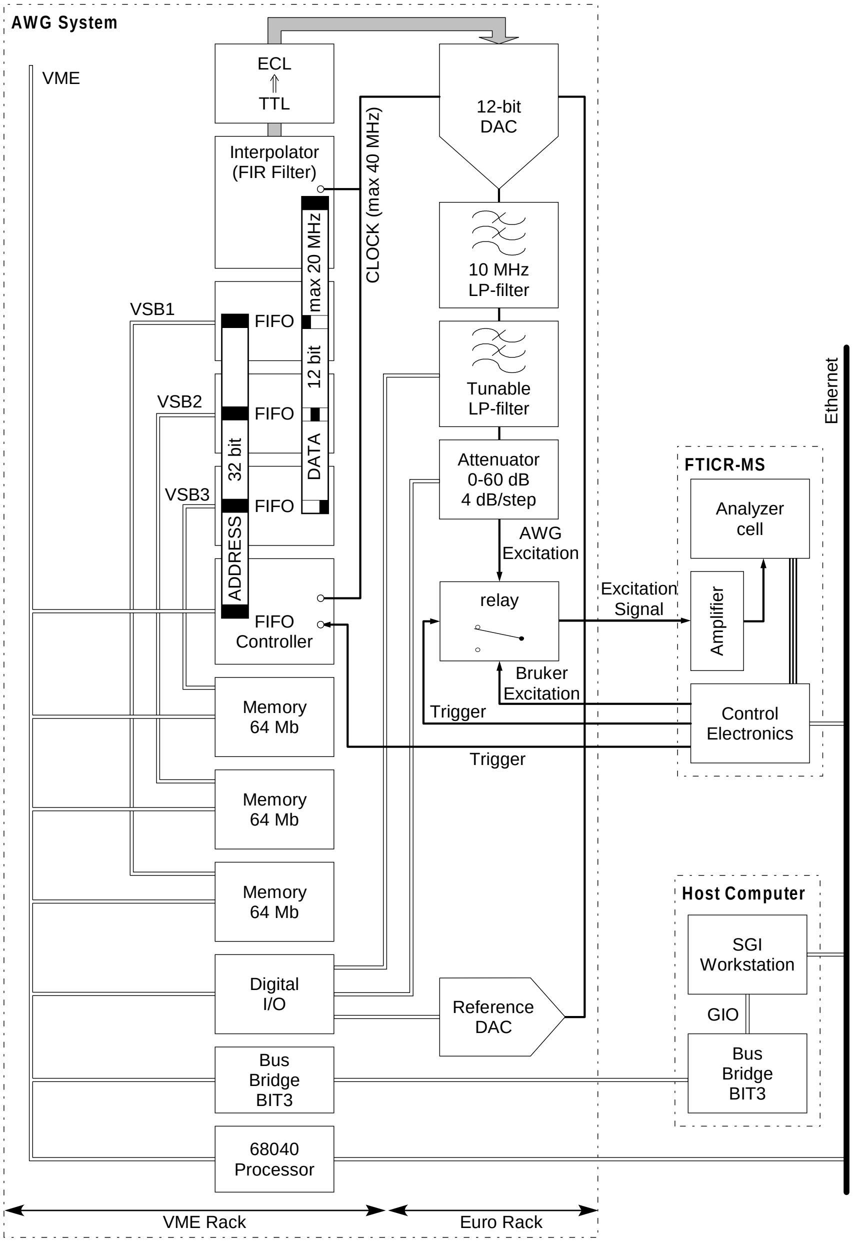

Figure 5.1: Block diagram of the electronics for AWG-based FTICR-MS experiments.

decoded 12 bit samples. The sample processing hardware consists of three FIFO (First In First Out memory) boards, which are based on a 2 kbyte FIFO buffer, and a FIFO controller board. Communication between these boards is realized via an additional control bus. The FIFO boards are connected to the memory boards via independent VSB side busses. This allows reading of the data in blocks of 128 words (that is, 512 bytes) from all memory boards simultaneously, at the maximum VSB cycle rate of 10 MHz. The start and finish address of a waveform as well as its bandwidth are loaded from the local processor into the FIFO controller board prior to the generation of a waveform. The control board starts the FIFO boards on the rising edge of an external trigger signal to extract in parallel nibbles from the FIFO buffers at a continuous rate of twice the waveform's bandwidth. This rate is governed by the 40 MHz internal clock of the FIFO controller board and can be adjusted by dividing the 40 MHz by powers of two in the range from 156 kHz to 20 MHz. The FIFO boards present the extracted nibbles in parallel to the data bus, jointly composing the original decoded 12 bit samples. During this process, a new VSB data transfer is initiated by the FIFO controller to replenish the FIFO buffers when 512 bytes have been freed. This continues until the entire waveform has been processed.

The stream of samples produced by the sample processing hardware (at the rate of twice the bandwidth) is interpolated once by a digital FIR (Finite Impulse Response) filter, producing a stream of samples at the rate of four times the bandwidth. Conversion to an analog signal is realized by a 12 bit DAC (Burr Brown). The FIR filter and the DAC are operated at a clock signal of four times the bandwidth, which is received from the internal clock of the FIFO controller board. Frequency components outside the bandwidth are removed from the excitation signal by the combination of a tunable and a 10 MHz low-pass filter. The dynamic range of the excitation signal can be modified by adjusting the attenuator (0-60 dB in steps of 4 dB). Additional fine-tuning of the dynamic range is available by adjusting the reference voltage of the DAC via an additional reference DAC, which sets the maximum output voltage of the 12 bit DAC. The settings of the tunable filter, the attenuator, and the reference DAC are initialized by the local processor via the in-house designed digital input-output module. Finally, the output of the AWG system is connected to the transmitter of the FTICR-MS instrument via a relay switching circuit, which allows for fast switching (dead time of the circuit is approximately $100 \mu s$) between AWG excitation signals and other excitation signals (e.g., the standard Bruker programmable frequency synthesizer) during experiments. This relay is operated on trigger pulses from the FTICR-MS control electronics such that the AWG output is connected to the transmitter if the trigger input is high.

After completion of the waveform, the local processor initiates the next task. This can be a next waveform following a variable time delay or a new trigger from the FTICR-MS control electronics. Alternatively, if the AWG event sequence is completed, it can be restarted automatically. The latter facilitates for example signal averaging over multiple experiments. Usually, various hardware parameters have to be reset in between subsequent waveforms, causing a dead time of approximately 1 ms.

### *5.2.3 Description of the Software*

Software was developed in-house for the calculation of waveforms, the construction of AWG event sequences, the communication between the host computer and the AWG system, and the task managing within the AWG system. This software consists of two elements: TasMan that runs under the real time operating system LynxOS on the local processor, and XAWG that runs under UNIX on the host computer.

The TasMan program controls the operation of the AWG electronics. For this purpose, it maintains a database of the waveforms that are stored in the systems memory and the associated hardware settings. It communicates with the host computer via the Ethernet in a server-client relationship. This communication line is used to receive a second database, which describes the composition of the AWG event sequence, and the commands to start and finish executing this sequence. During the sequence, the TasMan program configures the various hardware parameters when appropriate. In this way, it allows for real-time switching between subsequent pulses within 100 $\mu s$.

The XAWG program assists in the design and calculation of (SWIFT) waveforms, the design of AWG event sequences, and the communication with the AWG system. It is compatible with the data format used by the Bruker software XMASS. Loading a measured FTICR-MS transient signal into XAWG automatically sets defaults for various variables in the calculations. For example, the bandwidth for the excitation, the size of the data set, and the calibration constants for the transformations between the frequency and the mass domain are copied from the experimental parameters. After Fourier transformation of the transient, an excitation profile is constructed on the basis of the mass spectrum in the graphical user interface with standard functions. These include rectangular magnitude versus mass segments (determined by a center mass, a mass width and an excitation radius), and sinusoids in the mass domain (useful in two-dimensional FTICR-MS experiments [129]). The excitation profiles are saved in terms of the building objects, which allows for readily adjusting them at all times. Smoothing of the excitation profile by convolution of the spectrum with a rectangular pulse in the frequency domain [60, 124] is available to minimize wiggles (so-called Gibb's oscillations) in the actual magnitude spectrum of the calculated waveform. Subsequently, the desired post-excitation cyclotron radius as a function of mass is converted to excitation voltage magnitude versus frequency. This spectrum is used to calculate the quadratic phase versus frequency function for an optimal spread of the excitation power in the SWIFT waveform with an algorithm that is based on the methodology developed by Guan and McIver [124]. Inverse Fourier transformation of the magnitude and phase spectra yields the SWIFT excitation waveform. Finally, the ”true” excitation spectrum is examined by zero-filling and Fourier transformation of the SWIFT waveform.

In addition to the SWIFT waveforms, it is also possible to create the traditional time-domain excitation waveforms. For narrow band excitation, the single-frequency (burst) excitation (a sinusoid with fixed frequency and amplitude) is available. Broad band excitation can be performed using the chirp excitation (a constant-amplitude sinusoid whose instantaneous frequency increases linearly with time over a given frequency range).

The amplitude uniformity of the excitation spectrum produced is, particularly in the case of SWIFT waveforms, directly dependent on the accuracy of the digital-to-analog conversion [130]. It is therefore advantageous if the maximum amplitude of the waveform corresponds with the dynamic range of the DAC. In general, this is automatically achieved in the calculation of the optimal phase function according to the SWIFT algorithm of Guan and McIver [124]. However, if the duration of the excitation waveform is determined by the required resolution rather than the required total excitation power, a substantial mismatch may occur. Therefore, all excitation waveforms are normalized to fit the -2048 ... 2047 range corresponding to the 12 bit resolution of the DAC. The desired excitation power is obtained by adjusting the attenuator and the reference voltage of the DAC to the values that are calculated from the normalizing constant.

The normalized waveforms are written to disk in the special data format compatible with the AWG hardware. The associated hardware settings are attached in a header. A loader is implemented in the XAWG program to load these waveforms to the memory of the AWG system and the hardware settings to the TasMan program. The final part of the XAWG program, the sequencer, acts as the user interface to the AWG system. It retrieves the database describing the waveforms available in the AWG memory from the TasMan program and allows the user to design the AWG event sequence.

The system's flexibility in constructing the most versatile experiments is illustrated on the basis of the exemplar AWG sequence that is depicted in Figure 5.2. Also an external FTICR-MS trigger signal and the generated AWG output are included in the figure. Its practical relevance is that it contains all excitation events that are required for FTICR-MS experiments in which collision-activated dissociation (CAD) [131–133] of ions is achieved by application of sustained off-resonance irradiation (SORI) [134]. Briefly, it comprises the isolation of the precursor ions, the alternating acceleration and deceleration of these ions between a starting radius and a larger radius by an off-resonance burst excitation (typically, $\Delta f$ is varied from $10^2$ to $10^4$ Hz), and finally, the broad band excitation to produce a detectable signal for all precursor and fragment ions.

The sequence shows that subsequent waveforms can be separated by either external triggers or internal delays. It is also seen that the trigger signals remain high for the entire part of the sequence that they initiate. This is required because otherwise the AWG system will abort the sequence to prevent that other tasks managed by the FTICR-MS instrument (e.g., the detection event) unintentionally coincide with the AWG excitation events.

Additionally, the sequence exhibits that any part of it can be repeated several times. The main loop in the example is generally used to perform experiments in which the results of several measurements are averaged. The second loop is used to produce a single-frequency excitation signal from a waveform consisting of one period of a sinus. This is only possible by virtue of the systems capability of real-time and instantaneous pulse switching. It is obvious that this saves considerable amounts of memory compared to storing the complete waveform. It should be noted however that this is only possible if an integer number of periods of the sinus can be fitted into the block size of the data transfer between the memory modules and the FIFO buffers (that is, $128 \times 8$ samples).

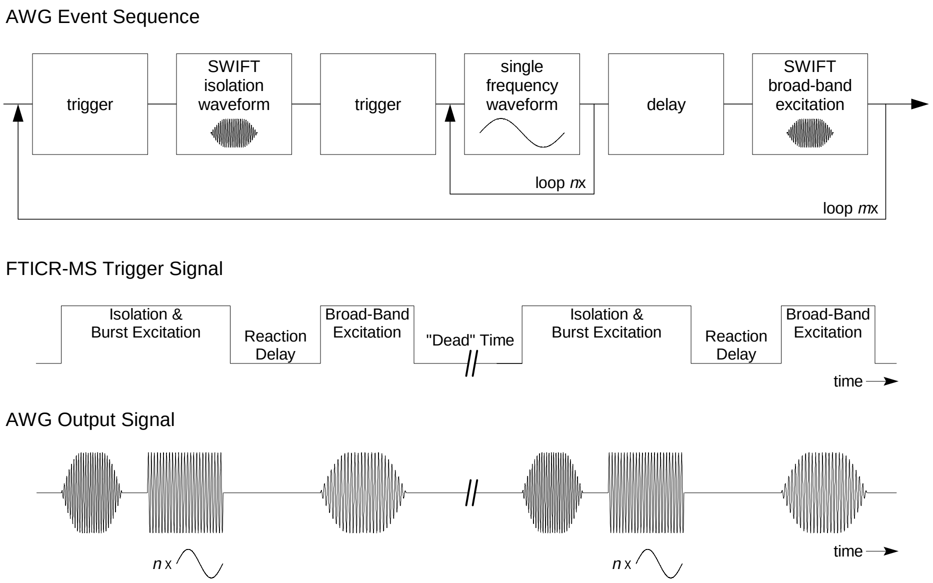

**Figure 5.2:** *Example of an AWG event sequence that illustrates the flexibility provided by the AWG system for the construction of experiments. Also shown is the AWG output that is generated by this sequence if the depicted external FTICR-MS trigger signal is applied to the system.*

This condition can be written as:

$$128 \times 8f_{\mathrm{exc}} = nf_{\mathrm{sample}} \tag{5.1}$$

Here, $n = 1, 2, 3, ...$, $f_{\mathrm{exc}}$ is the excitation frequency, and $f_{\mathrm{sample}}$ is the sample rate. If this condition is not met, a discontinuity will appear every time that the block of data is repeated.

## 5.3 Experimental

### *5.3.1 Instrumental*

The FTICR-MS experiments were performed on the modified Bruker-Spectrospin (Fällanden, Switzerland) APEX 7.0e FTICR-MS. The instrumental layout and experimental procedures are described in detail in Chapter 2. Briefly, the MALDI experiments were carried out in the MALDI/EI source by depositing the samples on the stainless steel tip of a direct insertion probe and introducing this tip into the external ion source via a vacuum lock. Ions were produced by irradiating the samples with the 337.1 nm wavelength beam of a nitrogen laser and they were subsequently transferred into the analyzer cell by electrostatic ion optics. The ESI experiments were performed in a newly in-house constructed source, which is described elsewere [135]. In the ESI geometry, a syringe pump was used to deliver the samples via a deactivated fused silica capillary to a stainless steel spray needle at a flow rate of 0.1 mL/hr. Positively charged electrosprayed droplets that were generated by applying $\sim 3000$ V to the spray needle, were accelerated towards a heated stainless steel capillary at 100 V. Subsequently, they were focused through a skimmer for removal of the excess neutrals and guided towards the electrostatic ion optics using an rf-only quadrupole.

After trapping of the ions, a TTL trigger pulse was applied to the relay switching circuit in the AWG system to connect the AWG output to the transmitter. This was followed by a 3 ms time delay to allow the relay to settle. A second TTL trigger pulse was applied to the AWG to initiate the generation of the loaded excitation waveform for ejection of ions of unwanted $m/z$ values from the cell. After lowering these trigger signals, the ions were excited to a high and coherent cyclotron orbit by a series of single-frequency excitations generated by the Bruker programmable frequency synthesizer (frequency shifted over the excitation range in steps of 20 $\mu$s duration with an increment of $\sim 5.2$ kHz). This coherent motion was detected at an acquisition rate of typically 500 kHz into 128 kbyte data points. The resulting time domain signal was zero-filled to 256 kbyte, followed by discrete Fourier transformation and magnitude calculation and finally transformed to a mass spectrum.

### *5.3.2 Sample Preparation*

The samples investigated are Jeffamine D2000 and cytochrome c and are both commercially available. The Jeffamine sample was obtained from Texaco Chemical Company and measured by means of MALDI-MS. According to the manufacturers data sheet (SC-024 102-0411), the Jeffamine D2000 is an amine-terminated polypropylene glycol with the general structure $H_2N\text{-}(C_3H_6O)_n\text{-}C_3H_6NH_2$ and an average molecular weight of 2000 u. Previously published FTICR-MS investigations on this sample [112] revealed that at least three additional polymer series are present in the D2000 sample at lower masses due to contamination, early termination reactions during polymerization, or oxidation. The matrix in the MALDI experiments was 2,5-dihydroxybenzoic acid (DHB) from Sigma Chemical Co. (St. Louis, MO). The Jeffamine was prepared for MALDI measurements by mixing a 1 M matrix solution in ethanol with an approximately 10 g/L Jeffamine solution in ethanol to give an average molar ratio matrix:analyte = 1000:1. This mixture was electrosprayed onto the stainless steel MALDI probe tip (Section 3.2.2). Approximately 0.1 mL analyte/matrix was consumed during sample deposition.

Cytochrome c of horse heart was measured by means of ESI-MS and was purchased from Aldrich (Milwaukee, WI). Cytochrome c was sprayed from a $\sim 1$ $\mu$M solution with a solvent composition of 68:30:2 MeOH:$H_2O$:HAc. The average molecular weight of cytochrome c was calculated to be 12360.18911 u on basis of its amino acid sequence

[136] (elemental composition $C_{526}H_{842}N_{144}O_{152}S_4$) and the elemental composition of its heme ($C_{34}H_{36}N_4O_4Fe_1$ [137]). It should be mentioned that the mass of two hydrogen atoms was subtracted for each of the two bonds between the heme and the thiol groups of the cysteine residues and that the acids in the heme group were assumed to be protonated.

## 5.4 Testing the Performance by Mass-Selective Ion Isolation in FTICR-MS

MALDI-FTICR-MS spectra of Jeffamine D20000 shown in Figure 5.3 were recorded by summing 100 consecutive laser shots at a trapping delay of 1000 $\mu$s to get a maximum signal-to-noise for the main polymer series.

The spectrum in Figure 5.3 A was recorded without actively ejecting ions from the analyzer cell and hence reflects the ion population initially trapped. It shows that two polymer series are present in the mass range $m/z$ 1000 to 2400. Both correspond to the amine-terminated polypropylene glycols at equidistant intervals of 58 u. The most abundant series was cationized by sodium attachment, and the other series by protonation. The inset with expanded mass scale shows that the naturally occurring isotopes of the component molecules are resolved and that the dominant series originates from sodium cationization, whereas the series at lower abundance is formed by protonation. The ions observed in the mass range below $m/z \sim 1200$ correspond to the additional polymer series that are present in the sample [112]. The abundance of these series is however highly underdetected because trapping was not efficient in this mass range due to the flight-time-induced mass discrimination (Section 3.4.1).

The spectra in Figure 5.3 B and 5.3 C show the effect of ejecting all ions within the mass range $m/z$ 1200-2000 that are not part of the dominant sodium cationized polymer series between the components at $m/z$ 1316 and $m/z$ 1896. This was realized by using SWIFT waveforms with a comb-like excitation profile as is indicated by the dashed lines in the bottom spectrum. The bandwidth of these excitation waveforms was 2.5 MHz, the size 2 Mwords, and the duration $\sim$ 0.2 s. The mass width of the notches in the applied excitation profile was 6.0 u for the isolation of the entire isotopic clusters in the middle spectrum and 1.0 u for the isolation of the monoisotopic peaks in the upper spectrum. The attenuation level of the SWIFT waveform was optimized to the level that ions are just ejected after completion of the waveform. This was done by omission of the broad band excitation and subsequently monitoring the increasing signal from the protonated polymers in a series of measurements in which the attenuation level was decreased (data not shown). The attenuation level at which this signal suddenly disappeared was selected to perform the measurements presented here. At this level, no signal was observed from polymers inside the notches. The upper two mass spectra demonstrate that this efficiently removes the protonated polymer series within the ejection mass range from the analyzer cell. Moreover, the expansions of the mass scale prove that no severe power leakage into the notches occurs because peak intensities and isotopic patterns are not significantly changed. Finally, the efficient isolation of the monoisotopic peaks in the upper spectrum

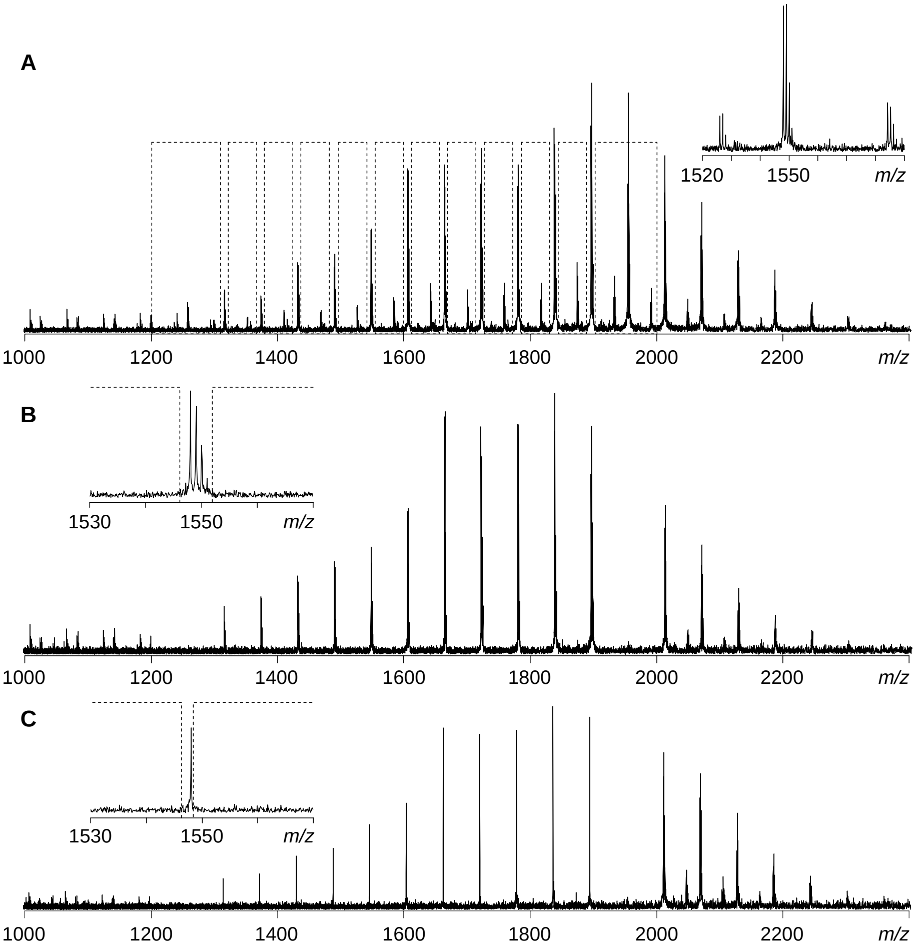

**Figure 5.3:** *MALDI-FTICR-MS spectra of Jeffamine D2000, illustrative of the capabilities of the novel AWG system. The top spectrum (A) was recorded without the application of isolation waveforms. The dashed lines indicate the comb-like excitation profile of the SWIFT waveform applied to obtain the remaining spectra (B & C). The mass width of the notches in the excitation spectrum was 6.0 u (B) and 1.0 u (C), respectively. The insets illustrate the effect of the isolation waveforms.*

is indicative of a frequency selectivity of better than 30 Hz in the isolation event. This value is based on the frequency difference between the isotopic peaks of the 32-mer (the monoisotopic peak at $m/z$ 1954 corresponds to 54929 Hz, the first isotopic peak at $m/z$ 1955 to 54901 Hz).

The frequency selectivity in AWG excitation events was investigated in more detail by ESI-FTICR-MS on cytochrome c. The mass spectrum recorded by broad band excitation using the Bruker frequency synthesizer is shown in Figure 5.4 A. An abundant distribution of ions is observed in which each ion corresponds to a different charge state of the molecular species. The expanded mass scale shows that the mass resolution (here, $(m/\mathrm{d}m)_{50\%} = 24400$ at $m/z$ 824.97) is sufficient to resolve the $^{12}$C and $^{13}$C isotope peaks for the individual charge states. The number of isotope peaks appearing within a single mass unit was determined to identify the number of charges on the ion [138]. In this way it was found that the charge state distribution in Figure 5.4 A ranges between $11+$ (around $m/z$ 1124.8) and $18+$ (around $m/z$ 687.8). The ionizing species was identified by determining the average $m/z$ ratio for the isotopic cluster shown in the expanded

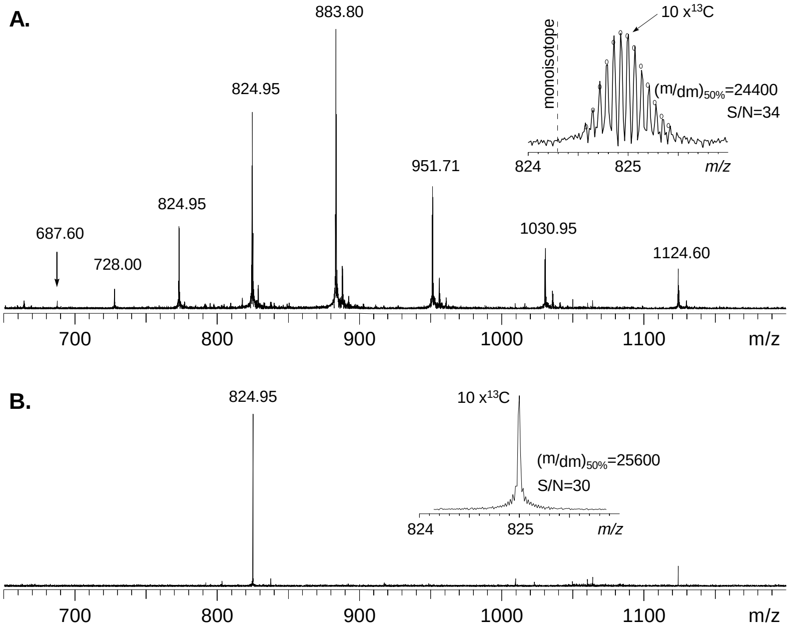

**Figure 5.4:** *Ultrahigh frequency selective SWIFT isolation with the novel AWG system: A) broad band ESI-FTICR-MS spectrum of cytochrome c covering the entire charge-state distribution that ranges between* $11+$ *and* $18+$*; and (B) mass spectrum following the broad band SWIFT waveform shown in Figure 5.5 The insets demonstrate the successful isolation of a single isotopic peak.*

mass scale and multiplying it with the charge state ($z = 15$). Comparison of the result (12374.21 u) with the theoretical mass calculated on basis of the cytochrome c amino acid sequence (12360.19 u) demonstrates that these ions were produced by proton attachment. However, this leaves a discrepancy between the measured and the calculated mass. This is illustrated by Table 5.1, which lists the molecular weights determined from different charge states. In the mass determination it was taken into account that the iron in the heme of cytochrome c is oxidized and carries three charges [137], and it was assumed that the remaining charges were added by the attachment of protons. It is seen that the experimentally determined values differ by typically 2 u from the theoretically calculated one. The deviant values for the 11+, 17+, and 18+ charge states are attributed to their poor S/N ratio. The difference of 2 u is significantly larger than the expected accuracy in the mass determination (which is estimated to be $\sim 10^{-1}$ u). Moreover, it is in agreement with results presented in other publications in which the charge of the oxidized iron was not considered. For example, Banks et al. determined a molecular weight of 12359.13 u from their ESI spectra with the assumption that all charges were the result of proton attachment [139]. Addition of the mass of three hydrogen atoms yields 12362.15 u. Beavis et al. determined with MALDI-ToF [140] a mass of 12360.1 u for the singly charged molecular ion, which gives 12362.1 u. Therefore, it is presently assumed that this discrepancy in mass is not produced by artifacts in the measurements but that the elemental composition of cytochrome c is not unambiguously determined by its amino acid sequence.

**Table 5.1:** *Molecular weights of horse heart cytochrome c, determined from the different charge states in the spectrum of Figure 5.4 A.*

| Charge state | molecular weight |
|---|---|
| 18+ | 12361.68 |
| 17+ | 12361.90 |
| 16+ | 12362.13 |
| 15+ | 12362.11 |
| 14+ | 12362.17 |
| 13+ | 12362.19 |
| 12+ | 12362.29 |
| 11+ | 12362.50 |

In addition to the main distribution, also ion series are observed that correspond to molecular masses that are approximately 60.7 u and 123.2 u larger than the protonated molecular species. These series result from deterioration of the sample due to the storage conditions of the sample solutions and are not observed when fresh samples are studied. For example, an increase in mass of 60.7 u can be explained by the attachment of acetate.

The inset in Figure 5.4 shows an expansion of the mass scale around the 15+ charge state. The circles indicate the theoretical exact masses and normalized relative abundances in the isotopic pattern. This pattern was calculated for the elemental composition of cytochrome c plus two additional hydrogen atoms. The position of the monoisotopic peak and the peak corresponding to ten ${}^{13}$C isotopes are indicated. It is seen that the calculated and the measured patterns match. The deviations between the exact masses and the measured masses were within 0.015 u around the center of the pattern.

The expanded mass scale also reveals the close isotope spacing for the $15+$ charge state. The difference in $m/z$ ratio between adjacent isotope peaks in this charge state is equal to 0.067 u. This corresponds to cyclotron frequency differences of less than 10 Hz at an average cyclotron frequency of 130.2 kHz. Isolation of a single isotope peak from this cluster is evidently challenging and an excellent test for the system's frequency selectivity. This was achieved by tailoring a 1 Mword broad band SWIFT waveform to eject all ions from 474.95 $< m/z <$ 824.95 and from 825.02 $< m/z <$ 1375.02 and to leave ions from 824.95 $< m/z <$ 825.02 unaffected. The time domain waveform (312.5 kHz bandwidth and 1.68 s duration) is depicted in Figure 5.5. Included in the figure is its actual excitation profile, which was obtained by Fourier transformation of the SWIFT waveform after zero-filling to 2 Mword. The inset reveals the ultra-high resolution of the mass notch at $m/z$ 824.865 and predicts a theoretical frequency selectivity of better than

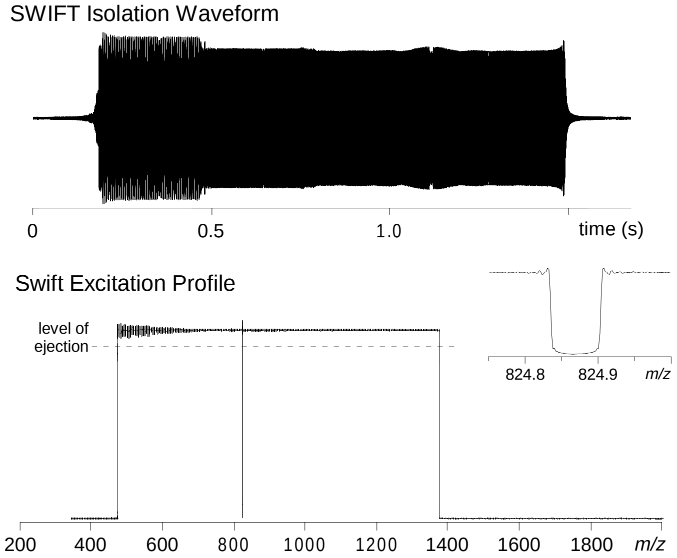

**Figure 5.5:** *Broad band SWIFT waveform and its actual excitation profile used to isolate a single isotope peak from the broad band ESI-FTICR-MS spectrum of cytochrome c. The excitation profile was specified to eject ions from 474.83* $< m/z <$ *824.83 and from 824.90* $< m/z <$ *1374.90. The inset illustrates the ultra-high resolution of the notch in the excitation profile.*

1 Hz.

The mass spectrum recorded after application of this ejection waveform is shown in Figure 5.4 B. It demonstrates that all unwanted ions were successfully removed from the cell. Moreover, comparison of the resolution and the S/N ratio of the peak at $m/z$ 824.85 before and after isolation (see the expanded mass scales in Figure 5.4 A and 5.4 B) indicates that the isolated ions remain unaffected.

Finally, the ejection efficiency around the borders of the isolating notch was investigated in more detail by performing similar experiments in the high-resolution (heterodyne) detection mode. Figure 5.6 A and 5.6 B show the high resolution spectrum without the application of any SWIFT isolation waveforms and one that follows the SWIFT waveform shown in Figure 5.5, respectively. The expanded mass scales illustrate clearly the increased resolution in comparison with the broad band spectra ($(m/\mathrm{d}m)_{50\%} = 97000$ at $m/z$ 824.85). Also some additional low-intensity peaks are observed in the high resolution mode, which were not clearly observed in the broad band spectrum in Figure 5.4 A. These are indicated in the spectrum and correspond to partial sodium cationization (for example, [M+Na+11H]$^{15+}$ instead of [M+12H]$^{15+}$), and oxidized cytochrome c. Fragment ions with eight charges attached are observed around $m/z$ 817.8. The mass spectrum

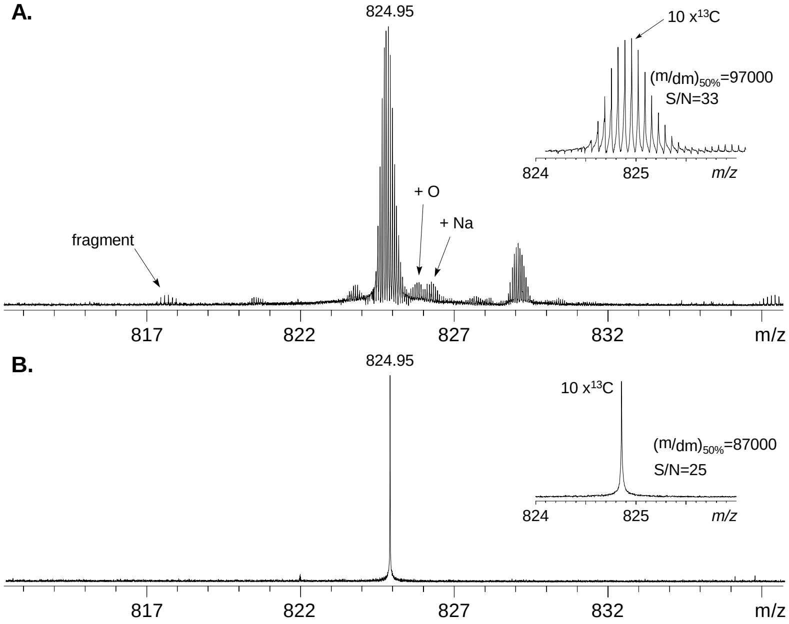

**Figure 5.6:** *High-resolution ESI-FTICR-MS spectrum of cytochrome c without (A) and after applying the broad band SWIFT waveform shown in Figure 5.5 The insets demonstrate the successful isolation of a single isotopic peak.*

recorded after application of the SWIFT ejection is shown in Figure 5.6 B and demonstrates that again all unwanted ions were successfully removed from the cell, whereas the isolated ions remain essentially unaffected.

The frequency selectivity was quantified by performing a series of similar experiments in which the center of the notch was shifted in steps of 0.01 u (corresponding with 1.4 Hz) from $m/z$ 824.95 to $m/z$ 825.05. In these experiments it was observed that a shift of 0.03 u in the center of the notch corresponds to the difference between efficient ejection and efficient isolation. We therefore conclude that the frequency selectivity at the boundaries of the isolation notch was approximately 4 Hz.

## 5.5 Summary and Conclusions

The design of a novel arbitrary waveform generator dedicated to the excitation of ion motions in ion traps has been described. FTICR-MS experiments have been performed with this generator in which monoisotopic components from the molecular weight distribution of Jeffamine D2000 and single isotopes from the charge-state distribution of cytochrome c have been successfully isolated in the analyzer cell. Based on these measurements the frequency selectivity allowed by the system hardware is estimated to be better than 4 Hz. This accuracy is however worse than the resolution in the calculated waveforms ($\ll 1$ Hz). It is presently believed that this is due to off-resonance excitation and not due to frequency instabilities in the AWG hardware. Future experiments based on longer isolation waveforms are envisaged to prove this.

By virtue of the AWG's large memory size and its flexibility in constructing output sequences, the system is ideally suited for complex FTICR-MS experiments such as SWIFT-based two-dimensional mass spectrometry [129] and multistage tandem mass spectrometry. Its stand-alone operation and easy interfacing make the AWG compatible with virtually any experimental apparatus.

Finally, new instrumental developments are currently undertaken, which will make it possible to use the memory of the AWG system for data acquisition too. The main advantage of this development is that it will become possible to acquire broad band transients for several seconds. This implies that mass resolving powers that are presently only available in heterodyne mode will also become available in broad band spectra over the entire mass range.

# 6

# Isotope Beating Effects in the Analysis of Polymer Distributions by Fourier Transform Mass Spectrometry

*The signals of the ions cyclotron orbital motions in Fourier Transform Ion Cyclotron Resonance Mass Spectrometry periodically undergo destructive interference on the time scale of the measurement if the frequencies of these motions are closely-spaced. The result is a beat pattern in the measured time-domain signal. If transients are sampled for less than two beat periods, it is likely that mass spectra obtained by Fourier transformation of these transients will show significant errors in the measured relative abundances. The effect was found to be significant in investigations of synthetic polymer samples, leading to errors in the derived average molecular weights. Here, we present experimental data on synthetic polymer samples which demonstrate that the measured molecular weight distributions exhibit distortions if the acquired transients are short compared to the beating period. These errors decrease for increasing transient lengths and become insignificant when the transient is acquired for longer than twice the beat period. Computer simulations show a similar behavior and indicate that the distortions are induced by isotope beating. By virtue of the newly constructed AWG system (Chapter 5) it was possible to obtain experimental data on an isotope depleted polymer distribution similar to the one studied in the computer simulations. This distribution was produced by SWIFT ejection of all* $^{13}$*C-containing ions from the analyzer cell. Distortions that depend on the transient length are not observed in these spectra. This proves that isotope beating is responsible for distortions in measured molecular weight distributions if transients are acquired for too short durations.*

## 6.1 Introduction

In Chapter 3 it was already discussed that MALDI-FTICR-MS has distinct advantages in the analysis of (synthetic) polymers. However, reasonable care must be taken to reduce the amount of artificial error introduced at each step of the experiment. For example, mass discrimination effects in trapping either externally or internally generated ions can skew the observed oligomer distribution, as was extensively examined in section 3.4. In Chapter 2 it was outlined that the use of SWIFT [121] excitation waveforms with a relatively flat power frequency spectrum reduces artifacts that result from the uneven power distribution found in the commonly used linear chirp excitations [141]. This was one of the driving forces behind the instrumental development described in Chapter 5. Other sources of error include ion densities that induce amplitude errors due to space-charge effects [142], energy-dependent ion trapping [93, 143, 144], and dynamic Coulomb interactions of ion clouds with different frequencies during detection [145].

In this chapter we discuss another newly discovered source of error in measurements of the proper relative abundances of oligomers in a polymer distribution with FTICR-MS. This source of error is inherent to the measurement of the image charge induced on the detection electrodes by the coherent cyclotron motion of ions trapped in the analyzer cell. The detected signal is simply the sum of the instantaneous phases and amplitudes of the individual oscillators. Depending on the relative phase of the oscillators, this may lead to constructive or to destructive interference. The result is a complex waveform that contains a manifold of frequency components, which correspond to the different oscillators.

It is often observed that interference of the signals from ions of slightly different $m/z$ produces modulation effects in the measured transients. This is especially the case in ESI-FTICR-MS experiments, because the frequency separation between isotopes may become very small for highly charged, high mass ions, This phenomenon is known as isotope beating [146] and is illustrated by the data in Figure 6.1, which shows the time-domain signal corresponding to the ESI-FTICR-MS spectrum of cytochrome c presented in Chapter 5 (Figure 5.6 A).

The theoretical description of modulation effects between closely spaced oscillators is fairly simple, and can be derived from basic trigonometric entities [146]. In the case of isotope beating, the modulation frequencies are determined by the frequency separation between adjacent isotopic peaks. Although the number of isotopic peaks for heavy ions can be quite considerable, the variation in the frequency difference between any pair of adjacent peaks is small. This allows the estimation of the overall beat frequency by the characteristic frequency spacing for a given charge state. This characteristic beat frequency (in Hz) is in good approximation given by:

$$f_{\text{beat}} \simeq \frac{zB}{2\pi m^2} \times 10^8 \qquad (6.1)$$

Here, $z$ is the integer number of elementary charges on the ion, $m$ is the average ion mass in u, and $B$ is the magnetic field strength in Tesla. For example, cytochrome c ions with

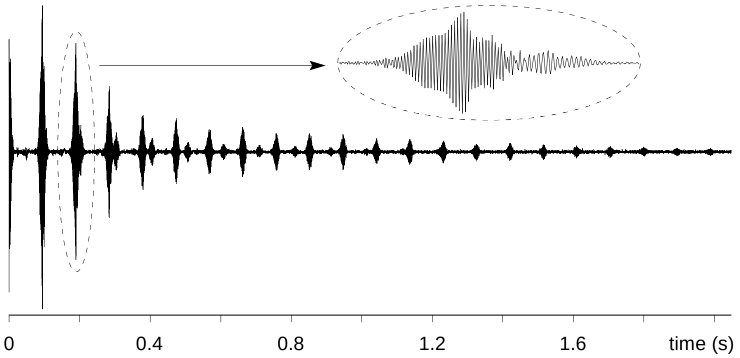

**Figure 6.1:** *Time domain transient measured at a magnetic field strength of 7 T for the 15+ charge state of cytochrome c (MW = 12,358). The periodic regions of diminished signal with a beat frequency of 11 Hz (eqn. 6.1) clearly illustrate the effect of isotope beating. Additional beats are observed from ions of other molecular weights that are present at low intensity.*

a average mass of 12,358 and 15 elementary charges attached exhibit a major beat of 11 Hz ($\tau = 90$ ms) at a magnetic field strength of 7 T.

Some degree of modulation is usually also observed for other ionization techniques in the time domain transients of FTICR-MS spectra of most materials. However, the modulation periods for heavy ions produced by ESI can approach 10-20 seconds in length, even for highly charged ions. High mass ions, with large numbers of closely spaced isotopic peaks, produce a transient signal in which short bursts of data are separated by long periods (dictated by the modulation frequency) of little or no observable signal above the broadband spectral noise (Figure 6.1). Although the mass information provided by these transients is not compromised by modulation of the time domain data, longer acquisitions are required to achieve high resolution spectra that can be used to determine the charge state from the separation of isotopic peaks [146].

Previous work on isotopic modulation effects concerned the effect on mass resolution [146], but the impact on the magnitude of spectral peaks was not examined. However, the key question for polymer analysis is to what extent the beating phenomenon alters the individual intensities of mass peaks and how these changes affect the quantitative characterization of polymer distributions. Therefore, the effect of isotope beating on the measured relative abundances of a distribution of ions is investigated in this chapter. Experimental data on synthetic polymer samples are presented, which demonstrate that the measured molecular weight distributions exhibit distortions if the acquired transients are short compared to the beating period. The behavior of transients was numerically modelled to investigate the effect of multiple modulation frequencies on the determination of polymer distributions independently of other significant physical effects in the experiments. These computer simulations showed the same behavior as the experimental data.

Finally, experimental data on an isotope depleted polymer distribution are presented. This distribution was produced by SWIFT ejection of all $^{13}$C-containing ions from the analyzer cell. The absence of transient length dependent distortions in these measurements prove unambiguously that isotope beating is responsible for distortions in measured molecular weight distributions if transients are acquired for too short durations.

Although the data and models presented here are primarily involved with the mass information found in polymer distributions, it is reasonable to assume that samples with multiple, closely spaced masses such as petrochemicals, combinatorial libraries, and natural products would exhibit similar effects.

## 6.2 Experimental

### *6.2.1 Instrumental*

MALDI FTICR-MS spectra were acquired with the heavily modified APEX 7.0e FTICR-MS (Bruker-Spectrospin, Fallanden, Switzerland) equipped with a 7-T magnet. Instrumental and experimental details can be found in Chapter 2. In short, the MALDI samples were deposited on the stainless steel tip of a direct insertion probe and introduced into the external MALDI ion source via a vacuum lock. Ions were produced by irradiating the samples with the 337.1 nm wavelength beam of a nitrogen laser and subsequently transferred by electrostatic ion optics to the analyzer cell. After trapping, the ions were excited to a large, coherent cyclotron orbit and detected at an acquisition rate of typically 500 kHz into 128k data points. This time domain signal was zero-filled to 256k, followed by discrete Fourier transformation and magnitude calculation.

Ion selection was carried out using the home-built AWG system (Chapter 5). The experiments described in this paper use an adapted SWIFT algorithm [60, 121, 125] to distribute the excitation power over the duration of the excitation pulse. The calculated waveform is downloaded from the SGI workstation into the AWG memory. A small relay switching circuit connects either the output of the programmable frequency synthesizer or the AWG output to the transmitter. A TTL trigger pulse toggles this switching circuit. A second TTL trigger pulse is generated 3 ms later, when the relays have settled. This pulse triggers the AWG to output the loaded excitation waveform.

### *6.2.2 Sample Preparation*

The poly(methyl methacrylate) (PMMA) standard with an average molecular weight of 1140 was obtained from Polymer Laboratories (Amherst, MA). DHB (2,5-dihydroxybenzoic acid) was used as the MALDI matrix and was purchased from Sigma Chemical Co. (St. Louis, MO). The MALDI samples were prepared by mixing a 1-M matrix solution in ethanol with an approximately 10-g/L analyte solution in ethanol to yield a molar ratio matrix:analyte = 1000:1. This mixture was electrosprayed onto a stainless steel probe tip.

Approximately 0.1 mL analyte/matrix was consumed during sample deposition. The total sample loading on the probe was approximately 10 ng.

### *6.2.3 Numerical Simulations*

To separate the effects of signal interactions from other physical phenomena, simulated transients were evaluated. These transients were produced by M. Easterling with a custom program [147] that runs on a 180 MHz MIPS R5000 based Silicon Graphics workstation (Silicon Graphics, Mountain View, CA) and uses arrays of mass and abundance values describing the fictional ion population in the analyzer cell. The mass and abundance values were either coded manually or generated automatically by providing the program with key (polymer) distribution parameters such as mean, standard deviation, and repeat mass. Isotopic patterns were calculated using the IsoPro program [148]. The amplitude of the transient signal $I$ that would be measured for the fictional ion population is calculated for different time points according to

$$I(n) = \sum_i \sum_j A_i C_j \sin\left(\frac{qB}{m_{i,j}} n\Delta\right) \tag{6.2}$$

where $A_i$ is the abundance of the oligomer with a monoisotopic mass $m_{i,0}$, $C_j$ the natural abundance of the $j$-th isotope at mass $m_{i,j}$, $qB/m_i$ its unperturbed cyclotron frequency, and $\Delta$ is the time step (or fictional reciprocal sample rate). In physical terms, the instantaneous amplitude is calculated by summing together the amplitudes for the individual ions. It is hereby assumed that all ions are instantaneously excited to a high cyclotron radius and that all phases are initially equal to zero. Broad band noise was not included in the simulation, and isotopic abundance ratios for each oligomer were treated the same as that of the central peak, as the abundances do not vary greatly for the major peaks in distributions with low polydispersity indices. Actual experimental conditions with respect to experimental phase lag due to chirp excitation, the delay between excitation and detection or ion cloud evolution effects such as dephasing [149, 150] signal locking [151–154], or dampening [155] were not considered. Data manipulation and evaluation including FFT and mass calibration and were performed using the XMGR data analysis program compiled for the SGI workstation. This program assisted in handling the large data sets produced by the simulations, which approached 30 MB in size. All simulated distributions were windowed with the Hanning function prior to the Fourier transformation. Additionally, the data sets were zero-filled to eliminate significant random errors in intensity. Data sets shorter than 256 kword were zero-filled to 256 kword, while 256 kword transients were zero-filled to 512 kword.

## 6.3 Effect of Isotope Beating on Measured Polymer Distributions

### 6.3.1 Distortions in Measured Distributions

A wide range of industrial homopolymers are extensively used for diagnostics and calibration, in particular in MALDI-FTICRMS [113, 143]. Also within the framework of this thesis, many experiments were carried out on polymeric samples to characterize instrument performances and optimize experimental conditions utilizing their characteristic symmetrical molecular weight distributions. It was discovered, however, that changes in the size of the data set of acquired spectra results in changes in the observed polymer molecular weight distribution. This effect is illustrated with MALDI-FTICR-MS measurements on a PMMA1140 sample. Figure 6.2 shows a measured time domain signal. It was acquired over 131 ms at a fixed trapping delay of 1000 ms (i.e., no correction for the flight-time distribution distortions was applied) at a sample rate of 1 MHz. Isotope beating is not readily recognized in the depicted signal. This is not surprising, because the various different beating frequencies associated with the different oligomers spread the beats evenly in time.

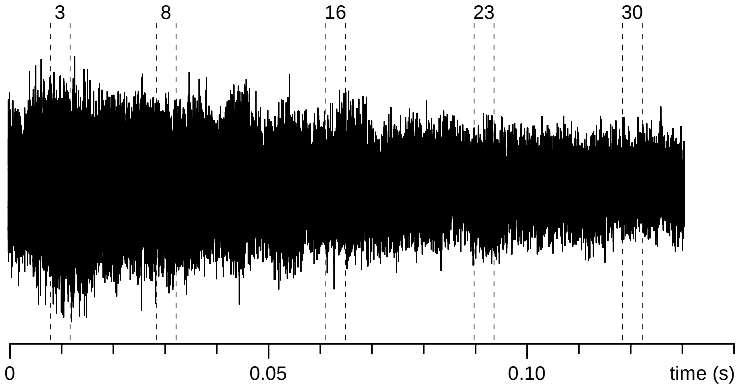

**Figure 6.2:** *Measured time domain transient for a MALDI generated PMMA1140 distribution. The dashed lines indicate the boundaries for sets of 4 K data points extracted at various times to compare the instantaneous distribution of amplitudes (Figure 6.5).*

The dependence of the observed PMMA distribution on the size of the data set is examined by Fourier transformation of different portions of the transient in Figure 6.2. The results are shown in Figure 6.3. For the top spectrum (Figure 6.3 A), the complete data set was part of the calculation. The observed distribution resembles the expected profile for this sample given the mass discrimination during the ion transport. The data set was truncated to 64 kword and 32 kword for the spectra in Figure 6.3 B and 6.3 C, respectively. Although a regular distribution is generally retained, it is clearly visible that the distribution is skewed and shifted about the center mass for smaller data sets.

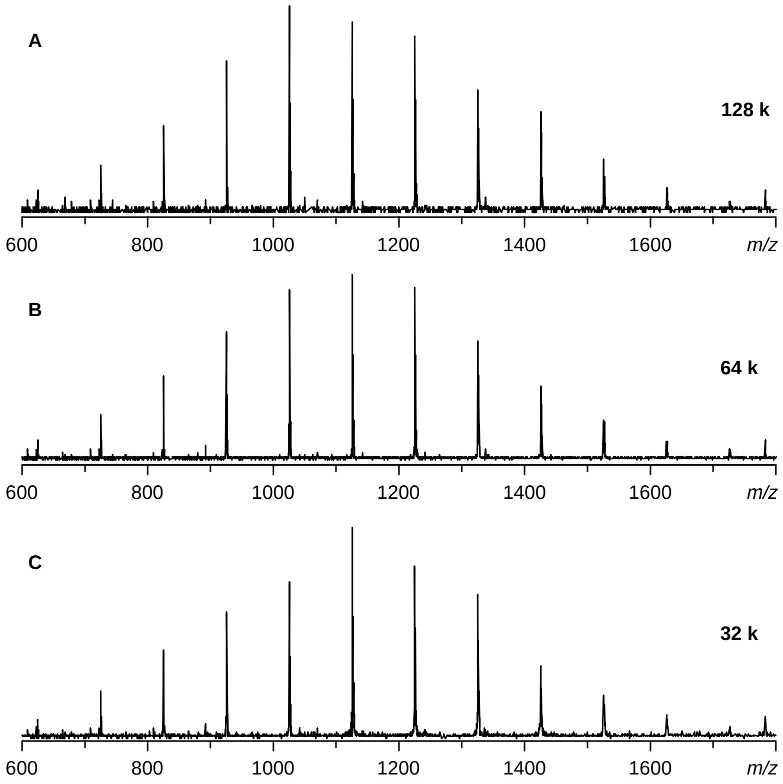

**Figure 6.3:** *MALDI-FTICR-MS spectra of a PMMA1140 distribution obtained by Fourier transformation of the full 128 kword time domain data set (A), the first 64 kword (B), and the first 32 kword of the data set (C).*

In Figure 6.4 it is demonstrated that modulation effects are present in the transient of Figure 6.2 by examination of small portions of the transient. It shows the contour plot of mass spectra obtained by transformation of 1 kword segments of the PMMA transient as a function of their occurrence in the transient. The plot clearly depicts that the signals of the individual components of the molecular weight distribution exhibit profound beating patterns. The frequencies of the beating patterns were determined from the contour plot and are listed in Table 6.1. Also the theoretical frequencies, which were calculated with eqn. 6.1, are included. It shows that the observed and the calculated values agree well. This indicates that isotope beating causes the staggered nature of the contour plot.

The contour plot in Figure 6.4 also indicates that the mass dependency in the beating frequencies causes "instantaneous" errors in the molecular weight distribution. This could well explain the changes in the measured distributions for different acquisition times. For example, a sampling time of less than 0.02 s would not completely sample the first beat

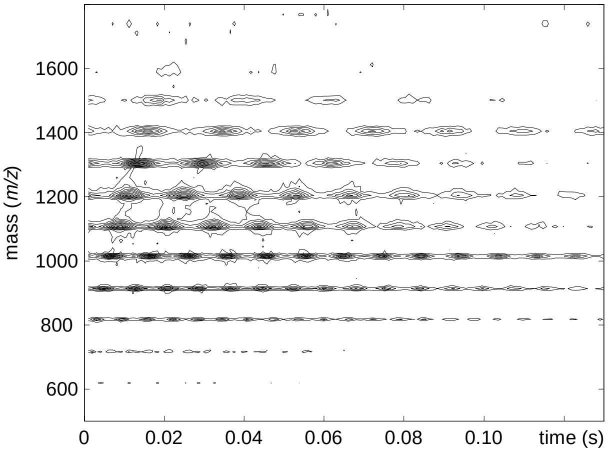

**Figure 6.4:** *Contour plot of PMMA1140 mass spectra obtained by Fourier transforming 1 kword segments of the transient in Figure 6.2 as a function of the position of the segment in the transient (i.e., time). An intensity modulation is observed for each component of the oligomer distribution.*

**Table 6.1:** *Beating frequencies of the components of the PMMA1140 distribution. The observed values were determined from the contour plot in Figure 6.4, the theoretical values were calculated with eqn. 6.1.*

| Mass (u) | Observed Beating Frequency (Hz) | Theoretical Isotope Beating Frequency (Hz) |
|---|---|---|
| 1425 | 54 | 55 |
| 1325 | 62 | 63 |
| 1225 | 76 | 74 |
| 1125 | 87 | 88 |
| 1025 | 104 | 106 |
| 925 | 127 | 130 |
| 825 | 160 | 164 |

of the $m/z$ 1425 oligomer and therefore would underestimate its abundance. This effect is even stronger than is suggested by the contour plot, as is illustrated with the spectra shown in Figure 6.5. The PMMA transient was split in 32 blocks of 4 kword each in order to obtain these spectra. Selected blocks, which are indicated in Figure 6.2 with dashed lines, were transformed into mass spectra. The equal length of the blocks makes that the spectral line width is similar in all spectra so that peak height, rather than area, can be used as a consistent measure of relative ion abundance. It is seen that each section of the transient produces a set of significantly different amplitudes. In addition, comparison of the spectrum obtained from the full data set (Figure 6.3 A) with those of the selected blocks reveals that it matches nowhere. It is obvious that this raises serious doubts about the correlation between the measured and the true ion population in the analyzer cell.

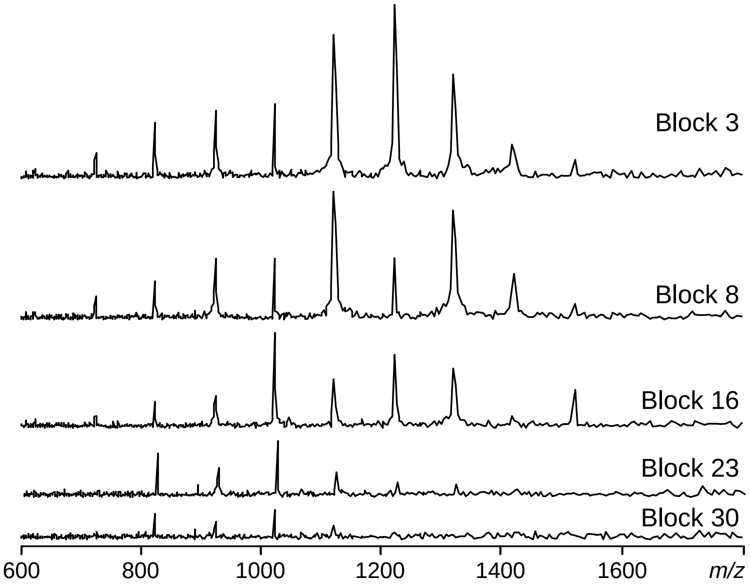

**Figure 6.5:** *MALDI-FTICR-MS spectra of the PMMA1140 distribution for the selected 4 kword blocks (denoted in Figure 6.2). Random oscillations of mass intensities are observed for each block.*

### *6.3.2 Numerical Simulation of the Distortions*

The effects of signal interferences on the spectral amplitude distribution can not be completely determined *in situ*. Although the frequency dependent power differences resulting from chirp excitation might be eliminated by SWIFT excitation [121], and space charge amplitude effects could be reduced by using a relatively low ion population, several other uncontrollable or unknown processes might effect the phase or amplitude of the rotating ion packets over time [150, 151, 156, 157]. To avoid these problems, numerically calculated time domain transients were used to investigate the effect of interference between closely-spaced isotopic frequencies on the measured polymer distributions. In these numerical investigations, dynamic processes that occur naturally during ion detection such as broadening mechanisms, collision induced signal dampening [155] and signal locking [149, 152, 154, 158] were not considered.

Two transients of 256 kword size were generated for a molecular weight distribution closely matching that of a PEG distribution with average molecular weight of 2030 u. One was the result of summing sine waves with frequencies corresponding to each of the peaks including isotopes, whereas the other contained only the monoisotopic masses at the polymer repeat interval. Frequencies were calculated for a 4.7 T magnetic field strength. Transformed data using Hanning apodization for the leading 32 K points of the isotope containing data set is shown in Figure 6.6 A. For comparison with expected values, theoretical peak magnitudes used to generate the waveforms are shown as circles with the highest abundance value normalized with the transformed data set. Although the

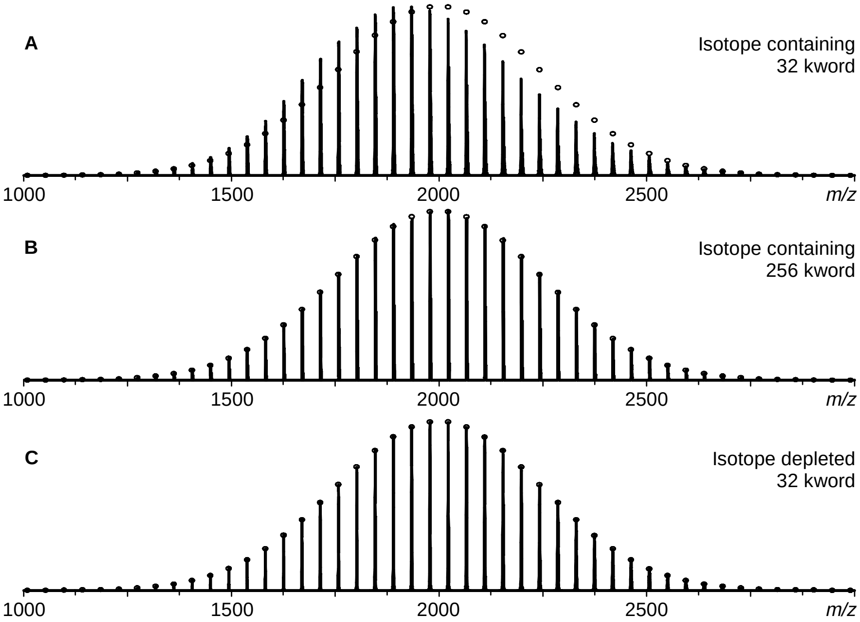

**Figure 6.6:** *Mass spectra obtained by Fourier transform of computer generated transients corresponding to an isotope containing (A& B) and a monoisotopic PEG2000 mass distribution (C). For the top and bottom spectra, only the first 32 kword data points were part of the calculations, whereas the middle spectrum was the result of the full 256 kword transient. The circles correspond to the abundance values of the distribution used to generate the transient.*

distribution is somewhat symmetric, skewing in favor of the lower half of the distribution is observed for the short transient from the isotope-containing model. These errors resemble those found for experimentally-obtained transients of similar length (data not shown). Figure 6.6 B shows that the full 256 K data set transforms into a mass distribution that closely matches the expected values for the isotope-containing transient. Figure 6.6 C shows the transformation of the monoisotopic time domain data of equal length as in Figure 6.6 B. The masses calculated in this case lie within the peak heights of the model distribution and shifts in the centroid distribution are not apparent. A qualitative correlation between these results and experimental data indicates that the centroid shifts observed for polymer distributions are mainly attributable to the interference effects of closely-spaced isotope frequencies. It should be stressed that while amplitudes are affected, the measured frequencies are not altered by this effect, as dictated by the superposition theorem [57].

The effect of “instantaneous” errors in the amplitude distribution, which was observed in the experimentally obtained PMMA distribution (Figure 6.5), was also numerically investigated. The computer generated transients corresponded to the expected distribution of singly charged PMMA ions with an average molecular weight of 1000 u. They were calculated for a 7 T magnetic field strength and were of 128 kword size (131 ms transient for 1 MHz sampling rate). Again, one was calculated for the isotope-containing and one for the monoisotopic case. The data sets were split into 32 blocks containing 4 kword of data per block, and selected blocks were transformed into mass spectra to evaluate the signal evolution in time. As in the experimental data, the equal length of the blocks allowed the use of peak heights as a measure of relative ion abundance. Figure 6.7 shows the results of Fourier transformation of the selected blocks of the isotope-containing computer-generated transient. Each section of the transient is observed to produce a set of significantly different amplitudes for the given range of masses, although the distributional shape is fairly well defined for all of the data blocks. Comparison with the measured distributions (Figure 6.5) reveals that the variations in the numerically simulated data set are similar to those observed in the measured distributions. However, the S/N ratio in the experimentally obtained mass spectra is observed to decrease towards the end of the transient, whereas in the case of the simulated transient this ratio remains roughly constant. This effect results from signal dampening, which was not included in the simulations. Computer-generated mass spectra from monoisotopic oligomer distributions, shown in Figure 6.8, indicate no observable oscillation in the magnitudes of the polymer masses, but rather exhibit identical amplitudes for each transformed block. This demonstrates that the presence of isotope beating is the origin of variations during the lifetime of the transient in the amplitude associated with each oligomer in the mass distribution. It also indicates that the actual distribution is measured if transients are acquired sufficiently long or if the naturally occurring isotopes are removed.

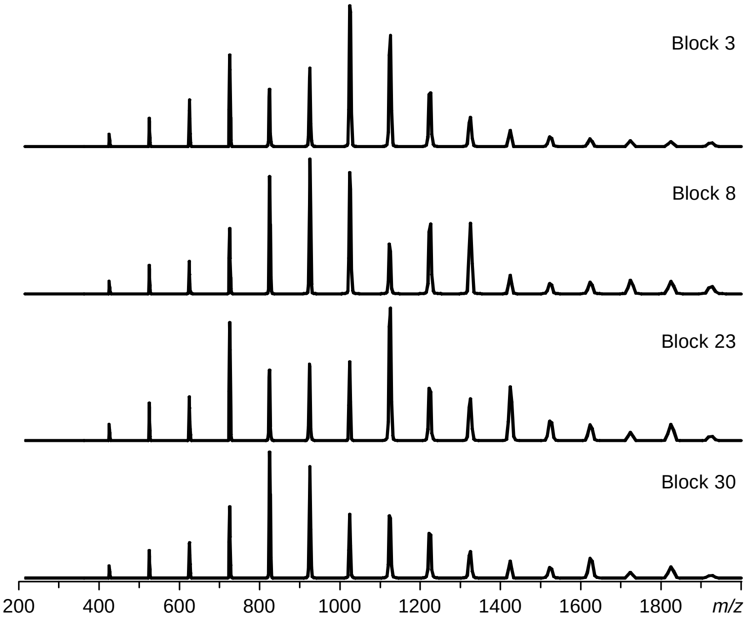

**Figure 6.7:** *Spectra obtained by Fourier transforming selected 4 kword blocks of computer generated transients corresponding to an isotope containing PMMA1140 mass distribution.*

### 6.3.3 Elimination of the Beating Induced Distortions by Removal of Isotopes

To prove that oscillations in the measured relative abundances of the components of a polymer distribution can be fully attributed to isotope-induced beat frequencies, isotope depleted experimental data were obtained for the PMMA sample. In these experiments, the arbitrary waveform generator was used to isolate the monoisotopic peaks by elimination of all isotopes from the analyzer cell by resonant ejection. Figure 6.9 shows mass data obtained by transformation of 1 kword segments of the monoisotopic transient as a function of time. It shows that the beating patterns that were observed in the contour plot in Figure 6.4 are no longer present.

In Figure 6.10, mass spectra of the full transient and selected blocks of 4 kword size are presented. As observed in the simulations, the shape of the mass distribution remains unchanged over the entire transient. Comparison of the mass spectra of the entire transients in Figures 6.5 and 6.10 reveals that the molecular weight distribution changes significantly by removal of the isotopes from the analyzer cell. Closer inspection of the distribution in Figure 6.10 indicates that the abundance of the $m/z$ 925 ion is severely underestimated. Imperfections in the isolation waveforms come to mind as a potential

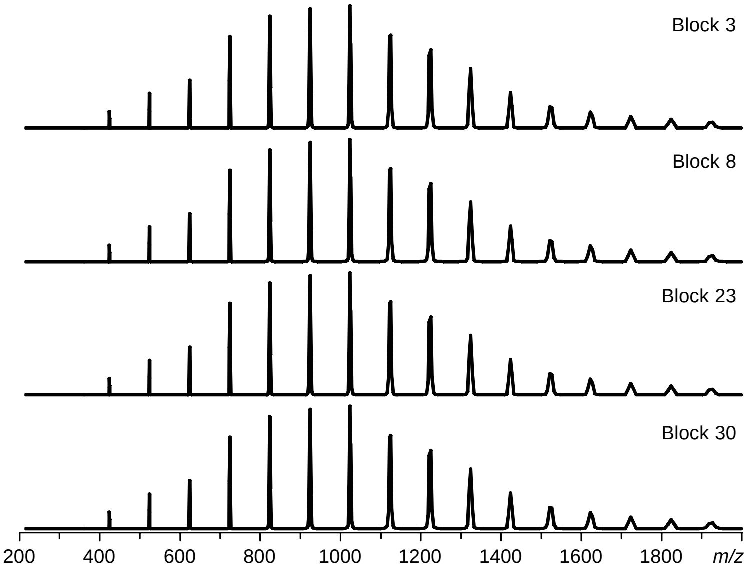

**Figure 6.8:** *Spectra obtained by Fourier transforming selected 4 kword blocks of computer generated transients corresponding to a monoisotopic PMMA1140 mass distribution.*

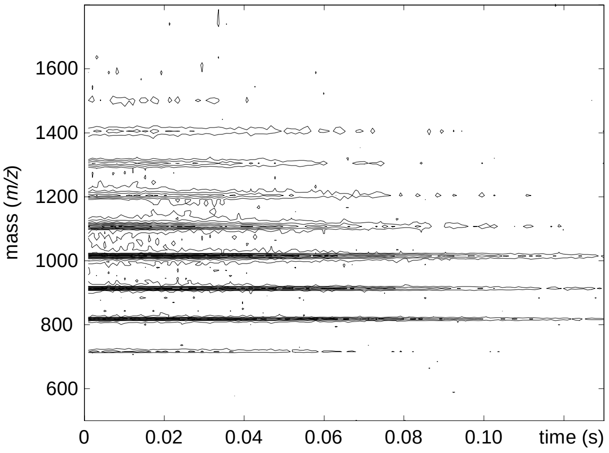

**Figure 6.9:** *Contour plot of PMMA1140 mass spectra obtained by Fourier transforming 1 kword segments of the transient measured from the monoisotopic distribution as a function of the position of the segment in the transient (that is, time). No intensity modulation is observed.*

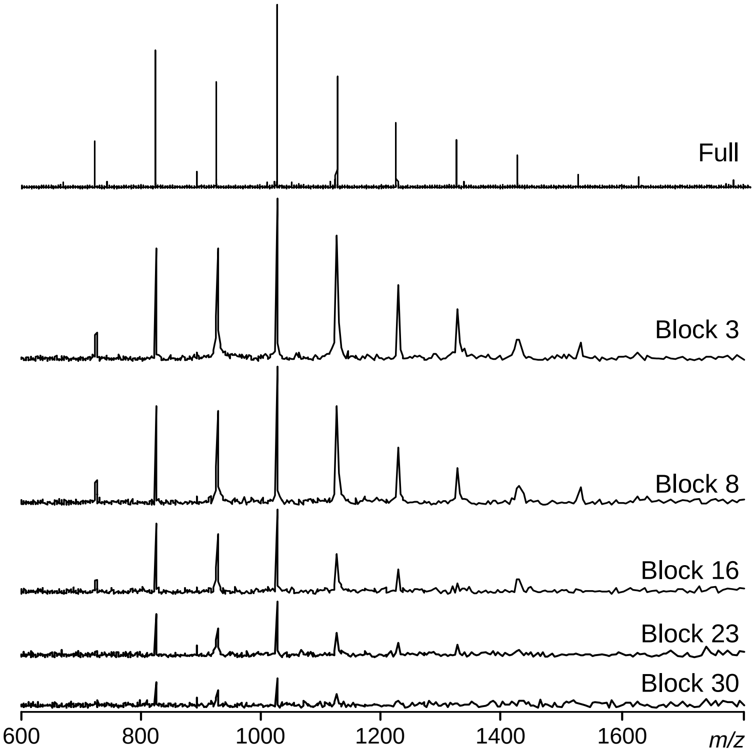

**Figure 6.10:** *MALDI-FTICR-MS spectra of the isotope depleted PMMA 1140 distribution for the full transient and selected 4 K blocks. Abundances are not observed to vary significantly as in the isotope containing spectra shown in Figure 6.5.*

explanation of this underestimation. Waveform imperfections could affect the trapped ion distribution through off-resonance excitation. However, it is unlikely that this would affect only one component in the distribution as all notches in the frequency spectrum are symmetrically centered around the monoisotopic peaks and of equal amplitude. Furthermore, previous isolation experiments have never revealed such effects. Another explanation could be a variation in ion cloud evolution. If we assume that the experimentally determined distribution in Figure 6.10 represents the actual ion population in the cell, it is striking to see the similarity between the spectra of block 23 and 30 in Figure 6.5 (containing all isotopes) and Figure 6.10 (containing only the monoisotopic oligomer ions). The convergence of these two series of spectra is most likely a result of ion cloud evolution that favors the most populated mass channels. This effect has recently been attributed to coulombic shearing forces that preferentially dephase sparser ion clouds causing them to dampen before the denser ion clouds [159]. Additionally, the weak presence of only a few mass channels virtually eliminates the beating effect, as observed as smoothness in the contour plots. As a result of these effects, the "instantaneous" mass distributions for both the isotope containing and depleted transients are observed to converge over the duration of the transient. The similarity of the final mass spectra from the final blocks of data supports our contention that the initial oligomer distributions were the same.

Examining small pieces of the time domain transients would be expected to yield mass spectra with varying amplitudes if beating effects created a discriminating sampling condition. In this case, a non-uniform number of maxima, or beats, are sampled for each frequency in the spectrum. Of greater importance to the analytical study of polymers is how the beating phenomena affects amplitude information for larger data sets, those in which the sample size provides Fourier-limited resolving power for baseline isotope separation. Experimental observations analogous to the one presented in Figure 6.3 (data not shown) indicated that centroid shifts are less significant for larger data set sizes. Table 6.2 shows that the theoretically produced data sets also exhibit this behavior. The calculated weight average for the isotope-containing PEG2000 theoretical distribution with an expected average molecular weight of 2032.13 u is seen to drop from a 5% error for the 32 kword data set, to an error of about 1% for the 128 kword transient. The 32 kword transient would represent an acquisition time of about 66 ms sampling for a bandwidth of 250 kHz, slightly longer than the isotopic beat period for the central mass (58 ms). The 8 ms sampling time provided by the 4 kword transient only represents about 15% of the beat period, resulting in large errors observed for transients of that length. A significant decrease in error is observed for the 64 kword transient, which utilizes 131 ms of magnitude information and contains at least two isotopic beats for each component of the distribution. From these data, it can be inferred that sampling for a period equal to the duration of two isotope-induced beats should be a minimum requirement to obtain a reasonable quantitative description of a polymer distribution. Slightly greater precision is obtained by further averaging of the instantaneous differences for an isotope containing distribution, as mentioned above for the 128 kword transient which samples more than four isotope beats of the center mass.

**Table 6.2:** *Average molecular weights calculated from theoretical transients of different length for a PEG 2000 distribution with an average molecular weight of 2032.13 u. Significant error is observed for the small data set of the isotope containing transient The error is sharply reduced as more data is sampled. In contrast, the data generated for monoisotopic distributions provides an accurate average molecular weight even for small data sets.*

| data set size | with isotopes | | without isotopes | |
|---|---|---|---|---|
| 32 kword | 1922.49 u | (-98.64 u) | 2031.26 u | (-0.87 u) |
| 64 kword | 2024.93 u | (-7.20 u) | 2030.00 u | (-2.13 u) |
| 128 kword | 2029.45 u | (-2.68 u) | 2031.41 u | (-0.72 u) |

As determined earlier, the errors for the monoisotopic distribution are not observed to significantly fluctuate for changes in the size of the data set. These results quantitatively support the earlier finding that longer transients tend to provide better molecular weight values for polymers. The longer sampling times inherently provide larger windows in which the disparity in the number of amplitude maxima for represented frequencies becomes smaller.

## 6.4 Conclusions

To accurately measure relative abundances for large distributions of ions that contain closely-spaced masses, transient duration must be considered to avoid the errors produced by isotopic beating in the time domain transient. The appropriate duration will depend on the magnetic field strength and mass and intensity distributions. Providing an analytical expression for the required sampling time for polymers is somewhat complex because the beat period is significantly different for the two ends of the distribution. To be conservative, the minimum sample time should cover several beat periods calculated for the frequency difference between isotopic peaks at the high mass end of the oligomer distribution. Verification that the transient is sufficiently long would require the performance of Fourier transformations on multiple truncations of the data set. As described earlier, the distributions will converge to a given central value as the data set size is increased. Convergence of the centroid indicates that sufficient sampling has been performed. It should be noted however, that the data found towards the end of the experimentally obtained transient is usually weighted much lower than that found at the beginning due to collision-induced signal dampening [155]. Also other temporally-evolving effects such as non-uniform decay and magnitude dependant ion cloud destabilization [145] should be considered when seeking longer transients. These considerations aside, accurate relative intensities can be obtained by sampling sufficient data points or by measuring isotope depleted spectra.

Finally, it is worth mentioning that the strategy of removing isotopes from the ICR-cell is also promising in the determination of the charge state of highly charged, high mass ions. For example, if the beating period is larger than the dampening constant of the transient, it would not be possible to detect the second beat in the transient. This is however required for isotopic resolution in the mass spectra [146] and, consequently, the charge state can not be determined from the mass-to-charge difference between adjacent isotopes. A set of experiments in which a charge state is isolated with increasing resolution could solve this problem. After all, if the isolated mass interval becomes smaller than the isotopic separation, only a single isotope would remain inside the ICR-cell. This would be expressed by a sudden increase in transient length. The charge state can than be determined from the width of the isolated mass interval.

# 7

# Probing Mass Discriminations and Mass Shifts in the ITMS Mass Spectra of Externally Generated MALDI Ions with Synthetic Polymers

*The design and performance of a newly configured external ion source Matrix Assisted Laser Desorption and Ionization quadrupole Ion Trap Mass Spectrometer (MALDI-ITMS) is described. The performance was characterized in detail with respect to mass discrimination effects and space charge induced mass shifts. Mass dependencies in the trapping efficiency were probed by comparison of measurements of poly(methyl methacrylate) standards in the mass range $m/z$ 400 to 3400 with MALDI-TOF-MS measurements of the same samples. The results indicated that it is possible to determine ideal experimental conditions for analyzing mass ranges smaller than 1000 u with negligible mass discrimination. This was demonstrated on the basis of measurements on a tri-block copolymer of poly(ethylene oxide) poly(propylene oxide). Mass measurements were observed to be highly influenced by the magnitude of the trapped ion population in measurements of phtalocyanine blue and poly(ethylene glycol). Consequently, reproducible results can only be obtained by controlling the total space charge in the trap. In MALDI experiments, this can be achieved by tuning the laser power just above threshold. This approach allowed the mass determination of three different end groups in a complex Jeffamine D2000 sample with an accuracy of better than 0.1 u.*

## 7.1 Introduction

It was already discussed in Chapter 4 that soft ionization techniques, which minimize fragmentation during ionization and thus produce (pseudo-) molecular ions, have proven to be most successful for lifting and converting macromolecules from the condensed phase to gaseous ions. Within this range of techniques, especially electrospray ionization [160] and matrix-assisted laser desorption/ionization (MALDI) [9] have proven their importance in providing accurate and detailed molecular weight data on high molecular weight materials. Additional properties of MALDI that make it especially suited for many applications include the dominance of singly-charged (pseudo) molecular ions (which makes the resulting mass spectra easier to interpret) and its tolerance for salts, buffers and other common additives and impurities. Since its introduction by Tanaka and coworkers [33] and by Karas and Hillenkamp [32] the technique has successfully been applied to volatilize and ionize a wide variety of molecules, such as peptides, proteins, oligosaccharides, and synthetic polymers. Several reviews illustrate the continuously growing scope of MALDI applications [16, 17, 34].

Traditionally, MALDI is coupled to time-of-flight (providing high sensitivity and a theoretically unlimited mass range) [83, 87], or Fourier transform ion cyclotron resonance mass spectrometers (providing superior mass accuracy, mass resolution and multistage tandem mass spectrometry) [108]. A relatively new and unexplored area is the use of the quadrupole ion trap mass spectrometer (ITMS) in analytical applications of MALDI. The ITMS seems particularly well-suited to combine with MALDI. For example, the pulsed nature of the ion production in a MALDI ion source matches well with the pulsed operation of the ITMS, whereas the capacity of the ITMS to store all ions created in the MALDI process, irrespective of the time scale in which these were formed, offers the possibility of panoramic registration of the ions from each laser shot. Moreover, the ITMS provides ultra-high sensitivity in the measurements and possibilities for multistage tandem mass spectrometry ($MS^n$). These are great potentials for the analysis of large molecules in complex mixtures.

Various publications have dealt with the coupling of the MALDI ionization technique and ITMS, which was realized either by performing the MALDI ionization event near the trap or by producing MALDI ions in an external ion source and subsequently transferring these ions to the trap. In the near-trap geometry, the MALDI samples were positioned near the internal surface of the ring electrode (radial introduction) [161–163] or at one of the end cap electrodes (axial introduction) [164]. The generation of ions in an external ion source has obvious advantages, such as flexibility in the nature and size of the samples and switching of ion sources [165–168]. Despite the attractiveness of a MALDI-ITMS instrument outlined above, these investigations encountered several problems revealing that this coupling is not trivial. Crucial among these is the efficiency in the trapping of the MALDI ions. Ions produced by MALDI have wide, mass-independent velocity distributions [96]. Therefore, difficulties in the trapping of ions over wide mass ranges without large (mass-dependent) losses can be expected. In the early experiments, no sophisticated trapping schemes were employed, and the MALDI ions are injected into a constant trapping field (static trapping). Trapping is realized by reducing the kinetic energy of the ions by means of collisions with buffer gas molecules. Several theoretical studies have discussed this process [169–171] and experiments utilizing this method of trapping have been reviewed extensively [172, 173]. The main drawback of this method is found to be a mass dependent, relatively low, trapping efficiency, where the amplitude of the rf field is found to determine the ion mass at which maximum trapping efficiency occurs [174, 175]. Recently, new methods for improved trapping of ions produced in a pulsed ionization technique have been developed. It has been demonstrated that the ion potential energy can be reduced if the rf field is switched on after the ions reached the central region of the trap, whereas it is gated during ion injection [176]. Following an alternative method, which is called dynamic trapping [177–179] the rf field is initially set to a low level to allow the ions an easy penetration of the trapping field. Subsequently, the amplitude of the trapping field is rapidly ramped to a high level to realize trapping before the ions have reached the opposite trap boundary and are lost. In the case of a near-trap geometry, dynamic trapping was demonstrated to give an improvement in the trapping efficiency of 1 order of magnitude [164]. In a more subtle version, called matched dynamic trapping [180], the trapping efficiency was found to be improved by an additional factor of 4 for an external source geometry. This improvement was accomplished by initially ramping the amplitude of the trapping field to an even higher level, followed by a down ramp to a lower level. Finally, it was demonstrated that also applying a d.c. retarding voltage to the end-cap electrodes improves the trapping efficiency [171].

The second essential problem encountered in MALDI-ITMS experiments results from the strong dependence of the performance of the ion trap as a mass spectrometer on the total number of ions that are held inside the trap. When the ion population within the ion trap becomes too dense, then the electrical fields to which the ions are being subjected are substantially modified by the electrostatic forces associated with the trapped ions, that is, the space charge. Low levels of space charge result into slight shifts in the secular frequencies of the ions [181–183] which are observed as small shifts in the mass assignment. At higher space charge levels, also peak broadening is observed, up to levels at which the analyzer performance is seriously degraded [184]. These space charge effects are especially in the case of MALDI measurements easily encountered, because the MALDI process will generate a large excess of matrix ions in addition to the ions of interest. The most straightforward method for diminishing the ion population inside the trap is optimizing the amplitude of the rf field to satisfy $q_z > 1$ for the matrix ions and $q_z < 1$ for the analyte ions, which means that only the polymer ions will be trapped. The disadvantage of this method is (next to the previously mentioned relatively low trapping efficiency) that this amplitude does not necessarily provide optimal trapping for the ions under study. Another option is ejection of the matrix ions from the trap during or after trapping [185]. In the case of dynamic trapping in an external source geometry matrix ion discrimination is also feasible on basis of differences in flight-times [168]. During the transport to the trap, the low-mass matrix ions separate in space from the higher mass analyte ions and consequently these will arrive earlier at the trap entrance. Appropriate adjustment of the timing in ramping the amplitude of the rf trapping field should accomplish the desired discrimination.

In this chapter, we describe the design and performance of a new external ion source MALDI-ITMS instrument. No sophisticated trapping schemes were employed in the presented experiments, but the MALDI ions were injected into an active trapping field. The performance of the instrument, in particular with respect to mass dependencies in trapping efficiency and mass shifts due to space charge effects, was investigated by measuring the molecular weight distributions of low-molecular-weight synthetic polymer samples. These samples are ideal for this purpose for two reasons. The first reason is that the polymer distributions cover substantial mass ranges and mass dependencies in the trapping efficiency will therefore be reflected in distortions of the measured distributions. These distortions were quantified by comparison of the MALDI-ITMS distributions with the distributions measured by MALDI-TOF and results obtained by MALDI-FTICR-MS (described in Chapter 4 and previously published publications). On basis of these results it was possible to determine the optimal experimental conditions for measuring the molecular weight distribution of a complex block copolymer sample without significant distortions. Evaluation of the distributions in the individual block lengths demonstrated that mass discrimination effects were negligible in the copolymer measurements. The second reason is that this type of samples is demanding for the total number of trapped ions. Polymer distributions generally consist of many components. This means that the total ion signal is divided over the different components and therefore it is necessary to accumulate many ions in order to obtain an adequate signal-to-noise ratio for each component. Consequently, mass shifts induced by the total associated space charge are likely. These mass shifts were monitored in detail as a function of the total ion load on basis of deviations in the mass difference between adjacent components in a single spectrum. In the final series of measurements on a complex polymer sample it is demonstrated that carefully controlling the total space charge in the trap sufficiently minimizes these shifts. This is illustrated on basis of end group mass determinations with an accuracy of $\sim 0.1$ u from the measured spectra.

## 7.2 Experimental

### *7.2.1 MALDI-ITMS*

Figure 7.1 shows a schematic representation of the newly constructed MALDI-ITMS instrument. In this instrument, the ions are generated external to the ion trap in a home-build MALDI ion source, which is described in detail in Chapter 2. These are subsequently accelerated towards and focused onto the entrance of the ion trap using electrostatic ion optics. This ion trap (including the control electronics) was obtained from Bruker-Franzen Analytik GmbH (Bremen, Germany), and is identical to the one in the commercial Bruker Esquire instrument.

The MALDI samples were deposited on the stainless steel tip of a direct insertion probe. This probe was inserted into the external ion source via a vacuum lock. After insertion, it was in electrical contact with the source housing. The frequency-tripled output of a Quanta-Ray GCR-11 (Spectra-Physics Inc, Mt. View, California) pulsed Nd:YAG laser (producing 355 nm pulses with an energy of 60 mJ and a pulse length of 5 ns) was

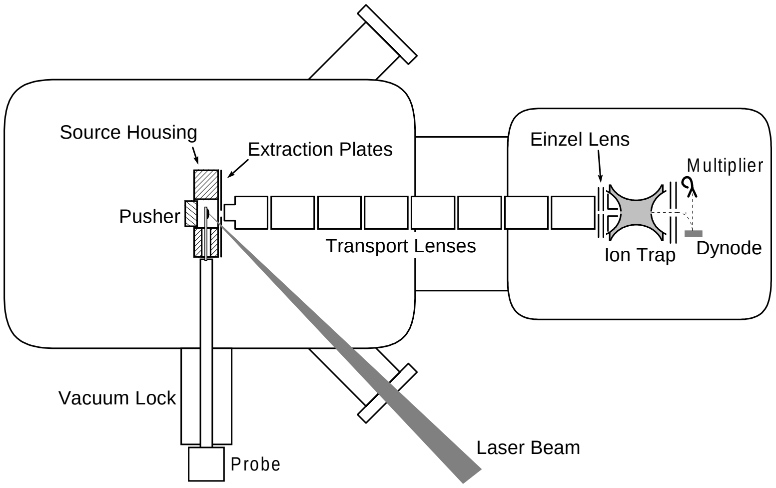

Figure 7.1: Schematic overview of the instrument for MALDI-ITMS experiments.

focused onto the MALDI probe with an incident angle of 45°. The area at the MALDI probe illuminated by the laser beam was approximately $2 \times 1$ mm$^2$ and the power density on target was measured to be maximally 100 MW/cm$^2$. The ions were created at a potential of typically 15 V and extracted from the ionization region by applying a potential difference of approximately 10 V between the source housing and the extraction plates. Subsequently, the ions were alternately accelerated and decelerated between 80 eV and 30 eV in a modified Heddle geometry, consisting of eight elements, to transport the ions over the distance of 0.2 m between the MALDI source and the ion trap. At the end of the transport lenses a set of three electrodes, operated at -40 V, -150 V, and -10 V, was installed to focus the ion beam onto the entrance of the ion trap. The ions are injected into the active trapping field of the ion trap, and He background gas was introduced into the ion trap at an estimated pressure of $10^{-3}$ mbar to realize trapping by collisional cooling of the ion kinetic energies.

At the beginning of each experiment the laser was triggered by a TTL pulse from the ion trap control electronics. A delay of typically 70 ms was installed allowing the ions to travel from the source to the cell, and to translationally cool to the center of the trap. The amplitude of the rf voltage during ion injection was determined by the value of the so-called cut-off mass $M_{\text{cut-off}}$, which corresponds to the mass of the ions that are in resonance with the dipole field at that amplitude. The relation between the amplitude and the cut-off mass in the standard operation mode is given by:

$$V_{rf} = \frac{0.2}{e} \Omega^2 r_0^2 M_{\text{cut-off}} \tag{7.1}$$

Here, $V_{rf}$, $e$, $\Omega$, and $r_0$ are the amplitude of the rf field, the elementary charge, the frequency of the rf field, and the radius of the trap (10 mm) respectively. Finally, the mass spectrum was recorded in the resonant ejection technique by scanning the amplitude of the rf voltage on the ring electrode and the phase-locked resonant ejection voltage over the two end caps. Ejected ions were accelerated over 7 kV towards a conversion dynode and the secondary electron signal was recorded by a channeltron detector operated at -1.2 kV. The entire multiplier signal as function of time was stored if only limited mass ranges were examined (see Chapter 2.3.4). Otherwise, the multiplier signal was converted in a bar graph. In that case the signal intensity is only stored for integer masses. The software packages Bruker DataAnalysis and m.a.c.s Labstar (Bruker-Franzen Analytik GmbH, Bremen, Germany) running on an IBM compatible computer under OS2 controlled the measurements and performed data acquisition and processing.

### *7.2.2 MALDI-TOF-MS*

Reference spectra of the samples used to characterize the performance of the MALDI-ITMS instrument were recorded by MALDI-TOF-MS. In this instrument, a Bruker Biflex mass spectrometer, desorption and ionization is achieved using a nitrogen laser, which produces 337 nm pulses with a pulse length of 5 ns. Samples for the MALDI experiments were deposited on a stainless steel disk containing 26 targets. After drying, this disk was transferred into the mass spectrometer via a vacuum lock. A CCD camera, connected to a video monitor, allowed visual selection and examination of the area of laser interaction with the sample. Selection of the MALDI target and positioning of the target under the desorbing laser beam were computer controlled. Optimization of the MALDI signal was achieved by varying the laser power and the position of the desorption spot. The spot size on the sample surface was approximately 50 $\mu$m in diameter. The laser beam was attenuated using a variable neutral density filter. The laser irradiance was typically optimized to be slightly above threshold. During measurements, a source pressure of $\sim 10^{-6}$ mbar at analyzer pressure of $\sim 10^{-7}$ mbar was maintained. Ions were detected in the linear mode using an accelerating voltage of 20 kV and a detector voltage of 1000 V by a MCP detector (1 GHz A/D converter). All spectra were signal averaged over 100 laser shots. All time of flight spectra were calibrated using a mixture of PEG1000, PEG2000 and PEG3000.

### *7.2.3 Sample preparation*

The poly(methyl methacrylate) (PMMA) standards were obtained from Polymer Laboratories (Amherst, MA). Four different standards were studied with an average molecular weight of 640, 1140, 1850, and 3100 u, respectively. With these standards, also a polymer blend with an extremely large polydispersity was obtained by mixing these in ratio to their number-averaged molecular weight. The polyethylene glycol (PEG) sample with average molecular weight of 1000 u was obtained from Serva (Heidelberg, Germany). Also the Jeffamine D2000 is commercially available (Texaco Chemical Company). According to the manufacturers data sheet (SC-024 102-0411), the Jeffamine D2000 is an amine-terminated polypropylene glycol with the general structure $H_2N$-($C_3H_6O$) $_n$-$C_3H_8N$. The PLURONIC L31 is a tri-block copolymer of poly(ethylene oxide) poly(propylene oxide) and was obtained from BASF (Mount Olive, NJ). The average molecular weight of the propylene oxide part was specified to be 950, and the ethylene oxide fraction of the final polymer sample was specified to be 20%. Liquitex acrylic phtalocyanine blue paint was manufactured by Lefranc & Bourgeois (Le Mans, France). The matrix in the MALDI experiments was 2,5-dihydroxybenzoic acid (DHB) from Sigma Chemical Co. (St. Louis, MO).

The polymer samples were prepared for MALDI mass spectrometry by mixing a 1-M matrix solution in ethanol with an approximately 10-g/L analyte solution in ethanol yielding a molar ratio matrix:analyte = 1000:1. For the experiments on PMMA the analyte solutions were first mixed yielding unity molar ratios. The resulting mixture was electrosprayed onto a stainless steel probe tip Chapter 3. Approximately 0.1 mL analyte/matrix is consumed during sample deposition. The acrylic paint was applied to the probe without prior sample preparation (that is, direct laser desorption instead of MALDI was performed). The total sample load on the probe was approximately 10 ng. Each sample was used to produce ions for thousands of laser shots by rotating the sample probe over $360^\circ$ and translating it over 5 mm (in this way a total area of 30 $\mathrm{mm}^2$ could be exposed to the laser spot).

## 7.3 Results

### *7.3.1 Evaluation of Mass Dependencies in the Trapping Efficiency with Broad Polymer Distributions*

Characterization of the blend of PMMA standards was realized by measuring a MALDI-TOF-MS reference spectrum. This spectrum was obtained by averaging 100 laser shots and is shown in Figure 7.2. It demonstrates that the molecular weight distribution of the PMMA blend ranges from $m/z$ 500 (corresponding to a degree of polymerization $n = 5$) to 5500 ($n = 55$). The expansion of the mass scale illustrates that predominantly sodium cationized pseudo-molecular ions are formed in the MALDI process. It further reveals that the resolution in the MALDI-TOF experiment is insufficient to distinguish between the natural occurring $^{12}$C/$^{13}$C isotopes. No further optimization of the resolution was attempted because only information on the shape of the molecular weight distribution was required. The MALDI-TOF molecular weight distribution is characterized by calculating the molecular weight averages from the spectrum in Figure 7.2. For these calculations, the measured masses were corrected for the mass of the sodium adducts and the intensities were determined by integration over the complete isotopic patterns. The calculated averages are the number-average molecular weight $M_n = \sum(N_i M_i)/\sum N_i$, where $N_i$ and $M_i$ denote the signal intensity and measured mass at peak $i$), the weight-average molecular weight $M_w = \sum(N_i M_i^2)/\sum(N_i M_i)$, the

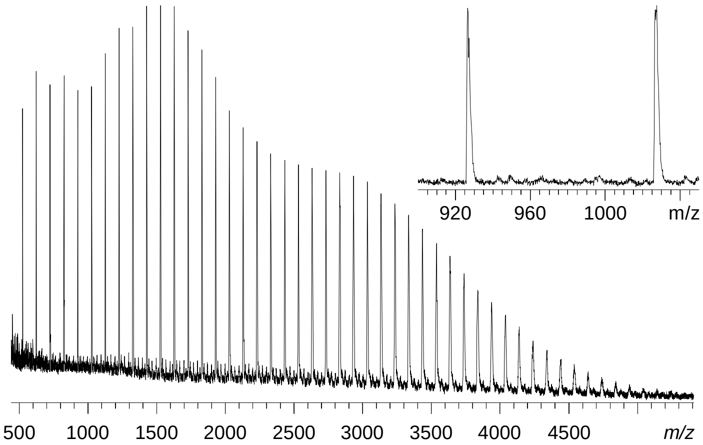

**Figure 7.2:** *Reference spectrum of the PMMA blend recorded by MALDI-TOF. The expansion of the mass scale show that primarily sodium cationized species are observed and that the resolution is insufficient to resolve the isotopic patterns.*

z-average molecular weight $M_z = \sum(N_i M_i^3)/\sum(N_i M_i^2)$, and the polydispersity index $(M_w/M_n)$. The results are listed in Table 7.1. In the following paragraphs it is assumed that these MALDI-TOF-MS results represent the true molecular weight distribution.

Next, the same sample was analyzed in the MALDI-ITMS instrument to monitor mass dependencies in the trapping efficiency of the instrument. The mass range $m/z$ 500 to 3400 was examined in the high-mass mode (as was mentioned before, $m/z$ 3400 is presently the software imposed upper mass limit of the system). In a series of experiments, the amplitude of the active rf field (that is, the value of $M_{\text{cut-off}}$) was varied because this parameter was expected to primarily determine the relationship between trapping efficiency and ion mass [174, 175]. In each experiment, spectra were recorded during 80

**Table 7.1:** *The characterizing weight averages of the PMMA blend, determined from the TOF measurement in Figure 7.2 (column 2) and from the IT measurements in Figure 7.3 for different cut-off settings (column 3-7).*

| | TOF | MALDI-ITMS | | | | |
|---|---|---|---|---|---|---|
| | | 100 u | 150 u | 200 u | 250 u | 300 u |
| $M_n$ | 2094 | 1363 | 1668 | 2106 | 2348 | 2466 |
| $M_w$ | 2644 | 1544 | 1810 | 2265 | 2486 | 2586 |
| $M_z$ | 3085 | 1720 | 1955 | 2408 | 2604 | 2688 |
| $M_w/M_z$ | 1.26 | 1.13 | 1.09 | 1.08 | 1.06 | 1.05 |

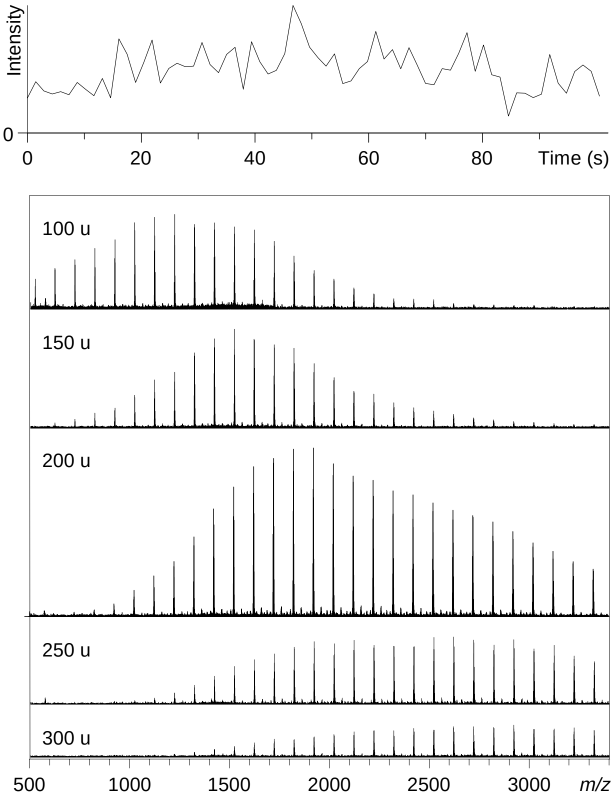

**Figure 7.3:** *MALDI-ITMS measurements of the poly(methyl metacrylate) blend. The five spectra are recorded for the different values of* $M_{\text{cut-off}}$ *indicated in the spectra. The total ion current is plotted as a function of time in the upper plot during the 80 laser shots which comprise the spectrum for* $M_{\text{cut-off}} = 100$ *u.*

successive laser shots. The resulting total ion current (TIC, the overall intensity in the individual scans as a function of time) for the experiment with $M_{\text{cut-off}} = 100$ u is presented in the upper plot in Figure 7.3. This plot shows that the MALDI-ITMS experiments are subjected to large shot-to-shot variations. The origin of these shot-to-shot variations is not likely to be in the MALDI ion source for two reasons. First, the ionizing laser beam has been tested to be stable in the course of the measurements, and second, MALDI experiments on our MALDI-FTICR-MS instrument utilizing an identical MALDI ion source did not reveal such large variations. Also the instabilities in the ion transport are not expected to be the cause, because previous experiments utilizing continuous ion beams did not reveal large temporal variations in the total ion yield. Therefore, we presently attribute the observed shot-to-shot variations to changes in the trapping efficiency due to random variations in the phase of the rf trapping field at the laser firing [179]. Elimination of the shot-to-shot variations was achieved by averaging the individual scans composing the TIC-signal, yielding the top spectrum of Figure 7.3. The other spectra in Figure 7.3 were similarly obtained with $M_{\text{cut-off}}$ = 150, 200, 250, and 300 u, respectively. Experiments performed with $M_{\text{cut-off}}$ smaller than 100 u or larger than 300 u were observed to give no significant signals. It is immediately seen from this set of spectra that the shape of the measured molecular weight distribution, and thus the mass range of efficient trapping, is strongly dependent on the setting for $M_{\text{cut-off}}$. However, experiments on the individual PMMA standards in the same mass range (data not shown) proved that the (mass dependence of the) trapping efficiency is not solely determined by the amplitude of the rf field. For example, comparison of the spectra in Figure 7.2 and Figure 7.3 suggests that the high-mass measuring mode is not suitable for masses smaller than $m/z \sim 1000$, whereas experiments on the PMMA standard with an average molecular weight of 640 u ($M_{\text{cut-off}}$=50-100 u) yielded relatively much higher intensities in the lower mass range. Moreover, an experiment (with $M_{\text{cut-off}}$=150 u) in which the PMMA oligomer at $m/z$ 625 was isolated after trapping and prior to the ejection scan yielded significantly higher intensities for this oligomer (data not shown). A similar effect was not observed for the higher mass end of the distribution. The total space charge apparently causes lower mass ions to be inefficiently ejected during the ejection scan or to become unstable prior to the ejection scan.

The distortions in the observed molecular weight distributions induced by the mass dependent trapping efficiency are nicely reflected by the characterizing weight averages. These have been calculated for the individual spectra in Figure 7.3 and are included in Table 7.3. As expected from the measured spectra, the weight averages increase for increasing $M_{\text{cut-off}}$. In a rough approach, the number-average molecular weights are indicative for the center of the mass range in which optimal trapping occurs at a given setting of $M_{\text{cut-off}}$. Unfortunately, the exact relationship between the trapping efficiency (as a function of mass) and $M_{\text{cut-off}}$ can not be obtained. This is caused by the mass discrimination effects due to space charge, which can not be recovered from the present measurements. The observed decrease of the polydispersity index for increasing $M_{\text{cut-off}}$ is mainly the result of the upper mass limit of $m/z$ 3400 in the MALDI-ITMS experiments. After all, the spectra in Figure 7.3 suggest that for $M_{\text{cut-off}} \geq 200$ u components with $m/z > 3400$ would be detected if the upper limit could be extended to $m/z$ 5000, which would lead to higher values of the polydispersity factor.

### 7.3.2 Characterization of the Trapping Efficiency

It follows from the previous experiments that, in order to characterize the trapping efficiency as a function of mass for different amplitudes of the active rf field, it is necessary to minimize mass discrimination due to space charge. This was accomplished by evaluating the PMMA standard with an average molecular weight of 640 u for different values of $M_{\text{cut-off}}$ and comparing the results with a MALDI-TOF-MS reference spectrum. The

MALDI-TOF-MS reference spectrum is plotted in Figure 7.4 A and shows the entire distribution, ranging from $m/z$ 425 to 1525 ($n = 4 - 15$) with a maximum at $m/z$ 725. It is seen that the PMMA640 sample has a much more moderate polydispersity index in comparison to the PMMA blend, which means that the number of trapped ions can be kept much lower. The MALDI-ITMS experiments were performed in the standard mass range for $M_{\text{cut-off}}$ ranging from 50 u to 180 u in steps of 10 u. The individual spectra were averaged over 25 laser shots. As an example, the MALDI-ITMS spectrum recorded with $M_{\text{cut-off}}$ =60 u is shown in Figure 7.4 B. This reveals again a severe distortion in the mass distribution recorded by the MALDI-ITMS instrument. The trapping efficiency was determined as a function of mass and $M_{\text{cut-off}}$ by dividing the relative intensities in the series of MALDI-ITMS spectra by those in the MALDI-TOFMS spectrum:

$$P(M_i, M_{\text{cut-off}}) = \frac{I_i^{\text{ITMS}}}{I_i^{\text{TOF}}} \tag{7.2}$$

Here, $I_i^{\text{ITMS}}$ and $I_i^{\text{TOF}}$ are the intensity of the polymer component measured by MALDI-ITMS and the intensity of the same polymer component measured by MALDI-TOF, respectively, at mass $M_i$, and $P$ is the trapping efficiency. The results are visualized as a function of $M_{\text{cut-off}}$ in the 3D plot in Figure 7.4 C. The 3D plot suggests that for $M_{\text{cut-off}}$ $>$ 90 u the trapping efficiency becomes fairly constant over considerable mass ranges. For example, at $M_{\text{cut-off}}$ = 120u the PMMA distribution measured by MALDI-ITMS was almost identical to the one measured by MALDI-TOF-MS in the mass range $m/z$ 600 to 1200.

This ”flatness” of the detection efficiency curve was examined in more detail by evaluating the distributions in the individual components of the PLURONIC L31 block copolymer, which was previously characterized with MALDI-FTICR-MS (Chapter 4). The FTICR-MS results demonstrated that the PLURONIC copolymer follows the random coupling hypothesis, i.e., no correlation exists between the lengths of the different constituents. A correlation between these lengths in the ITMS results would therefore be a strong indication for mass discrimination effects which distort the measured molecular weight distribution. The PLURONIC copolymers are fabricated by first synthesizing a poly(propylene oxide) polymer and subsequently adding ethylene oxide units to both sides of the initial poly(propylene oxide) polymers which yields a distribution of triblock polymers of the type HO - $(C_2H_4O)_X$ - $(C_3H_6O)_Y$ - $(C_2H_4O)_Z$-H. Figure 7.5 shows the MALDI-ITMS spectrum. In order to obtain this spectrum, two experiments were performed over the mass ranges $m/z$ 500-1300 and $m/z$ 1100-1900, respectively, in which 50 laser shots were averaged in the standard mass mode with $M_{\text{cut-off}}$ =70 u. In this way it was possible to store the complete multiplier signal as a function of time and thus to preserve peak information. The overall spectrum was reconstructed by overlaying the two individual spectra. The mass range shown covers the entire molecular weight distribution. Spiking the samples with sodium, potassium, and lithium salts verified that only sodium adduct ions are present in the spectrum. The most dominant ion series was identified as the distribution of the poly(propylene oxide) homopolymers. The composition of the

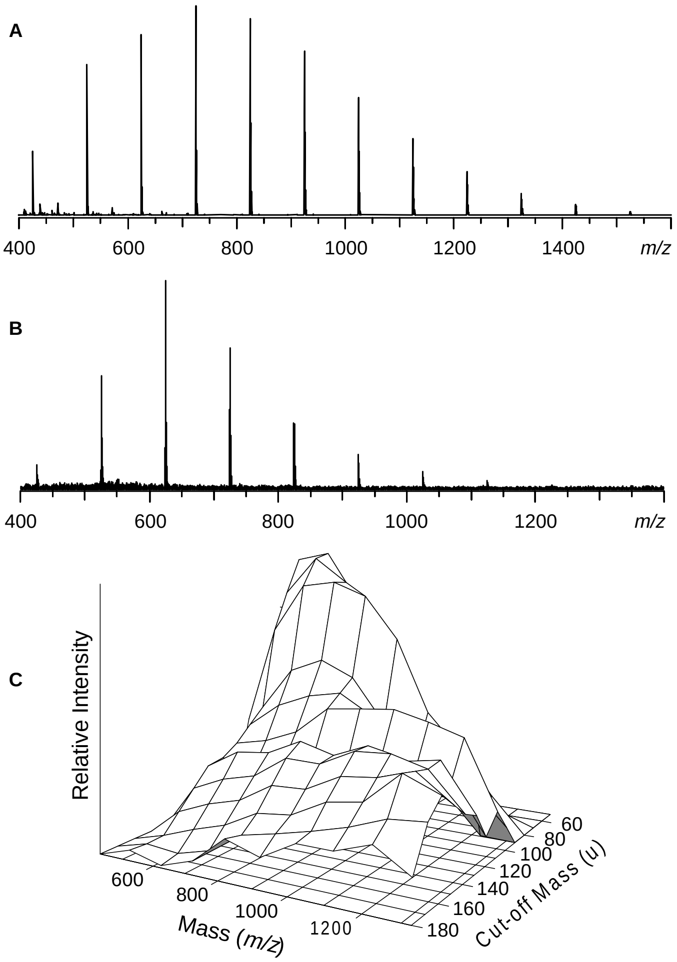

**Figure 7.4:** *Molecular weight distribution of PMMA 640 recorded by MALDI-TOF (A), by MALDI-ITMS with $M_{\text{cut-off}}$ =60 u (B), and by MALDI-ITMS as a function of the value of $M_{\text{cut-off}}$ (C).*

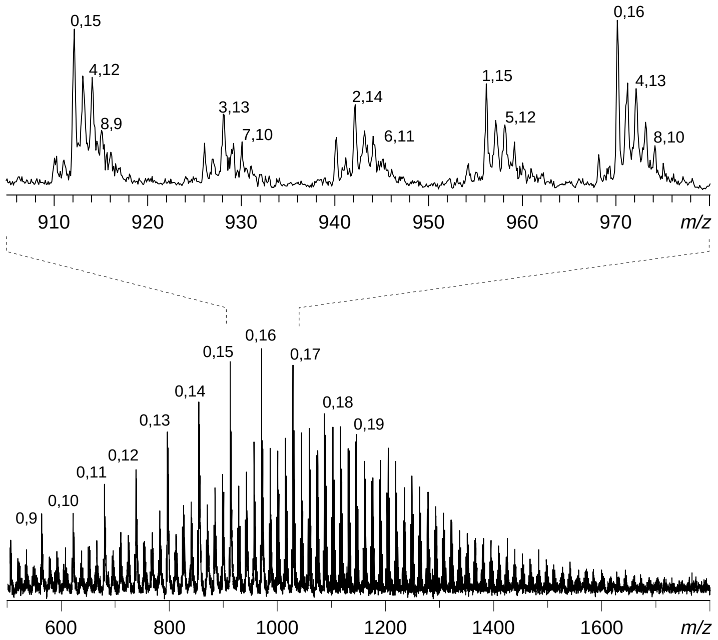

**Figure 7.5:** *MALDI-ITMS spectrum of Pluronic L31. For this measurement,* $M_{\text{cut-off}}$ *was optimized to minimize mass discrimination over the mass range covered by the molecular weight distribution. The series of poly(propylene glycol) homopolymers is indicated (the first number refers to* $n^{EO}$*, the second number to* $n^{PO}$*). In the expanded mass scale the composition of all monoisotopic copolymers is indicated.*

copolymer molecules is indicated for the series of poly(propylene glycol) homopolymers in the spectrum, and in the expanded mass scale for all monoisotopic peaks. Here the first number refers to the number of ethylene oxide units present in the copolymer ($n^{\text{EO}}$) and the second number refers to the number of propylene oxide units present ($n^{\text{PO}}$). In this way we have identified all the components with S/N>2, yielding 210 peak intensities with their corresponding copolymer compositions.

Before evaluating the individual block length distributions two effects have to be considered. Firstly, it can be seen from the expanded mass scale that no distinction can be made between the second isotopic peak of the homopolymer with $n^{\text{EO}}$=0 and $n^{\text{EO}}$=16 (monoisotopic peak at $m/z$ 969.6) and the monoisotopic peak of the copolymer with $n^{\text{EO}}$=4 and $n^{\text{EO}}$=13 at $m/z$ 971.6. Secondly, it is evident that taking the intensity of monoisotopic peaks to be representative for the relative abundance of the corresponding component will introduce errors as the relative abundance of the monoisotopic peak will significantly vary over the mass range under study. In Chapter 4 we have dealt with these problems and proposed a correction method to reveal the actual relative abundances.

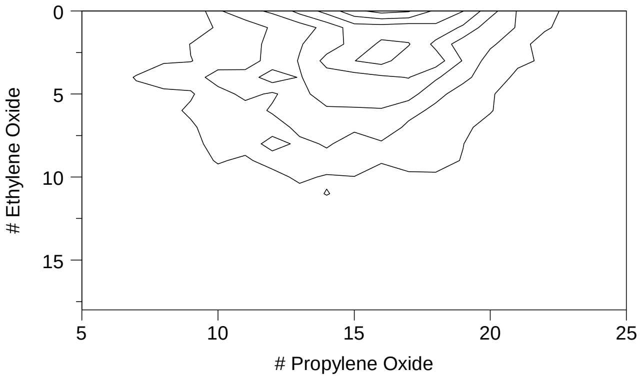

**Figure 7.6:** *Contour map of the distribution of monomeric units as a function of the individual monomeric units in the polymer. The data plotted are extracted from the spectrum in Figure 7.5.*

After applying this correction method to the data obtained from Figure 7.5, the corrected peak intensities are plotted as a function of $n^{\mathrm{EO}}$ and $n^{\mathrm{PO}}$ in Figure 7.6. The contour plot reveals that the distribution in the propylene oxide block remains approximately constant for the different total lengths of the ethylene oxide blocks. This result demonstrates that our MALDI-ITMS instrument can be optimized to have a constant trapping efficiency in the mass range $m/z$ 500 to 1500.

### *7.3.3 Mass Shifts Induced by Space Charge*

The dependence of the measured mass upon the signal intensity has been investigated for a phtalocyanine blue pigment in a series of measurements on the acrylic paint sample. For these experiments the complex paint formulation was applied directly to the probe, that is, direct Laser Desorption and Ionization (LDI) was employed instead of MALDI. Spectra were recorded for single laser shots in the high-resolution mode with $M_{\text{cut-off}}$ =100 u over the mass range $m/z$ 400 to 700. Variations in the intensity of the molecular ion were induced by changes in the attenuation of the laser beam at the one hand, and by the statistical shot-to-shot variations in the MALDI-ITMS experiments at the other hand. The intensity of the molecular ion cluster was determined by integration of the ion signal over the mass range $m/z$ 574 to 580. The monoisotopic peak of the molecular ion cluster was fitted with the Gauss function

$$I_{\text{meas}} = A \cdot \exp\left(-\frac{(m_{\text{meas}} - m_c)^2}{w^2}\right) \tag{7.3}$$

where $I_{\text{meas}}$ was the measured intensity at mass $m_{\text{meas}}$. The fit result for the peak center $m_c$ was taken as the measured mass of the pigment. The fit results for the peak height $(A)$

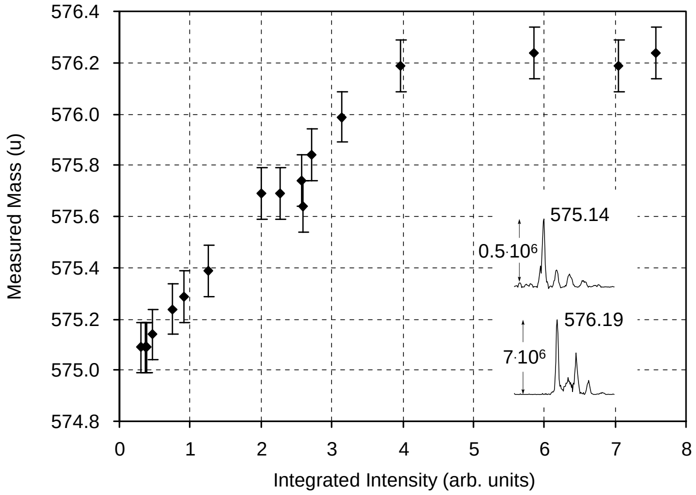

**Figure 7.7:** *Mass of the phtalocyanine blue pigment measured by LDI-ITMS as a function of the intensity of the molecular ion (determined by integration over the entire isotopic pattern).*

and the peak width ($w$) were not evaluated. The results are plotted in Figure 7.7. The plot indicates that a linear relationship exists between the measured mass and the molecular ion intensity for intensities lower than $4{\cdot}10^6$ cps. The total mass shift over the complete set of measurements is expounded by the inset in Figure 7.7. This inset shows the measured isotopic pattern for an integrated intensity of $0.5 \cdot 10^6$ cps (upper spectrum) and $7 \cdot 10^6$ cps (lower spectrum), respectively, revealing the total shift of $\sim$1.1 u. Note that the isotopic pattern is severely distorted in the lower spectrum. Inspection of the individual spectra revealed that this is the case for integrated intensities larger than $\sim 1.5 \cdot 10^6$ cps. The increase in the measured mass for an increasing ion load can be explained by recalling that the mass axis (y-axis) can be regarded as a time-of-ejection axis, whereas the intensity of the molecular ion (x-axis) can be regarded as the total number of ions present inside the trap. It is evident that the space charge associated to the ion cloud inside the trap slightly shields the electrical field induced by the rf voltage on the ring electrode. This shielding increases for increasing numbers of ions, inducing a decrease of the effective electrical field strength. As a result of the decreased effective electrical field, the secular motion of ions with a particular $m/z$ will get in resonance with the alternating dipole field across the end caps at higher rf voltages, and thus will be ejected and detected at later times (that is, at higher masses). The asymptotic behavior of the plot for intensities larger than $4 \cdot 10^6$ cps is presently not fully understood. Future experiments in combination with ion trajectory calculations are planned for further investigation of this effect.

After the previous results, which only concerned ions of one specific mass, it is interesting to investigate shifts in the measured mass of a particular ion induced by the presence of ions at other masses. This was studied by measuring the distribution of the poly(ethylene glycol) sample. Mass spectra were produced by averaging 25 spectra from individual scans in the extended mass range with $M_{\text{cut-off}}$ = 90 u, covering the molecular weight distribution in the mass range $m/z$ 745 to 1362 (corresponding to a degree of polymerisation of 16 and 30 respectively). First, the distribution was measured with the laser intensity just above threshold, which implies that mass shifts are minimal. The instrument was calibrated on basis of this measured distribution. Next, a spectrum was taken at a much higher laser intensity. The influence of the total ion load on the measured mass was evaluated by plotting the difference between the mass determined from the spectrum and the calculated mass as a function of the number of ions trapped at the time of ejection for each monoisotopic peak in the spectrum. The latter quantity was assumed to be proportional to the integration of the ion signal starting two mass units lower than the mass of the ejected ions up to the upper limit of the mass scan. The result is plotted in Figure 7.8. The corresponding high-intensity MALDI-ITMS spectrum is shown in the inset in Figure 7.8. It should be noted that $M_{\text{cut-off}}$ was optimized for optimal signal-to-noise and no attempt was made to produce a molecular weight distribution close to the expected one. The linear dependence between the mass shift and the integrated intensity demonstrates

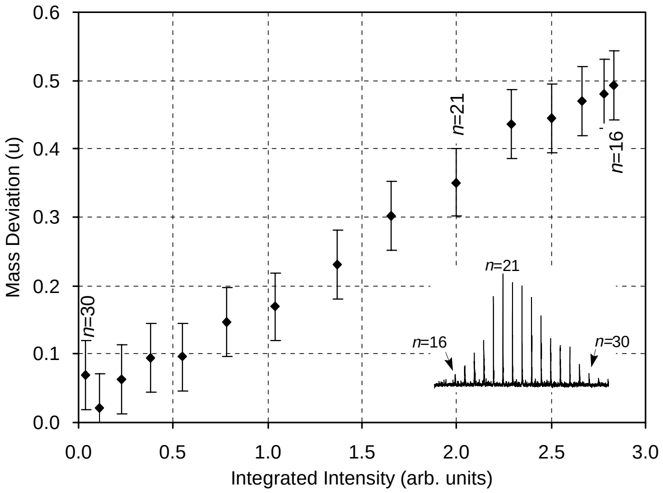

**Figure 7.8:** *Mass deviations as a function of the integrated intensity for a PEG1000 sample measured by MALDI-ITMS. The mass deviation is defined as the difference between the measured mass of a particular component of the molecular weight distribution and its actual mass. The corresponding integrated intensity is determined by integration of the mass spectrum over the mass range starting at (and including) this particular component up to the upper limit of the measured mass range. This quantity is assumed to be proportional to the magnitude of the trapped ion population at the time of its ejection.*

that shifts in the measurement of an ions mass are entirely determined by the magnitude of the total space charge at the time of ejection. An important consequence of this result is that the number of trapped ions does not change the calibration function by a constant offset. Instead, the change depends on both the masses as well as the intensities of all trapped ions, resulting in a complex calibration function which is hard to predict.

It is obvious that mass shifts complicate the mass measurements. A challenging test for the possibilities of MALDI-ITMS with respect to accurate mass measurements is the determination of the polymer end groups in a complex polypropylene sample. According to the specifications of the manufacturer, the Jeffamine D2000 sample consists of a series of amine terminated polypropylene glycols and an average molecular weight of 2000 u. As was mentioned before, the present set-up only allows to acquire scan spectra in standard mass mode over mass ranges smaller than 800 u. In order to preserve information on single isotopic peaks, experiments were performed in the standard mass mode with $M_{\text{cut-off}}$ =70 u over three different mass ranges, namely $m/z$ 500-1300, $m/z$ 1100-1900, and $m/z$ 1700-2500 respectively. In this way the complete molecular weight distribution of the Jeffamine sample could be analyzed. The laser intensity was optimized to be just above threshold. Spectra of 50 individual scans were summed for each of the three mass ranges. First, these settings were used to record spectra of the PMMA1140 standard (data not shown) for calibration of the instrument. The results of the experiments on the Jeffamine sample are combined in Figure 7.9 to reconstruct the complete molecular weight distribution. It is seen that the molecular weight distribution in the mass range $m/z$ 500-2500 is bimodal, pointing to contamination with other polymers, early termination reactions during polymerization, or oxidation. The expansion of the mass scale reveals that the resolution $(m/\mathrm{d}m)_{50\%}$ of 2500 at $m/z$ 1722 is sufficient to resolve the naturally occurring $^{12}$C/$^{13}$C isotopes of the component molecules. Only sodium adduct ions are

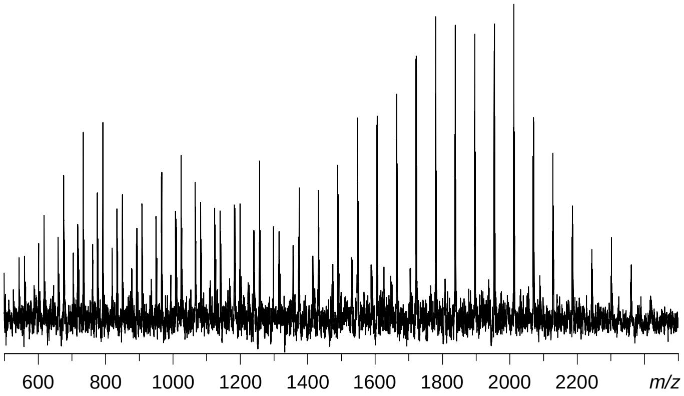

**Figure 7.9:** *MALDI-ITMS spectrum of Jeffamine D2000. The value of $M_{\text{cut-off}}$ was optimized for optimal signal-to-noise at the lower mass end of the molecular weight distribution.*

present in the spectrum, as was again verified by spiking the samples with sodium and potassium salts. The distribution was characterized by calculating the molecular weight averages and the polydispersity index from the intensities of all monoisotopic peaks in the spectrum. The results are presented in Table 7.2, which also lists the results of previous analyses on the same sample by MALDI-FTICR-MS [112]. It is seen that the average molecular weights obtained from the ITMS data are structurally lower than those obtained from the FTICR-MS data. This results from an optimization of the value for $M_{\text{cut-off}}$ for especially the lower mass range (there signal intensities are lower). Consequently, masses above $m/z$ 1600 were slightly discriminated which causes an underestimation of the average molecular weights.

**Table 7.2:** *$M_n$, $M_w$, $M_z$, $M_p$, and $M_w/M_n$ values calculated from the molecular weight distributions of Jeffamine D2000 measured by MALDI-FTICR-MS [112] and MALDI-ITMS (Figure 7.9).*

| | MALDI-FTICR-MS | MALDI-ITMS | | | |
|---|---|---|---|---|---|
| | Complete MWD | Complete MWD | $C_3H_8N$ | $C_3H_5$ | $C_3H_5O$ |
| $M_n$ | 1559 | 1347 | 1785 | 997 | 912 |
| $M_w$ | 1746 | 1517 | 1817 | 1062 | 958 |
| $M_z$ | 1779 | 1653 | 1847 | 1119 | 1002 |
| $M_p$ | 1779 | 1779 | 1779 | 1067 | 793 |
| $M_w/M_n$ | 1.12 | 1.13 | 1.02 | 1.07 | 1.05 |

End group analysis (Chapter 3) of the mass spectrum of the Jeffamine D2000 spectrum demonstrated that there are at least three different series of peaks at equidistant intervals of 58 u present in the molecular weight distribution of Jeffamine D2000. The masses of the end groups $M_{\text{end, meas}}$ were calculated by subtracting the mass of the cationizing species and the product of the degree of polymerization and the mass of the repeating unit from the measured masses for each component in the molecular weight distribution. Subsequently, these values were averaged for the three series of peaks. The results are presented in Table 7.3, along with a proposal for the elemental composition of the end groups, the corresponding calculated masses of the end groups $M_{\text{end, calc}}$, and the differences between the measured and calculated end group masses $\Delta M_{\text{end}}$. In addition, the characterizing molecular weights were calculated for the individual series, which are included in Table 7.2. The results in Table 7.3 show that the dominant distribution in Figure 7.9 consists of the amine terminated polypropylene glycols of the type $[H_2N\text{-}(C_3H_6O)_n\text{-}C_3H_8N + Na]^+$, as specified by the manufacturer. The molecular weight distribution of this series ranges from $m/z$ 1316 ($n$=21) to $m/z$ 2303 ($n$=38) and exhibits an $M_p$ of $m/z$ 1779. The second prominent ion series is observed in the low molecular weight part of the spectrum, ranging from $m/z$ 544 to 1473, and with an $M_p$ of $m/z$ 1067. End group analysis on this series yielded 57.26, which corresponds to the sum of the masses of $C_3H_5$

**Table 7.3:** *Masses and deviations in the end group analysis of Jeffamine D2000 by MALDI-ITMS.*

| | $M_{\text{end, calc}}$ | $M_{\text{end, meas}}$ | $\Delta M_{\text{end}}$ |
|---|---|---|---|
| $H_2N\text{-}(C_3H_6O)_n\text{-}C_3H_8N$ | 74.08 | 73.96 | -0.12 |
| $H_2N\text{-}(C_3H_6O)_n\text{-}C_3H_5$ | 57.06 | 57.01 | -0.05 |
| $H_2N\text{-}(C_3H_6O)_n\text{-}C_3H_5O$ | 73.05 | 73.02 | -0.03 |

and $NH_2$ (Table 7.3). Such unsaturated structures are well known for poly-ethers, and may result from dehydration of terminal hydroxyl groups during polymerization. This would point to early termination of the polymerization process, and thus explain the relatively low average molecular weight numbers of this series (Table 7.2). The last ion series is observed in the molecular weight range from $m/z$ 560 to 1315 and exhibits a $M_p$ of $m/z$ 793. The mass of the corresponding end group was determined to be 73.25, which is in agreement with the sum of the masses of $C_3H_5O$ and $NH_2$. This would indicate that for example oxidation processes have induced ketone or aldehyde functions in the polymer. In the MALDI-FTICR-MS experiments an additional ion series with an end group mass corresponding to the sum of the masses of H and $NH_2$ was observed. This ion series has not been recovered in the present investigation, as the resolution of the MALDI-ITMS experiment is not sufficient to resolve it from the naturally occurring $^{13}C$ isotopes of the $[H_2N\text{-}(C_3H_6O)_n\text{-}C_3H_5O + Na]^+$ series.

It can be concluded that the results of the end group analysis are in good agreement with those obtained from the previous MALDI-FTICR-MS experiments, which demonstrates that mass accuracies better than 0.3 u can be achieved by optimizing the laser intensity just above threshold.

## 7.4 Discussion and Conclusions

The presented results clearly reveal that external ion source MALDI-ITMS experiments are easily complicated by mass discriminations and shifts in the mass determination. Mass discriminations are attributed to mass dependencies in the trapping efficiency because the amplitude of the rf field during injection highly determines the mass range of efficient trapping. Nevertheless, the instrument can be optimized to properly analyze samples with narrow mass distributions in a single experiment. This was demonstrated with the experimental confirmation of the random coupling hypothesis for the PLURONIC copolymer. On basis of the measurements of the PMMA blend it is expected that this generally holds for mass ranges smaller than $\sim$1000 u up to at least $m/z$ 3400. Analyses of systems that are more polydisperse are highly affected by mass discriminations. Possible experimental strategies for such samples are correction of the measured spectra for the mass discrimination or recording a series of spectra in which successive mass intervals of 1000 u are optimized for minimal mass discrimination. Of course, these remarks assume that additional mass discriminations due to space charge can be avoided.

The shifts in the mass determination result from variations in the total space charge. It was demonstrated that these can effectively be minimized by minimizing the number of trapped ions. At larger ion signals, mass shifts can be kept within reasonable limits if the shape of the isotopic patterns is evaluated. It was shown that these become substantially distorted when a mass shift of approximately 0.3 u is observed (see Figure 7.7). This is however only true if the sample contains a few different components. Calibrant spectra have to be recorded to characterize the mass shifts for the actual experimental conditions if many different components are present in the ion population. This can be used to estimate the space charge induced mass shifts for the individual components on basis of shift versus ion intensity graphs (similar to Figure 7.8) as a correction of the measured masses.

# 8

# A Novel Instrument for Spatially Resolved Surface Analysis with Laser Desorption Quadrupole Ion Trap Mass Spectrometry

*A new instrument for Laser Microprobe Mass Spectrometry with a quadrupole Ion Trap Mass Spectrometer is described. The instrument is designed to achieve a spatial resolution of 10 $\mu$m. Analytical data on preliminary measurements of the distribution of pigments in a paint cross section are presented. These demonstrate a spatial resolution of approximately 25 $\mu$m. Also the possibility to perform spatially resolved structural studies by utilization of MS$^n$ experiments is shown.*

## 8.1 Introduction

A large number of commonly used and fullgrown techniques is available for the spatially resolved analysis of surfaces. For example, techniques as Atomic Force Microscopy (AFM) and Scanning Tunneling Microscopy (STM) lead to detailed information on the surface morphology. Various forms of electron spectroscopy are available if instead information is required on the identity of the elemental composition of the surface. For example, Auger Electron Spectroscopy (AES) and Xray Photoelectron Spectroscopy (XPS) are widely used techniques in this field. Surface information on a more molecular level is provided by techniques as Raman and Fourier Transform Infra-Red (FTIR) spectroscopy, because also the presence of specific functional groups in the surface molecules can be detected. However, the only analytical method that provides information on the composition and the structure of large organic molecules is mass spectrometry.

The first step in the examination of solid surfaces by mass spectrometry is the conversion of solid matter into gas phase ions. This conversion can be problematic if knowledge on the masses of the intact molecules is desired, because then the energy deposited into the molecules has to be minimized to prevent decomposition. This is even worse if the surfaces consist of large polar, nonvolatile or thermally labile substances. During the past two decades, various so-called ”soft” ionization techniques have been developed to address this problematic conversion step (Chapter 1). Of these techniques, laser desorption is the most promising ionization technique for the study of organic compounds. The spatially resolved version of laser desorption MS, which has become known as ”laser microprobe mass spectrometry” (LMMS), has proven to be very successful in characterizing both the organic and the inorganic constituents at the surface of a broad range of samples [10–14].

The pulsed nature of the ion production in the LMMS technique makes it a natural partner for a mass analyzer which is also operating in a pulsed manner, such as Time-of-Flight (TOF), Fourier Transform Ion Cyclotron Resonance (FTICR), and quadrupole Ion Trap (IT) mass spectrometers. Especially TOF mass spectrometers are widely used in LMMS instruments, as these are relatively inexpensive and easy to couple to laser desorption techniques. These systems provide a large mass range over which the samples can be analyzed and a high sensitivity. If the mass resolution and mass accuracy of the TOF-MS instruments are insufficient or multistage mass spectrometry experiments (MS$^n$) are required to fully characterize the samples, it is preferable to couple the laser microprobe technique to FTICR-MS instruments. Concessions with respect to the sensitivity provided by TOF instruments are however unavoidable. A rather unexplored area is the use of quadrupole ion traps in LMMS instruments. Laser desorption experiments in ions traps have demonstrated that this combination is very attractive as the IT-MS combines MS$^n$ possibilities with high sensitivity.

This chapter deals with the development of a new ion source for specially resolved laser desorption experiments with FTICR-MS and ITMS. The design of the ion source and the hardware and software for sample manipulation are described in detail. Results of preliminary experiments with the ion source coupled to the ITMS instrument are presented to illustrate its performance.

## 8.2 Instrument Description

The design of the novel LMMS instrument is based on the following criteria:

- The spatial resolution in the LMMS analyses must be better than 15 $\mu$m.
- Spatial resolution is to be achieved by focusing laser beams to a spot size of approximately 15 $\mu$m on the sample surface for localized desorption.
- The laser and sample viewing optics are fixed and situated entirely outside the vacuum system.
- Samples are micropositioned inside the vacuum system in order to specify the desorption area.
- Desorbed neutrals should be post-ionized by electron impact ionization (EI) or photon ionization (PI) to obtain maximum ion yields.

- The ions are analyzed according to their mass in a quadrupole ion trap mass spectrometer in order to ensure high detection sensitivity in combination with the possibility of high-efficiency tandem mass spectrometry experiments.
- The hardware required for spatially resolved laser desorption experiments must be compatible with the existing FTICR-MS instrument in case of ultra-high resolution LMMS experiments in the future.

Figure 8.1 shows a schematic representation of the instrument that was build on basis of these criteria. To summarize the operating principles briefly, a sample that is mounted on a sample holder is introduced into the vacuum system via the sample exchange chamber and placed on the sample table. After pumping down the manipulator and the sample exchange chamber, the separation valve is opened and the sample is transported to the ion source by the manipulator. There, it is micropositioned underneath a small ionization chamber in the focus of the laser beam to select the desorption area. This selection process is aided by visual images, which are recorded by a video camera mounted on the long distance microscope and captured by in-house developed software that controls the manipulator. Four different types of laser light are available for desorption. A diode pumped Nd:YAG laser delivers cw laser light at 1064 nm, whereas a Q-switched Nd:YAG laser produces short, intense pulses of light at 1064 nm, which can be frequency doubled or tripled if desirable. The same optics are used to focus either of these laser beams on the sample surface. The laser light is coupled into the line of view of the microscope with a dichroic laser mirror, which reflects only light at the laser's operating wavelength. Upon

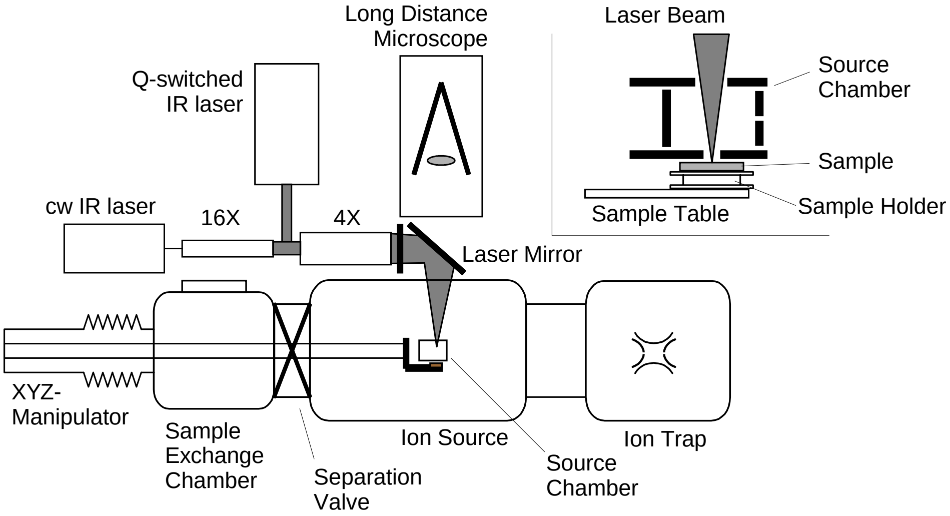

**Figure 8.1:** *Schematic representation of the novel LMMS instrument. The inset shows an expanded view of a sample that is micropositioned underneath the source chamber.*

desorption, surface material is converted into gaseous neutrals and ions. The neutrals expand into a small ionization chamber, where they are post-ionized by electron impact or photo ionization. The ions are extracted orthogonal to the desorption plume and then transferred from the external source into the ITMS with an electrostatic ion optical system.

In this instrument, the ITMS (including electronics and data acquisition software) and the XYZ-manipulator are commercially available and were obtained from Bruker-Franzen Analytik GmbH (Bremen, Germany) and VG instruments (Fisons Instruments Vacuum Generators, East Sussex, England), respectively. The remaining components were designed and/or constructed in-house and are described in more detail in the following subsections.

### *8.2.1 Vacuum System*

It can be seen in Figure 8.1 that the vacuum system consists of four sections: the XYZ-manipulator, the sample exchange chamber, the ion source region, and the ITMS. The sample exchange chamber is pumped by a Balzers 56 $l/s$ turbo molecular pump and the ion source region by a Balzers 520 $l/s$ turbo molecular pump, both backed by oil-free membrane pumps. A separation valve is installed, which allows the venting of the sample exchange chamber and the XYZ-manipulator without braking vacuum in the source and ITMS regions. The base pressure in the ion source region is $10^{-7}$ mbar (with closed separation valve and no Helium introduction). Helium is introduced into the ion trap to a level that increases the pressure in the ion source to typically $2 \times 10^{-6}$ mbar. After venting the sample exchange chamber, it is pumped down in approximately half an hour to a pressure $< 1 \times 10^{-5}$ mbar before the separation valve is opened. During operation, the pressure in the ion source is typically $4 \times 10^{-6}$ mbar.

### *8.2.2 Ion Source and Ion Optics*

A top view of the ion source is schematically shown in Figure 8.2. The core of the ion source is the source chamber, which consists of a source housing (internal dimensions $2 \times 2 \times 4.5$ cm$^3$), a movable pusher electrode and an extraction electrode. Holes in the top and bottom of the source housing of 5 mm and 4 mm diameter, respectively, allow the focussing of the laser light onto the sample surface that is located typically 1 mm underneath the source chamber (see also the inset in Figure 8.1). In the configuration depicted in Figure 8.2, neutrals that expand into the source chamber via the bottom hole are subjected to electron bombardment for post-ionization. These electrons are emitted by the filament that is mounted on the side of the source housing and are accelerated by a potential difference of 1-100 V between the filament and the source housing. This causes the electrons to move along the magnetic field lines between the two permanent magnets towards the collector at the other side of the source housing, and thus to cross the desorption plume. The complete assembly for the electron beam can be removed easily. This allows to direct a laser beam through the desorption plume for photo-ionization.

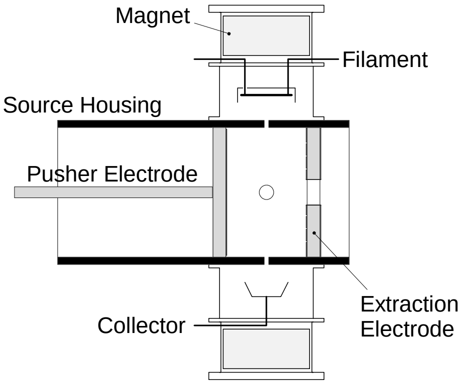

**Figure 8.2:** *Schematic overview of the ion source for spatially resolved laser desorption and the specially shaped extraction electrodes.*

The repeller electrode consists of a thin layer of CrN that is deposited on a 2 mm thick plate of macor. The extraction electrode consists of a pair of such plates. However, the CrN layers on these plates were milled to yield specially shaped patterns, as is depicted in Figure 8.3 A. These plates were connected together to obtain the electrode structure that is shown in Figure 8.3 B. Three voltages are applied to this electrode assembly: the left-hand side extraction voltage EL, the right-hand side extraction voltage ER, and the voltage that is applied to the source housing. Resistors are placed in between the two electrode plates to connect the different CrN segments with these external voltages according to the scheme that is shown in Figure 8.3 C. This causes the voltage on the CrN segments to change gradually from the extraction voltage (which is the average of EL and ER) to the source housing potential, as is illustrated in Figure 8.3 D. SIMION ion trajectory calculations [186] indicate that this arrangement provides a hundred percent efficient extraction field for ions that are created around the center of the source chamber. Additionally, these numerical simulations show that optimization of the source potentials allows the efficient extraction primary ions that are produced by the laser desorption process at the sample surface.

Extracted ions are transported to the ion trap by the ion optical system that was already presented in Figure 7.1 of Chapter 7. In this system, a set of eight cylindrical electrodes is used to alternately accelerate and decelerate the ions between typically 80 eV and 30 eV. A set of three plate electrodes (typically operated at -40 V, -150 V, and -10 V, respectively) is installed at the end of these transport electrodes to focus the ions onto the entrance of the ion trap. This system was designed with the aid of ion trajectory calculations using the SIMION computer program. The results of the numerical simulations indicate a high transport efficiency for low kinetic energy ions ($< 30$ eV).

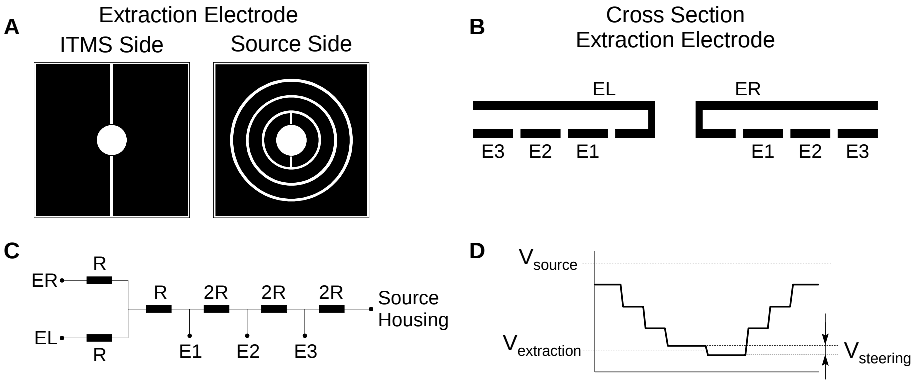

**Figure 8.3:** *Specially shaped extraction electrode for an optimal extraction field. Shown are the milled patterns in the CrN layers of the component plates that face the source and ITMS, respectively (A), a cross section of the extraction electrode assembly (B), the wiring scheme that connects the different CrN segments, the voltage applied to the source housing and the externally applied extraction voltages EL and ER (C), and the voltage scheme near the source side plate (D).*

### *8.2.3 Sample Viewing System and Laser Optics*

Sample viewing during desorption experiments is provided by a Leica (Heerbrugg, Switzerland) MZ12 microscope equipped with a Donpisha XC-003P color video camera (fabricated by Sony, Japan). This system attains a maximum magnification of $220\times$ at a working distance of 190 mm. The output of a cold-light source is coupled into the vacuum system for sample illumination with a 10 mm diameter flexible fiber optic light guide that is sealed in a stainless steel tube.

Laser light is produced by two different Nd:YAG lasers. A diode pumped Nd:YAG laser (Adlas DY301 Q DII, Adlas GmbH & Co. KG, Lübeck, Germany) delivers laser light of 0.6 mm beam diameter at 1064 nm. In the cw mode, the output power is adjustable between 0 and 200 mW. Alternatively, a Q-switch mode is available, in which it produces pulses of laser light of minimally 13 ns length and maximally 7 $\mu$J pulse energy. The second laser is a Quanta-Ray GCR-11 pulsed Nd:YAG laser (Spectra Physics Inc., Mt View, CA). It produces 6.4 mm diameter intense laser beam pulses at 1064 nm, which can be frequency tripled if desirable. At 1064 nm, the pulse length and energy are 9 ns and 257 mJ, respectively; at 355 nm, these are 6 ns and 60 mJ, respectively.

The optical system that is used to focus the laser beams must have a numerical aperture (i.e., ratio between the input beam diameter at the focusing lens and the focal distance) of approximately 0.18 in order to achieve a spot diameter of $\sim 10\mu$m on target [187]. On the other hand, the minimal distance between the optical system and the sample surface is approximately 200 mm in order to keep all optics outside the vacuum. Therefore, two beam expanders are used to expand the laser beams with a factor of 16 and 4, respectively (see

Figure 8.1). A doublet laser collimator lens (240 mm focal length) is used for focusing. The beam expanders and focusing lens were fabricated by Optics for Research (Caldwell, NJ). The focused laser light is coupled into the line of view of the sample viewing system with a 1 mm thickness $62 \times 82\,\mathrm{mm}^2$ sapphire laser mirror (Eksma Co, Vilnius, Lithuania). A mirror is available for each of the two laser wavelengths. Special mirror mounts were in-house constructed to exchange the mirrors whilst reproducing the position of the laser focus at target within 20 $\mu$m.

### *8.2.4 Sample Manipulation*

The sample manipulator is based on a Fisons Omniax MXY25 and MZ200 high precision XY-translation and Z-translation stage. It consists of a bellows XY-stage on which a 200 mm bellows for the Z-movement is mounted. This arrangement provides a maximum XY-motion of $\pm 12.5$ mm and a maximum Z-motion of 200 mm to a 50 mm diameter support tube (see Figure 8.1). The sample table on which the sample holder (that carries the samples) is clamped, is mounted at the end of this tube.

The translation stages are driven by DC motors. Rotations of these motors are detected by optical increment encoders and are fed back to the motorization controller unit. The controller unit uses this information to keep the position of the sample table with respect to a reference position (defined by optical marks which are automatically traced by optical sensors) updated during sample translations. The controller unit supports two modes of sample translation: a number of relative translations from an actual sample position, each initiated by an external trigger signal, and absolute translations to a specified sample position. The resolution of the encoders in combination with the gear boxes attached to the motors and the reproducibility of the Fisons components allows the reproduction of sample positions well within 1 $\mu$m.

Software was developed in-house for communication with the motorization controller and the calibration of the different degrees of freedom. The software provides a graphical user interface in which sample translations can be defined on basis of visual images of the sample. These images are captured life from the video signal that is recorded by the sample viewing system.

## 8.3 Experimental

### *8.3.1 Instrumental*

Preliminary spatially resolved experiments were carried out with the newly constructed instrument that was described in the previous section. Details on the operation of the ion trap, the ion optics, and the laser can be found in Chapter 7.

Line scans were performed in this instrument by moving the samples with a constant velocity of 3 $\mu$m/s underneath the spot of the desorption laser in the direction perpendicular to the layers. The 355 nm beam of the frequency tripled Q-switched Nd:YAG laser was used, which was focused to 20 $\mu$m. The desorbed neutrals were post-ionized by means of 25 eV electron ionization. During the movement over the sample, the laser was fired and mass spectra were recorded by the ITMS every $\sim$1 s.

### 8.3.2 Sample Preparation

Multilayered paint samples were produced from two Liquitex acrylic paints (Lefranc & Bourgeois, Le Mans, France), which contained phtalocyanine blue ($C_{32}H_{16}N_8Cu$) and phtalocyanine green pigment ($C_{32}Cl_{16}N_8Cu$), respectively. An alternating stack of twelve approximately 100 $\mu$m thickness layers was created. Spacers were used to control the layer thickness. The sample was dried at $\sim 100^0$C under air for 15 min. every time a new layer was applied. The final sample was cut to a size of $2 \times 5$ mm$^2$ and clamped on its side onto the sample holder.

## 8.4 Results

### 8.4.1 Spatially Resolved Measurement of the Pigments in a Multilayer Paint Sample

The performance of the novel ion source was tested with measurements of the multilayer paint sample. Figure 8.4 shows the results of a line scan over this sample. The intensities in the individual mass spectra were summed over the mass ranges $m/z$ 574-576 and $m/z$ 1000-1150 (i.e., the mass ranges in which molecular ions of the phtalocyanine blue and phtalocyanine green pigment are respectively expected). These ion currents are plotted in Figure 8.4 A and B, respectively. These plots show that the different layers are clearly resolved. The spatial resolution in the measurements was estimated by comparison of the ion currents. It was determined from Figure 8.4 A and B that the shortest distance over which both pigments are detected was approximately $25\mu$m (which applied to roughly half of the layer boundaries) and represents the spatial resolution. This is in good agreement with the observed crater diameter of 20 $\mu$m. Around some of the layer boundaries (for instance, the boundary between layer 1 and 2), both pigments were detected over distances up to $80\mu$m. It was observed that in these cases the line scan was not perpendicular to the layer boundary due to imperfections in the sample.

The spectra averaged over the third and the sixth layer are plotted in Figure 8.4 C and D, respectively. Both spectra comprise a total of 20 laser shots and exclusively show the molecular ions of the respective pigments. Given the number of laser shots that is averaged, the spectra exhibit a very large signal-to-noise ratio. This is indicative for a high sensitivity of the new ion source. Of course, quantification of the sensitivity is not possible on basis of these measurements. Nevertheless, the present experience is that the configuration for spatial resolved laser desorption offers a higher sensitivity than the MALDI configuration that was presented in Chapter 7.

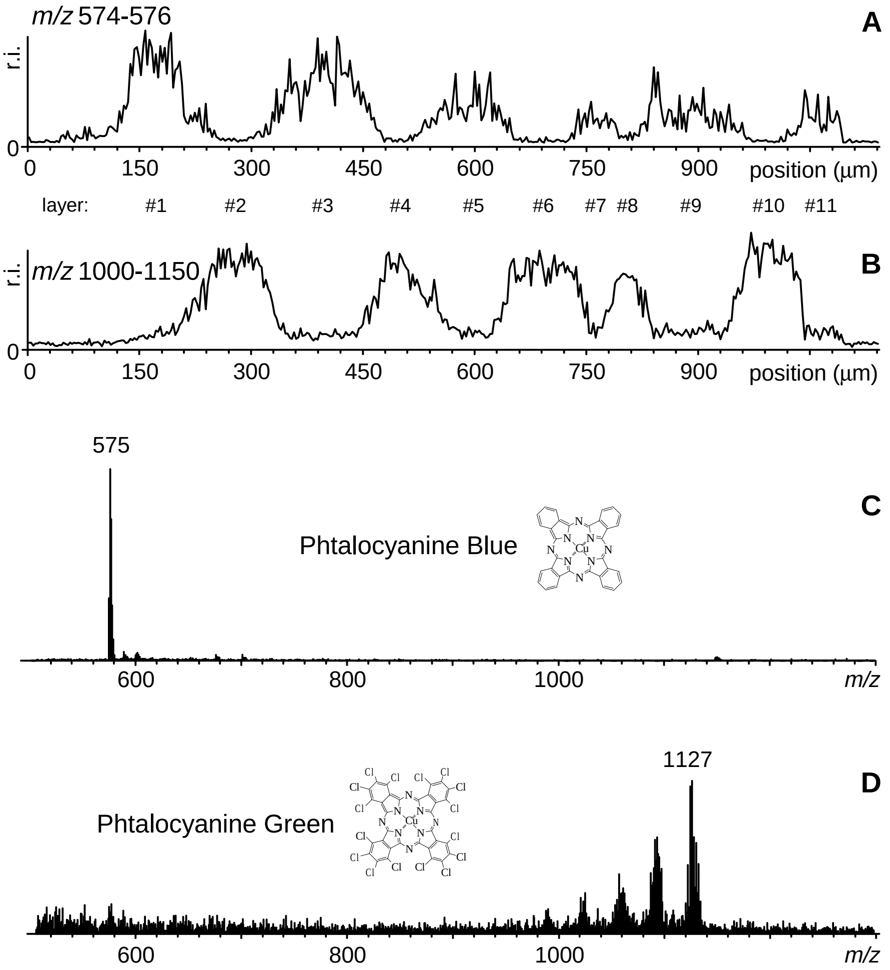

**Figure 8.4:** *Line scan over a multilayer paint sample, which consisted of 10 acrylic paint layers containing alternately phtalocyanine blue and phtalocyanine green pigment. The top graphs (A & B) show the ion currents over the two mass ranges where the molecular ions of the two different pigments are expected as a function of the position on the sample. The spectra corresponding to the third and the sixth layer (as determined from the ion currents) are plotted in the lower graphs (C & D).*

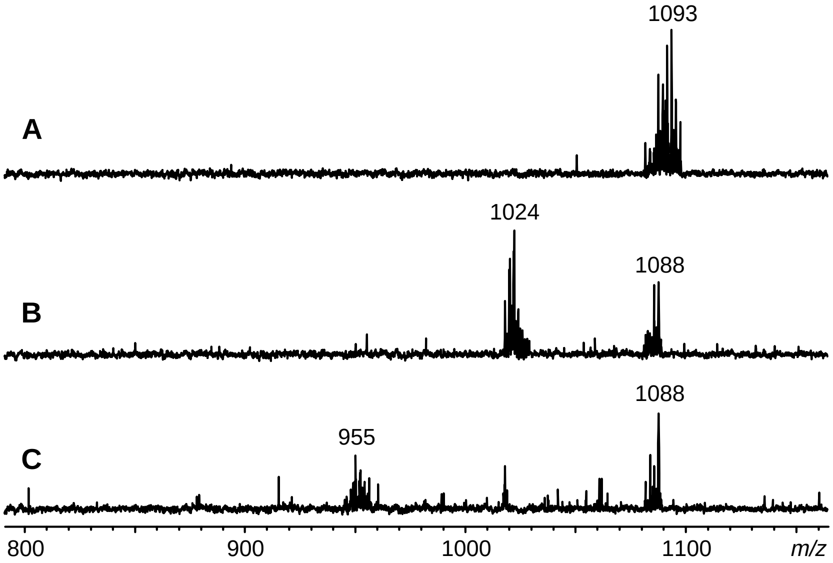

**Figure 8.5:** *Spatially resolved MS$^3$ laser desorption experiment on phtalocyanine green. After isolation of the molecular ions around $m/z$ 1093 (A), the higher mass part of the cluster was fragmented (B), and the resulting daughter ions were again fragmented (C).*

In Figure 8.5, an example of structural information obtained from spatially resolved MS$^3$ experiments is given. For these spectra, 25 consecutive laser shots were fired at the same position on a layer that contained phtalocyanine green pigment and were averaged. After isolation of the cluster around m/z 1093 (Figure 8.5 A), the higher mass part of the cluster was kinetically excited to induce fragmentation by means of collisional induced dissociation. The excitation waveform comprised a small frequency band, which corresponded to the resonance frequencies of the mass interval $m/z \sim 1089 - 1099$. The amplitude was 3.5 V and the time associated with the excitation event was 100 ms. The spectrum in Figure 8.5 B demonstrates that the excited ions were effectively fragmented and that a loss of $Cl_2$ was the result. Furthermore, there is no significant decrease in ion signal observed for the unfragmented molecular ions ($1080 < m/z < 1089$). This demonstrates that the excitation event leaves ions outside the excitation range unaffected. Note that the shape of the isotopic clusters around $m/z$ 1024 and $m/z$ 1088 in Figure 8.5 B are complementary and resemble the shape of the original isotopic cluster of the molecular ion in Figure 8.5 A. Similar fragmentation of the daughter ions around $m/z$ 1024 ($m/z$ $> 1019$) again led to a loss of $Cl_2$ (Figure 8.5 C). Losses of $Cl_2$ are to be expected from fully chlorinated aromatic systems, such as phtalocyanine green.

## 8.5 Summary and Conclusions

A new instrument for Laser Microprobe quadrupole Ion Trap Mass Spectrometry with a spatial resolution of 10 $\mu$m was designed, built, and tested. Preliminary measurements of the pigments in a paint cross section demonstrated an actual spatial resolution of approximately 25 $\mu$m and the possibility of structural studies by $MS^n$ experiments. It is expected that the spatial resolution can be further improved by realignment of the laser optics and optimization of the applied power densities.

# Bibliography

[1] H. D. Beckey, (Pergamon Press, Oxford, 1977).
[2] C. R. Blakley, J. J. Carmody, and M. L. Vestal, Anal. Chem **52,** 1636–1641 (1980).
[3] C. M. Whitehouse, R. N. Dreyer, M. Yamashita, and J. B. Fenn, Anal. Chem **57,** 675–679 (1985).
[4] M. Barber, R. S. Bordoli, R. S. Sedgwick, and A. N. Tyler, J. Chem. Soc. Chem. Commun. pp. 325–327 (1981).
[5] R. D. Macfarlane and D. F. Torgerson, Science **191,** 920 (1976).
[6] A. Benninghoven and W. K. Sichtermann, Anal. Chem **50,** 1180 (1978).
[7] R. J. Cotter, Anal. Chim. Acta **195,** 45–59 (1987).
[8] F. Hillenkamp and H. Ehring, In *Mass Spectrometry in the Biological Sciences: A Tutorial*, M. L. Gross, ed., pp. 165–179 (Kluwer Academic, Dordrecht, 1992).
[9] F. Hillenkamp, M. Karas, R. C. Beavis, and B. T. Chait, Anal. Chem **63,** 1193A–1203A (1991).
[10] in *Proceedings of the LAMMA-Workshop, 1-2 September 1983*, U. Seydel and B. Lindner, eds., (Borstel, Germany, 1983).
[11] in *Proceedings of the Third International Laser Microprobe Mass Spectrometry Workshop, 26-27 August 1986*, University of Antwerp, F. Adams and L. Van Vaeck, eds., (Antwerp, Belgium, 1986).
[12] in *Microbeam Analysis - 1989*, P. E. Russel, ed., (San Francisco Press, Inc, San Francisco, 1989).
[13] L. Van Vaeck, H. Struyf, W. Van Roy, and F. Adams, Mass Spectrom. Rev. **13,** 189–208 (1994).
[14] L. Van Vaeck, H. Struyf, W. Van Roy, and F. Adams, Mass Spectrom. Rev. **13,** 209–232 (1994).
[15] R. Zenobi, Int. J. Mass Spectrom. Ion Processes **145,** 51–77 (1995).
[16] M. Karas, U. Bahr, and U. Giessmann, Mass Spectrom. Rev. **10,** 335–357 (1991).
[17] M. V. Buchanan and R. L. Hettich, Anal. Chem **65,** 245A–259A (1993).
[18] A. M. Belu, J. M. DeSimone, R. W. Linton, G. W. Lange, and R. M. Friedman, J. Am. Soc. Mass Spectrom. **7,** 11–24 (1996).
[19] R. Honig, Appl. Phys. Lett. **2,** 138–139 (1963).
[20] J. Berkowitz and W. A. Chupka, J. Chem. Phys. **40,** 2735 (1964).
[21] K. A. Lincoln, Anal. Chem **37,** 541 (1965).
[22] B. E. Knox and F. J. Vastola, Laser Focus **3,** 15 (1967).
[23] N. C. Fenner and N. R. Daly, J. Mater. Sci. **3,** 259 (1968).
[24] F. Vastola and A. Pirone, In *Symposium on Pyrolysis Reactions of Fossil Fuels, in 151st Meeting of the Division of Fuel Chemistry*, (Pittsburgh, 1966).
[25] F. J. Vastola, R. O. Mumma, and A. J. Pirone, Org. Mass Spectrom. **3,** 101 (1970).
[26] M. A. Posthumus, P. G. Kistemaker, H. L. C. Meuzelaar, and M. C. ten Neuver de Brauw, Anal. Chem **50,** 985 (1978).
[27] H. Vogt, H. J. Heinen, S. Meier, and R. Wechsung, Fresenius. Z. Anal. Chem. **308,** 195 (1981).
[28] H. J. Heinen, S. Meier, and R. Wechsung, Int. J. Mass Spectrom. Ion Processes **47,** 19–22 (1983).
[29] T. Dingle, Vacuum **31,** 571 (1981).
[30] R. J. Conzemius and J. M. Capellen, Int. J. Mass Spectrom. Ion Phys. **34,** 197 (1980).
[31] M. Karas, D. Bachmann, U. Bahr, and F. Hillenkamp, Int. J. Mass Spectrom. Ion Processes **78,** 53–68 (1987).
[32] M. Karas and F. Hillenkamp, Anal. Chem **60,** 2299–2301 (1988).

[33] K. Tanaka, H. Waki, Y. Ido, S. Akita, Y. Yoshida, and T. Yoshida, Rapid Commun. Mass Spectrom. **2,** 151–153 (1988).

[34] A. L. Burlingame, R. K. Boyd, and S. J. Gaskell, Anal. Chem **70,** 647R–716R (1998).

[35] L. Van Vaeck, W. Van Roy, R. Gijbels, and F. Adams, In *Laser Ionization Mass Analysis*, A. Vertees, R. Gijbels, and F. Adams, eds., Chemical Analysis pp. 177–320 (John Wiley & Sons, New York, 1993).

[36] M. Karas, D. Bachmann, and F. Hillenkamp, Anal. Chem **57,** 2935–2939 (1985).

[37] F. Hillenkamp, M. Karas, D. Holtkamp, and P. Klüsener, Int. J. Mass Spectrom. Ion Processes **69,** 265–276 (1986).

[38] F. Hillenkamp, U. Bahr, M. Karas, and B. Spengler, Scanning Microsc. Suppl. **1,** 33 (1987).

[39] B. Spengler, M. Karas, U. Bahr, and F. J. Hillenkamp, Phys. Chem. **91,** 6502 (1987).

[40] R. B. Hall, A. M. DeSantolo, and S. J. Bares, Surface Sci. **161,** L533–L542 (1985).

[41] M. G. Sherman, J. R. Kingsley, J. C. Hemminger, and R. T. McIver Jr., Anal. Chim. Acta **178,** 79 (1985).

[42] R. J. Beuhler, E. Flanigan, L. J. Greene, and L. Friedman, J. Am. Chem. Soc. **96,** 3990 (1974).

[43] P. Williams, In *Ion Formation from Organic Solids (IFOS V)*, A. Hedin, B. U. R. Sundqvist, and A. Benninghoven, eds., p. 22 (Wiley, Chichester, 1990).

[44] A. Vertes and R. Gijbels, Scanning Microsc. **5,** 317 (1991).

[45] A. Vertes, In *Microbeam Analysis - 1991*, D. Howitt, ed., (San Francisco Press, San Francisco, 1991).

[46] M. Karas and U. Bahr, In *Mass Spectrometry in Biomolecular Sciences*, R. M. Caprioli, A. Malorni, and G. Sindona, eds., NATO ASI Series C: Mathematical and Physical Sciences pp. 33–50 (Kluwer Academic Publishers, Dordrecht, The Netherlands, 1996).

[47] E. D. Hardin and M. L. Vestal, Anal. Chem **53,** 1492 (1981).

[48] R. J. Cotter, Anal. Chem **52,** 1767 (1980).

[49] D. A. McCrery, E. B. Ledford, and M. L. Gross, Anal. Chem **54,** 1435–1437 (1982).

[50] C. L. Wilkins, D. A. Weil, C. L. C. Yang, and C. F. Ijames, Anal. Chem **57,** 520–524 (1985).

[51] C. F. Ijames and C. L. Wilkins, J. Am. Chem. Soc. **110,** 2687–2688 (1988).

[52] G. Krier, C. Masselon, J. F. Muller, S. Nelieu, and J. Einhorn, Rapid Commun. Mass Spectrom. **8,** 22–25 (1994).

[53] W. Paul and H. Steinwedel, Z. Naturforsch., Teil A **8,** 448 (1953).

[54] G. C. Stafford, P. E. Kelley, J. E. P. Syka, W. E. Reynolds, and J. F. J. Todd, Int. J. Mass Spectrom. Ion Processes **60,** 1984 (85).

[55] J. N. Louris, J. W. Amy, T. Y. Ridley, and R. G. Cooks, Int. J. Mass Spectrom. Ion Processes **88,** 97–111 (1989).

[56] G. L. Glish, D. E. Goeringer, K. G. Asano, and S. A. McLuckey, Int. J. Mass Spectrom. Ion Processes **94,** 15–24 (1989).

[57] A. G. Marshall and F. R. Verdun, *Fourier Transforms in NMR, Optical, and Mass Spectrometry: a User's Handbook* (Elsevier Science Publishers B.V., Amsterdam, The Netherlands, 1990).

[58] *Fundamentals of Ion Trap Mass Spectrometry*, No. Vol. 1-3 in *Practical Aspects of Ion Trap Mass Spectrometry*, R. E. March and J. F. J. Todd, eds., (CRC Press, New York, 1995).

[59] F. M. Penning, Physica (Utrecht) **3,** 873–894 (1936).

[60] S. H. Guan and A. G. Marshall, Int. J. Mass Spectrom. Ion Processes **158,** 5–37 (1996).

[61] R. M. A. Heeren, de Koster C. G., and J. J. Boon, Anal. Chem **67,** 3965–3970 (1995).

[62] R. M. A. Heeren and J. J. Boon, Int. J. Mass Spectrom. Ion Processes **157/158,** 391–403 (1996).

[63] P. Caravatti and M. Alleman, Org. Mass Spectrom. **26,** 514–518 (1991).

[64] T. D. Wood, C. W. Ross, and A. G. Marshall, J. Am. Soc. Mass Spectrom. **5,** 900–907 (1994).

[65] N. W. McLachlan, *Theory and Applications of Mathieu Functions* (Clarendon Press, Oxford, 1947).

[66] E. Z. Fischer, Phys **156,** 1 (1959).

[67] P. H. Dawson and N. R. Whetten, J. Vac. Sci. Technol. **5,** 1 (1968).

[68] P. H. Dawson and N. R. Whetten, J. Vac. Sci. Technol. **5,** 11 (1968).

[69] P. E. Kelley, G. C. Stafford, Jr., and D. R. Stephens, U.S. patent pp. 4,540,884 (1985).

[70] R. E. Kaiser, Jr., R. G. Cooks, G. C. Stafford, Jr., J. E. P. Syka, and P. E. Hemberger, Int. J. Mass Spectrom. Ion Processes **106,** 79 (1991).

[71] J. Franzen, R. H. Gabling, M. Schubert, and Y. Wang, In *Fundamentals of Ion Trap Mass Spectrometry*, R. E. March and J. F. J. Todd, eds., Practical Aspects of Ion Trap Mass Spectrometry pp. 49–167 (CRC

Press, New York, 1995).
[72] I. V. Bletsos and D. M. Hercules, Anal. Chem **63,** 1953 (1991).
[73] B. T. Chait, J. Shpungin, and F. H. Field, Int. J. Mass Spectrom. Ion Processes **58,** 121 (1985).
[74] C. L. Johlman, C. L. Wilkins, J. D. Hogan, T. L. Donavan, D. A. Laude, Jr., and M. J. Youssefi, Anal. Chem **62,** 1167 (1990).
[75] A. T. Hsu and A. G. Marshall, Anal. Chem **60,** 932 (1988).
[76] S. C. Beu, M. W. Senko, J. P. Quinn, and F. M. Wampler, III, J. Am. Soc. Mass Spectrom. **4,** 557 (1993).
[77] P. B. O'Connor and F. W. McLafferty, J. Am. Chem. Soc. **117,** 12826–12831 (1995).
[78] B. T. Chait and S. B. H. Kent, Science **257,** 1885 (1992).
[79] U. Bahr, A. Deppe, M. Karas, F. Hillenkamp, and U. Giessmann, Anal. Chem **64,** 2866–2869 (1992).
[80] G. Wilczek-Vera, P. O. Danis, and A. Eisenberg, Macromolecules **29,** 4036–4044 (1996).
[81] C. G. Smith, P. B. Smith, A. J. Pasztor, M. L. McKelvy, D. M. Meunier, and S. W. Froelicher, Anal. Chem **67,** 97R–126R (1995).
[82] S. G. Penn, M. T. Cancilla, and C. B. Lebrilla, Anal. Chem **68,** 2331–2339 (1996).
[83] D. C. Schriemer and L. Li, Anal. Chem **68,** 2721–2725 (1996).
[84] J. M. Grundwürmer, M. Bönisch, G. R. Kinsel, J. Grotemeyer, and E. W. Schlag, Int. J. Mass Spectrom. Ion Processes **131,** 139–148 (1994).
[85] P. Juhasz, M. T. Roskey, I. P. Smirnov, L. A. Haff, M. L. Vestal, and S. A. Martin, Anal. Chem **68,** 941–946 (1996).
[86] M. L. Vestal, P. Juhasz, and S. A. Martin, Rapid Commun. Mass Spect. **9,** 1044–1050 (1995).
[87] R. D. Edmondson and D. H. Russell, J. Am. Soc. Mass Spectrom. **7,** 995–1001 (1996).
[88] M. B. Comisarow and A. G. Marshall, Chem. Phys. Lett. **25,** 282–283 (1974).
[89] P. B. Marshall, A. G.; Grosshans, Anal. Chem **63,** 215A–229A (1991).
[90] M. L. Gross and D. L. Rempel, Science **226,** 261–268 (1984).
[91] F. W. McLafferty, Acc. Chem. Res. **27,** 379–386 (1994).
[92] M. Dey, J. A. Castoro, and C. L. Wilkins, Anal. Chem **67,** 1575–1579 (1995).
[93] C. Köster, J. A. Castoro, and C. L. Wilkins, J. Am. Chem. Soc. **114,** 7572–7574 (1992).
[94] R. S. Brown, D. A. Weil, and C. L. Wilkins, Macromolecules **19,** 1255–1260 (1986).
[95] L. M. Nuwaysir, C. L. Wilkins, and J. Simonsick, W. J., J. Am. Soc. Mass Spectrom. **1,** 66–71 (1990).
[96] R. C. Beavis and B. T. Chait, Chem. Phys. Lett. **181,** 479–484 (1991).
[97] J. D. Hogan and D. A. Laude, Jr., Anal. Chem **64,** 763–769 (1992).
[98] S. A. Hofstadler, S. C. Beu, and D. A. Laude, Jr., Anal. Chem **65,** 312–316 (1993).
[99] M. L. Easterling, C. C. Pitsenberger, S. S. Kulkarni, P. K. Taylor, and I. J. Amster, Int. J. Mass Spectrom. Ion Processes **157/158,** 97–113 (1996).
[100] S. J. Pastor and C. L. Wilkins, J. Am. Soc. Mass Spectrom. **8,** 225–233 (1997).
[101] P. R. Bevington, *Data Reduction and Error Analysis for the Physical Sciences* (McGraw-Hill, New York, 1969).
[102] P. J. Florry, J. Am. Chem. Soc. **62,** 1561 (1940).
[103] G. Montaudo, M. S. Montaudo, C. Puglisi, and F. Samperi, Rapid Commun. Mass Spectrom. **9,** 453 (1995).
[104] C. Jackson, B. S. Larsen, and C. N. McEwen, Anal. Chem **68,** 1303–1308 (1996).
[105] C. N. McEwen, C. Jackson, and B. S. Larsen, Polym. Prepr. **17,** 314 (1996).
[106] J. T. Brenna and W. R. Creasy, Appl. Spectrosc. **45,** 80–91 (1991).
[107] Z. M. Liang, A. G. Marshall, and D. G. Westmoreland, Anal. Chem **63,** 815–818 (1991).
[108] G. M. Alber, A. G. Marshall, N. C. Hill, L. Schweikhard, and T. Ricca, Rev. Sci. Instrum. **64,** 1845–1852 (1993).
[109] J. T. Brenna, W. R. Creasy, and J. Zimmerman, Adv. Chem. Ser. pp. 129–154 (1993).
[110] J. A. Castoro, C. Köster, and C. L. Wilkins, Anal. Chem **65,** 784–788 (1993).
[111] P. A. Limbach, H. S. Kim, N. C. Hill, and A. G. Marshall, Anal. Chim. Acta **277,** 31–39 (1993).
[112] E. R. E. van der Hage, M. C. Duursma, R. M. A. Heeren, J. J. Boon, M. W. F. Nielen, A. J. M. Weber, C. G. Koster, and N. K. de Vries, Macromolecules **30,** 4302–4309 (1997).
[113] C. L. Pastor, S. J.; Wilkins, Int. J. Mass Spectrom. Ion Processes **175,** 81–92 (1998).
[114] R. Priorr, In *Surfactants in Consumer Products*, J. Falbe, ed., p. 5 (Springer-Verlage, Heidelberg, 1987).

[115] A. J. Ryan and J. L. Stanford, In *Comprehensive Polymer Science*, G. Allen and J. C. Bevington, eds., p. 427 (Pergamon Press, Oxford, 1989).

[116] H. T. Kalinoski, In *Nonionic Surfactants Polyoxyalkylene Block Copolymers*, V. M. Nace, ed., p. 31 (Marcel Dekker, New York, 1996).

[117] B. Chu, Langmuir **11,** 414 (1995).

[118] B. Chu and Z. Zhou, In *Nonionic Surfactants Polyoxyalkylene Block Copolymers*, V. M. Nace, ed., p. 67 (Marcel Dekker, New York, 1996).

[119] T. M. Schmitt, *Nonionic Surfactants*, Vol. 40 of *Surfactant Science Series* (Marcel Dekker, New York, 1992).

[120] E. Kreyszig, in *Advanced Engineering Mathematics* (John Wiley & Sons, Inc., New York, 1993), Chap. 23.

[121] A. G. Marshall, T. C. Wang, and T. L. Ricca, J. Am. Chem. Soc. **107,** 7893–7897 (1985).

[122] L. Chen, T. C. L. Wang, T. L. Ricca, and A. G. Marshall, Anal. Chem **59,** 449–454 (1987).

[123] S. Guan and R. T. McIver, Jr., J. Chem. Phys. **91,** 775–777 (1989).

[124] S. Guan and R. T. McIver, Jr., J. Chem. Phys. **92,** 5841–5846 (1990).

[125] S. H. Guan and A. G. Marshall, Anal. Chem **65,** 1288–1294 (1993).

[126] S. Guan and P. R. Jones, Rev. Sci. Instrum. **59,** 2573–2576 (1989).

[127] S. C. Bue and D. A. Laude, Jr., "Modular Data System for Selective Waveform Excitation and Trapping Experiments in FTMS," Anal. Chem **63,** 2200–2203 (1991).

[128] C. D. Hanson, M. E. Castro, E. L. Kerley, and D. H. Russell, Anal. Chem **62,** 1352–1355 (1990).

[129] C. W. Ross, III, S. Guan, P. B. Grosshans, T. L. Ricca, and A. G. Marshall, J. Am. Chem. Soc. **115,** 7854–7861 (1993).

[130] L. Chen and A. G. Marshall, Rapid Commun. Mass Spectrom. **1,** 39–42 (1987).

[131] R. G. Cooks, *Collision Spectroscopy* (Plenum, New York, 1978).

[132] in *Tandem Mass Spectrometry*, F. W. McLafferty, ed., (John Wiley & Sons, Inc., New York, 1983).

[133] K. L. Busch, G. L. Glish, and S. A. McLuckey, *Mass Spectrometry / Mass Spectrometry: Techniques and Applications of Tandem Mass Spectrometry* (VCH, New York, 1988).

[134] J. W. Gauthier, T. R. Trautman, and D. B. Jacobson, Anal. Chim. Acta **246,** 211–225 (1991).

[135] S. Koster, M. C. Duursma, J. J. Boon, and R. M. A. Heeren, J. Am. Soc. Mass Spectrom. (1999), submitted for publication.

[136] E. Margioliash, E. L. Smith, G. Kreil, and H. Tuppy, Nature **192,** 1125–1127 (1961).

[137] C. K. Mathews and K. E. Holde, in *Biochemistry* (The Benjamin/Cummings Publishing Company, Redwood City, CA, 1990), chapter 15, p. 513.

[138] K. D. Henry, Q. J. P., and F. W. McLafferty, J. Am. Chem. Soc. **113,** 5447–5449 (1991).

[139] J. F. Banks and C. M. Whitehouse, In *High resolution separation and analysis of biological Macromolecules Part A Fundamentals*, K. B. L. and H. W. S., eds., Methods in Enzymology pp. 486–514 (Academic Press, London, 1996).

[140] R. C. Beavis and B. T. Chait, Anal. Chem **62,** 1836–1840 (1990).

[141] A. G. Marshall and D. C. Roe, J. Chem. Phys. **73,** 1581–1590 (1980).

[142] G. T. Uechi and R. C. Dunbar, J. Am. Soc. Mass Spectrom. **3,** 734–741 (1992).

[143] M. L. Easterling, C. C. Pitsenberger, and I. J. Amster, J. Am. Soc. Mass Spectrom. **8,** 195–198 (1997).

[144] S. H. Guan, L. Pasatolic, A. G. Marshall, and X. Z. Xiang, Int. J. Mass Spectrom. Ion Processes **139,** 75–86 (1994).

[145] J. A. Bresson, G. A. Anderson, J. E. Bruce, and R. D. Smith, J. Am. Soc. Mass Spectrom. **9,** 799–804 (1998).

[146] S. A. Hofstadler, J. E. Bruce, A. L. Rockwood, G. A. Anderson, B. E. Winger, and R. D. Smith, Int. J. Mass Spectrom. Ion Processes **132,** 109–127 (1994).

[147] M. L. Easterling, software written in the C programming language (MIPSPRO compiler and associated math libraries), available upon request, Department of Chemistry, University of Georgia, Athens, GA.

[148] IsoPro 3.0, MS/MS Software, http://members.aol.com/msmssoft.

[149] Y. Naito and M. Inoue, Int. J. Mass Spectrom. Ion Processes **158,** 85–96 (1996).

[150] E. N. Nikolaev, N. V. Miluchihin, and M. Inoue, Int. J. Mass Spectrom. Ion Processes **148,** 145–157 (1996).

[151] A. J. Peurrung and R. T. Kouzes, Int. J. Mass Spectrom. Ion Processes **145,** 139–153 (1995).
[152] D. W. Mitchell and R. D. Smith, Phys. Rev. E **52,** 4366–4386 (1995).
[153] J. T. Stults, Anal. Chem **69,** 1815–1819 (1997).
[154] J. Y. Huang, P. W. Tiedemann, D. P. Land, R. T. McIver, and J. C. Hemminger, Int. J. Mass Spectrom. Ion Processes **134,** 11–21 (1994).
[155] A. G. Marshall, M. B. Comisarow, and G. Parisod, J. Chem. Phys. **71,** 4434–4444 (1979).
[156] Y. Naito and M. Inoue, Rapid Commun. Mass Spectrom **11,** 578–586 (1997).
[157] D. W. Mitchell and R. D. Smith, Int. J. Mass Spectrom. Ion Processes **165,** 271–297 (1997).
[158] D. W. Mitchell and R. D. Smith, J. Mass Spectrom. **31,** 771–790 (1996).
[159] J. A. Breeson, G. A. Anderson, J. E. Bruce, and R. D. Smith, J. Am. Soc. Mass Spectrom. **9,** 799 (1998).
[160] F. B. Fenn, M. Mann, C. K. Meng, S. F. Wong, and C. M. Whitehouse, Mass Spectrom. Rev. **9,** 37–70 (1990).
[161] D. N. Heller, I. Lys, R. J. Cotter, and O. M. Uy, Anal. Chem **61,** 1083–1086 (1989).
[162] V. M. Doroshenko, T. J. Cornish, and R. J. Cotter, Rapid Commun. Mass Spectrom. **6,** 753–757 (1992).
[163] D. M. Chambers, D. E. Goeringer, S. A. McLuckey, and G. L. Glish, Anal. Chem **65,** 14–20 (1993).
[164] V. M. Doroshenko and R. J. Cotter, Rapid Commun. Mass Spectrom. **7,** 822–827 (1993).
[165] K. Jonscher, G. Currie, A. L. McCormack, and J. R. Yates, III, Rapid Commun. Mass Spectrom. **7,** 20–26 (1993).
[166] J. C. Schwartz and M. E. Bier, Rapid Commun. Mass Spectrom. **7,** 27–32 (1993).
[167] A. W. T. Bristow and C. S. Creaser, Rapid Commun. Mass Spectrom. **9,** 1465–1469 (1995).
[168] J. Qin, J. M. M. Steenvoorden, and B. T. Chait, Anal. Chem **68,** 1784–1791 (1996).
[169] R. K. Ghosh, A. S. Arora, and L. Narayan, Int. J. Mass Spectrom. Ion Phys. **23,** 237 (1977).
[170] C. S. O and H. A. Schuessler, J. Appl. Phys. **52,** 1157 (1981).
[171] C. Weil, M. Nappi, C. D. Cleven, H. Wolnik, and R. G. Cooks, Rapid Commun. Mass Spectrom. **10,** 742–750 (1996).
[172] R. E. March and R. J. Hughes, *Quadrupole Storage Mass Spectrometry* (John Wiley & Sons, Inc., New York, 1989).
[173] J. F. J. Todd, Mass Spectrom. Rev. **10,** 3–52 (1991).
[174] S. A. McLuckey, G. L. Glish, and K. G. Asano, Anal. Chim. Acta. **225,** 25–35 (1989).
[175] K. Yoshinari, Y. Ose, and Y. Kato, In *Proc. 46th ASMS Conf. Mass Spectrom. Allied Topics*, p. 492 (Orlando, Florida, 1998).
[176] P. Kofel, In *Practical Aspects of Ion Trap Mass Spectrometry*, R. E. March and J. F. J. Todd, eds., (CRC Press, New York, 1995).
[177] G. C. Eiden, M. E. Cisper, M. L. Alexander, and P. H. Hemberger, J. Am. Soc. Mass Spectrom. **4,** 706 (1993).
[178] G. C. Eiden, A. W. Garrett, M. E. Cisper, N. S. Nogar, and P. H. Hemberger, Int. J. Mass Spectrom. Ion Processes **136,** 119–141 (1994).
[179] V. M. Doroshenko and R. J. Cotter, J. Mass Spectrom. **32,** 602–615 (1997).
[180] J. Qin and B. T. Chait, Anal. Chem **68,** 2102–2107 (1996).
[181] J. E. Fulford, D. N. Hoa, R. J. Hughes, R. E. March, R. F. Bonner, and G. J. Wong, J. Vac. Sci. Technol. **17,** 829–835 (1980).
[182] F. Vedel, M. Vedel, and R. E. March, Int. J. Mass Spectrom. Ion Processes **99,** 125–138 (1990).
[183] F. Vedel, M. Vedel, and R. E. March, Int. J. Mass Spectrom. Ion Processes **108,** R11–R20 (1991).
[184] F. D. Williams and R. G. Cooks, Rapid Commun. Mass Spectrom. **7,** 380–382 (1993).
[185] M. H. Soni, P. S. H. Wong, and R. G. Cooks, Anal. Chim. Acta **303,** 149–162 (1995).
[186] D. A. Dahl, *SIMION 3D Version 6.0 User's Manual* (Princeton Electronic Systems, Princeton, NJ, 1995).
[187] G. Dalessi, 1996, (Applied Laser Technology, Best, The Netherlands), private communication.

# Summary

The formation of intact gas phase ions from compounds in the condensed phase is a major challenge in mass spectrometry. In recent years, laser desorption techniques have proven to be powerful tools to achieve this conversion. These techniques have allowed organic chemical studies with mass spectrometry on a wide range of polar, nonvolatile, high molecular weight, and thermally labile compounds in complex samples. An additional advantage of laser desorption is the possibility to focus laser beams to very small spot sizes, which allows spatially resolved surface analyses at the micrometer level.

This thesis deals with the coupling of laser desorption techniques to the two types of trapped ion mass analyzers: the Fourier Transform Ion Cyclotron Resonance Mass Spectrometer (FTICR-MS) and the quadrupole Ion Trap Mass Spectrometer (ITMS). An introduction on the theoretical concepts and the operating principles of these mass spectrometers is given in Chapter 2. Although the application of laser desorption in trapped ion mass spectrometers is very attractive (Chapter 1), it is certainly not a trivial task. Problems and pitfalls associated with the implementation of laser desorption initiated most of the experiments and instrumental developments described in this thesis.

Chapter 3 describes the implementation of a newly constructed external ion source for Matrix Assisted Laser Desorption and Ionization (MALDI) in the FTICR-MS instrument. Experiments on low molecular weight polymers are carried out to investigate two key issues in the performance of this configuration: the accuracy of the mass determinations and mass discrimination effects that distort the measured spectra. On basis of the experimental data, new methods for processing the mass spectra are developed. These are successfully applied to determine polymer end group mass with an accuracy within 0.003 u for the molecular weight range from $m/z$ 500 to 1400 and within 0.02 u for $m/z$ 3400 to 5000, which demonstrates the superior resolution of the new configuration. Measured molecular weight distributions however exhibit flight-time induced distortions that are inherent to the requirement to analyze discrete ion bunches in external ion source FTICR-MS. It is shown that superimposition of several mass spectra, which are acquired at different trapping times, compensates for these distortions.

The MALDI-FTICR-MS technique along with the methodologies developed in Chapter 3 are applied to triblock polymers of poly(oxypropylene) and poly(oxyethylene) in Chapter 4. The copolymer results show that apart from flight-time induced mass discrim-

ination also the variation in isotopic patterns over the measured mass range and overlap of peaks in the spectrum must be considered before accurate information on block length distributions can be deduced. An analytical treatment of the spectral data is presented to correct the measured molecular weight distributions, which made it possible to obtain for the first time detailed and accurate molecular weight data on such a complex sample. The experimentally verified random coupling hypothesis supports the validity of the methodologies proposed to process the spectral data.

It became evident in the course of the MALDI experiments on polymers that the versatility of the FTICR-MS instrument is immensely broadened if ions can be manipulated in a mass selective way. Chapter 5 describes the design and performance of a novel arbitrary waveform generator, which has been constructed to address this need. Its ultra-high mass selectivity is demonstrated with the isotopic depletion of a complex polyoxyalkeneamine distribution (produced by matrix assisted laser desorption/ionization) and the isolation of a single isotope from the charge-state distribution of cytochrome c (produced by electrospray ionization) in FTICR-MS measurements.

The arbitrary waveform generator is utilized in Chapter 6 to investigate isotope beating as a source of error in the determination of polymer molecular weight distributions. Isotope beating is a beat pattern in the measured time-domain FTICR-MS signal that is caused by periodical destructive interference of the orbital motion of isotopes. Experimental results show that significant errors in the measured relative abundances appear if transients are sampled for less than two beat periods. Computer simulations show a similar behavior and indicate that the distortions are induced by isotope beating. With the help of the newly constructed AWG system, it was possible to obtain experimental data on an isotopically depleted polymer distribution similar to the one studied in the computer simulations. Distortions that depend on the transient length are not observed in these spectra. This proves that isotope beating is responsible for distortions in measured molecular weight distributions if transients are acquired for too short durations.

Chapter 7 describes a newly configured external ion source MALDI-ITMS instrument. Again, synthetic polymer samples are used to characterize its performance. Mass discrimination effects are probed by comparison of measurements of polymer standards in the mass range $m/z$ 400 to 3400 with MALDI-TOF-MS measurements of the same samples. The results indicate that it is possible to determine ideal experimental conditions for analyzing mass ranges smaller than 1000 u with negligible mass discrimination. This is proved with measurements of poly(ethylene oxide) poly(propylene oxide) copolymers. Evaluation of experimentally obtained mass accuracies shows that these are highly influenced by the magnitude of the trapped ion population. Consequently, reproducible results can only be obtained by controlling the total space charge in the trap. In MALDI experiments, this can be achieved if the laser power is tuned just above threshold. In this way, the mass of three different end groups in a complex polymer sample is successfully determined with an accuracy of better than 0.1 u.

Finally, the experience obtained with respect to laser desorption as well as trapped ion mass spectrometry is exploited in Chapter 8 to design and construct a novel ion source for spatially resolved analyses with a spatial resolution of 10 $\mu$m. This laser microprobe ion source is successfully coupled to the ITMS instrument. Analytical data on preliminary measurements of the pigments in a paint cross section are presented. These demonstrate a spatial resolution of approximately 25 $\mu$m and the possibility to perform spatially resolved structural studies by utilization of MS$^n$ experiments.

# Samenvatting

De overgang van gecondenseerde materie naar intacte ionen in de gasfase is een belangrijk probleem in de massaspectrometrie. Technieken die gebaseerd zijn op desorptie van stoffen met behulp van laserlicht hebben inmiddels hun kwaliteiten bewezen. Dit blijkt uit talloze succesvolle experimenten aan polaire, niet-vluchtige, zware en soms zelfs thermisch fragiele moleculen in monsters van complexe organische samenstelling. Een bijkomend voordeel van laserdesorptietechnieken is de mogelijkheid om laserbundels te focusseren tot zeer kleine diameter. Dit maakt het mogelijk om oppervlakken op micrometerschaal plaatsopgelost te bestuderen.

Het onderwerp van dit proefschrift is de implementatie van laserdesorptietechnieken in massaspectrometers die gebruik maken van het ionenvalprincipe voor het invangen en massascheiden van ionen. Er bestaan twee typen massaspectrometers die van dit principe uitgaan: de Fourier-transformatie ionencyclotronresonantie massaspectrometer (FTICR-MS) en de quadrupolaire ionenvalmassaspectrometer (ITMS). De theoretische achtergronden en de werking van beide systemen worden beschreven in hoofdstuk 2. De toepassing van een FTICR-MS of een ITMS voor de analyse van ionen, die gevormd zijn met behulp van laserdesorptie, is veelbelovend, maar zeker niet eenvoudig. Een groot aantal van de experimenten en de ontwikkelingen van apparatuur en methodologie, die beschreven zijn in dit proefschrift, vonden zodoende hun oorsprong in problemen, die hierbij naar voren kwamen.

Hoofdstuk 3 behandelt de toepassing van een nieuwe externe ionenbron voor matrix-geassisteerde laserdesorptie en -ionisatie in het FTICR-MS instrument. De prestaties van deze configuratie, met name met betrekking tot de nauwkeurigheid van de massabepaling en massa-afhankelijke meetgevoeligheid, zijn gekarakteriseerd aan de hand van metingen aan polymeren. De experimentele resultaten konden worden gebruikt voor het ontwikkelen van nieuwe methoden voor het verwerken van massaspectrale informatie, waarmee de massa van eindgroepen van polymeren kon worden bepaald met een nauwkeurigheid beter dan 0.003 u en 0.02 u voor het massagebied van respectievelijk $m/z$ 500 tot 1400 en $m/z$ 3400 tot 5000. Deze getallen tonen duidelijk de ongeëvenaarde massanauwkeurigheid van de nieuwe instrumentele configuratie aan. De gemeten moleculaire gewichtsverdelingen zijn echter misvormd als gevolg van een massa-afhankelijkheid in het ionentransport. Dit fenomeen wordt veroorzaakt door vluchttijdeffecten en is inherent aan de toepassing van een gepulste ionisatietechniek in een externe bron van een FTICR-MS instrument. Het kon worden aangetoond dat de juiste gewichtsverdelingen worden verkregen door metingen te verrichten bij verschillende vluchttijden en vervolgens de gemeten massaspectra over elkaar heen te leggen.

In hoofdstuk 4 worden de MALDI-FTICR-MS techniek en de methoden, die ontwikkeld zijn in hoofdstuk 3, toegepast op triblock co-polymeren van poly(propyleenoxide) en poly(ethyleenoxide). De resultaten laten zien dat naast massa-afhankelijkheden in het ionentransport ook variaties in isotooppatronen en het samenvallen van verschillende massapieken de interpretatie van massaspectra van polymeren kunnen bemoeilijken. Om voor deze effecten te corrigeren wordt er een nieuwe strategie ontwikkeld om de verdelingen in de bloklengtes in het co-polymeer te bepalen. Met deze strategie was het voor het eerst mogelijk om gedetailleerde moleculaire gewichtsinformatie te verkrijgen over zo'n gecompliceerd monster. De juistheid van deze analytische strategie wordt ondersteund door de experimentele verificatie, dat de bloklengteverdelingen voor het bestudeerde copolymeer niet gecorreleerd zijn.

De MALDI experimenten leerden dat de experimentele mogelijkheden van het FTICR-MS instrument enorm toenemen als de ingesloten ionen gemanipuleerd kunnen worden op basis van hun massa. Hiertoe werd een nieuwe functiegenerator voor arbitraire golffuncties ontwikkeld. Hoofdstuk 5 beschrijft het ontwerp en de prestaties van deze functiegenerator. De hoge graad van massaselectiviteit, die hiermee verkregen wordt, blijkt uit FTICR-MS experimenten waarin alle isotopen uit een polyoxyalkeenamine verdeling (geproduceerd met MALDI) verwijderd worden en waarin één enkele isotoop in de verdeling in ladingstoestanden van cytochrome c (geproduceerd met electrospray) geïsoleerd wordt.

In hoofdstuk 6 wordt deze functiegenerator toegepast om te onderzoeken in hoeverre isotoopmodulaties de bepaling van moleculaire gewichtsverdelingen in polymeren beïnvloeden. Isotoopmodulaties komen tot uiting als een golfpatroon in het FTICR-MS signaal, dat gemeten wordt in het tijdsdomein. Zij worden veroorzaakt door interferentie als gevolg van kleine frequentieverschillen in de cirkelbewegingen die verschillende isotopen beschrijven. De experimentele resultaten tonen aan dat aanzienlijke fouten in de gemeten relatieve intensiteit ontstaan, indien het gemeten FTICR-MS signaal minder dan twee modulatieperiodes bevat. Computersimulaties bevestigen hetzelfde effect als zijnde veroorzaakt door isotoopmodulaties. Dankzij de nieuwe functiegenerator was het mogelijk om metingen te verrichten aan een monoisotopische polymeerverdeling, die tevoren bestudeerd was met behulp van computersimulaties. Deze metingen vertonen geen fouten als functie van de meettijd. Dit bewijst dat isotoopmodulaties de bepaling van gewichtsverdelingen verstoren, indien het FTICR-MS signaal te kort gemeten wordt.

Hoofdstuk 7 beschrijft een nieuw MALDI-ITMS instrument met een externe ionenbron. Ook in dit hoofdstuk worden synthetische polymeren gebruikt om de prestaties van dit instrument te karakteriseren. Massa-afhankelijkheden in de metingen worden onderzocht door de resultaten van metingen aan polymeerstandaarden in het massagebied van $m/z$ 400 tot 3400 te vergelijken met resultaten, die verkregen waren met MALDI-TOF-MS. Hieruit blijkt dat het mogelijk is om in een massagebied, kleiner dan 1000 u, dergelijke afhankelijkheden uit te schakelen door optimale experimentele condities te kiezen. Deze waarneming wordt gestaafd door metingen aan poly(ethyleenoxide) poly(propyleenoxide) co-polymeren. Wanneer echter naar de massanauwkeurigheid van de metingen gekeken wordt, dan valt op dat deze sterk beïnvloed worden door het totale aantal ionen dat ingesloten is. Als gevolg hiervan is het noodzakelijk voor het verkrijgen van reproduceerbare resultaten om dit aantal nauwkeurig te beheersen. In MALDI experimenten is dit mogelijk door het laservermogen net boven de ionisatiedrempel in te stellen. Deze werkwijze is succesvol toegepast om de massa van drie verschillende eindgroepen in een complex polymeermonster te bepalen met een nauwkeurigheid, die beter is dan 0.1 u.

Tenslotte wordt de ervaring, die verkregen is op het gebied van laserdesorptie en van ionenvalmassaspectrometers, teogepast in hoofdstuk 8 om een nieuwe ionenbron voor plaatsopgelost onderzoek met een resolutie van 15 $\mu$m te ontwikkelen. Deze bron is met succes ingebouwd in een ITMS instrument. De resultaten van een verkennende studie aan de pigmenten in een dwarsdoorsnede van een verfmonster tonen een voorlopige plaatsresolutie van 25 $\mu$m aan en illustreren de mogelijkheden om plaatsopgelost structuuronderzoek door middel van MS$^n$ experimenten te verrichten.

# Nawoord

Hoewel enkel mijn eigen naam op de voorkant vermeld staat, is dit proefschrift natuurlijk het resultaat van inspanningen van een grote groep mensen. Hierbij dank ik iedereen die een bijdrage heeft geleverd. Het zou echter onterecht zijn om een aantal mensen niet bij naam te noemen.

In de eerste plaats gaat mijn speciale dank uit naar Jaap Boon en Ron Heeren. Niet alleen hun wetenschappelijke bijdrage, maar ook hun betrokkenheid bij voor- en tegenspoed, die niet direct met de promotie te maken had, hebben gezorgd voor een goede stimulans en enthousiasme voor het onderzoek.

Tina Weeding, Piet Kistemaker en Chris de Koster ben ik erg dankbaar voor hun aanvullende hulp en suggesties op wetenschappelijk gebied.

De dagelijkse werkzaamheden werden enorm verlicht door de hulp in het chemisch lab van Marc Duursma, de technische ondersteuning van Michel de Wilde en de hulpverlening van Gert Eijkel bij computerproblemen. Door dit te koppelen aan gezelligheid en emotionele steun, zijn zij meer dan dierbare collega's geworden. Dit laatste is in het bijzonder van toepassing op Frans Giskes. Hoewel het niet tot zijn taken behoorde, is hij vaak bijgesprongen in talloze “haastklusjes” en is hij een bijzondere vriend geworden.

De ontwikkeling van nieuwe apparatuur heeft veel werk met zich meegebracht voor de ondersteunende groepen. Zo werden tekeningen gemaakt door Herman Ficke en Joop van Dorsselaer, welke vervolgens door Jan v.d. Linden, Henk Neerings, Hildebrand Voort, Wim Brouwer, Wim Barsinghorn, Menno Borsboom en Dirk Exalto werden vertaald in roestvrij staal. Electronica en software werden ontwikkeld en onderhouden door Hans Alberda, Hans ter Horst, Idsart Attema, Henk Dekker, Cees van Doornik, Anton Vijftigschild, Jan van Elst, Ben Okhuysen, Ronald Grosmann, Guus Ruwiel, Sjoerd Wouda en Els Homan.

Mijn periode op AMOLF was zeker niet zo aangenaam geweest zonder de prettige samenwerking en de goede werksfeer tussen de mensen met wie ik een kamer heb mogen delen (Jaap Beijersbergen, Erik v.d. Hage, Pete O'Connor, Vincent Klap en Marcel Janson) en alle andere mensen in de groep macromoleculen (in “past and present”: Oscar v.d. Brink, Jos Pureveen, Jerre v.d. Horst, Gisela v.d. Doelen, Peter Arisz, Klaas-Jan v.d. Berg, Sander Koster, Jorrit v.d. Berg, Nicolas Wyplosz, Jaap v.d. Weerd, Georgiana Languri, Oscar van Hoof, Linda Hartgring, Ad de Snaijer, Ilja Stavenuiter, Hugo Vijftigschild, Liz Minor, Annebeth Kerkhof, Sophie Peulvé, Janine de Maaijer, Leo Spetter, Marco & Ivana Bobeldijk, Muriel Geldof, Marieke van Veen, David Rainford en Jan Commandeur). Andere mensen in het lab die hebben bijgedragen aan een plezierige tijd op AMOLF zijn Wim Koppers, Bart Berenbak, Steven de Vries, Iliya Cerjak, Ulrich Emmerichs, Sander Woutersen, Bernd Riedmüller, Iwan Snel, André Dijkslag, Rene Maatman, Rutger Vrijen, Marcel Lankhuizen, Noëlle Rutte, Erik Kossen, Willem-Jan Huisman, Malcolm Kadodwala en David Butler.

Tenslotte ben ik erg veel dank verschuldigd aan mijn familie mijn vrienden buiten AMOLF. Helaas brengt promoveren tijden met zich mee waarin een leven naast het onderzoek niet lijkt te bestaan. Met name mijn ouders, zus Corinne, zwager Wouter, huisgenoot Armand en natuurlijk Josine hebben in zulke tijden voor de steun en afleiding gezorgd, die nodig is om het vol te houden.

*Amsterdam, mei 1999*